THE EFFECTS OF IMPOSED PRE-SWIRL ON THE STATIC AND ROTORDYNAMIC PERFORMANCE FOR SMOOTH ANNULAR LIQUID SEALS

A Thesis

by

JOSHUA THOMAS BULLOCK

Submitted to the Office of Graduate and Professional Studies of
Texas A&M University
in partial fulfillment of the requirements for the degree of

MASTER OF SCIENCE

Chair of Committee,	Dara W. Childs
Committee Members,	Luis San Andrés
	Paul Cizmas
Head of Department,	Andreas Polycarpou

May 2019

Major Subject: Mechanical Engineering

ABSTRACT

The tested annular seals were smooth with a length-to-diameter ratio of 0.50, a diameter of 102.0064 mm (4.016 inches), and a nominal radial clearance of 0.2032 mm (0.008 inches). The tests were conducted for angular shaft speeds, ω, of 2, 4, 6, and 8 krpm, axial pressure drops, ΔP, of 2.1, 4.13, 6.21, and 8.27 bar (30, 60, 90, and 120 psi), eccentricity ratios, ϵ_0, of 0.00, 0.27, 0.53, and 0.8, with three pre-swirl inserts to target zero, medium, and high (0.0, 0.4, and 0.8) pre-swirl ratios for a set of pre-determined operating conditions with ISO VG 2 oil at 46.1°C (115°F). Circumferential fluid velocity components were measured at single locations upstream and downstream from the seal's inlet and exit. Most of the data presented in this thesis takes place in the transitional regime.

The static performance of the seals was evaluated by measuring volumetric leakage rate, $\dot{Q}$, inlet and exit circumferential fluid velocity, and the rotor's eccentric position. Comparisons are made between measured values and predictions. The measured vector Reynolds number ranged from ~1180 to ~4350, with only occasional points in the laminar and turbulent regimes. Pitot tubes were used to measure the average circumferential velocity at the inlet and outlet of the seal were used to calculate pre-swirl ratio, PSR, and post-swirl ratio, OSR, respectively. The PSR tended to converge to a value of ~0.4-0.5 as ω increased for all tested pre-swirl inserts. There was little correlation between the inlet pre-swirl ratio and post-swirl ratio, OSR. This is the first known attempt to measure OSR.

Rotordynamic coefficients analyzed include direct and cross-coupled: stiffness, damping, and virtual mass. The rotordynamic coefficients were generally unaffected by changing $\epsilon_0 \in$

[0.00, 0.53]. When ϵ_0 = 0.80, the measured K_{xx} values were generally negative, while K_{yy} increased in magnitude by a factor of ~1.5 from the measured values at ϵ_0 = 0.53. The results indicated that when higher PSRs were experienced by the seal, the seal was more destabilizing. The direct damping values, C_{xx} and C_{yy}, were normally positive, and equal. When ϵ_0 = 0.80 the measured cross-coupled damping, C_{xy} and C_{yx}, decreased by a factor of 5, causing both to become negative; changing the damping from gyroscopic to dissipative.

The whirl frequency ratio, WFR, indicated that the cross-coupled virtual mass terms were too small in magnitude to affect overall rotordynamic stability. WFR was generally within ~0.3-0.6 and was unaffected by changing either ϵ_0 or ΔP except at ω = 2 krpm. When ω = 2 krpm for the zero pre-swirl insert, WFR increased in magnitude by a factor of ~4 when ϵ_0 increased from 0.00 to 0.80. The effective damping results showed that of the tested seals, the most stable seal configuration was ω = 2 krpm for the zero pre-swirl insert particularly at high ΔP's. Both the WFR and effective damping showed that as ω increases, the effect of the pre-swirl insert diminishes. For the zero pre-swirl insert, the seals were generally less stable than predicted with a few exceptions.

DEDICATION

I dedicate this work to my amazing wife, Denise, without whom this thesis would not have been possible. You’ve driven me to become a better version of myself, to be unafraid of the unknown, and to have a lot more gray hair. I can’t begin to thank you for all of your love, support, and patience, and as we enter into parenthood, know that I am so excited for all of our adventures yet to come.

ACKNOWLEDGEMENTS

Dr. Dara Childs: Thank you for the opportunity to pursue a M.S. degree at Texas A&M University through the Turbomachinery Laboratory. Through your endless patience, you taught me that there is no substitute for honesty, intelligence, and modesty. I am thankful to know you and hope that one day, you'll refer to me as a 'nice, smart guy'.

Alex J. Moreland and Jose M. Torres: thank you for your unrelenting support through endless obstacles, support, and advice. I couldn't have done it without you.

Jesus Salas, Ivan Cortez, Clay Norrbin, Jimmy McLean, and Andrew Crandall: my experience would not have been the same without you. Thank you for making my time at Texas A&M unforgettable. Dr. Luis San Andrés and Dr. Paul Cizmas: Thank you for taking the time to be on my committee.

To my Family: Your love and support provided the motivation needed to complete this thesis. It's been a long journey and you've been there for me every step of the way.

CONTRIBUTORS AND FUNDING SOURCES

Contributors

This work was supervised by a thesis committee consisting of Professor Dara Childs and Professor Luis San Andrés of the Department of Mechanical Engineering and Professor Paul Cizmas of the Department of Aerospace Engineering.

All work for the thesis was completed independently by the student.

Funding Sources

This work was made possible in part by Shell Oil. Its contents are solely the responsibility of the author.

NOMENCLATURE

C_{ij}	Damping Coefficient	[FT/L]
C_r	Radial Clearance	[L]
C_r/R	Clearance to Radius Ratio	[-]
D	Rotor Diameter	[L]
D_i	Inner Diameter of Seal	[L]
D_o	Outer Diameter of Seal	[L]
e_0	Static Eccentricity	[L]
F_s	Applied Static Load	[F]
f_w	Whirl Frequency Ratio as defined in Eq. (24)	[-]
F_x, F_y	Excitation Forces in *x* and *y* axes	[F]
K_{ij}	Stiffness Coefficient	[F/L]
L	Axial Seal Length	[L]
M_{ij}	Virtual Mass Coefficients	[M]
$\dot{Q}$	Volumetric Flow Rate	[L^3/T]
R	Rotor Radius	[L]

Greek Symbols

$\epsilon_0 = e_0/C_r$	Static Eccentricity Ratio	[-]
ΔP	Axial Pressure Drop	[F/L^2]
μ	Fluid Dynamic Viscosity	[FT/L^2]
ρ	Fluid Density	[M/L^3]
$\upsilon_{inlet}, \upsilon_{outlet}$	Measured Inlet and Outlet Circumferential Fluid Velocity	[L/T]
ω	Angular Shaft Speed	[1/T]

Subscripts

i	Direction of System Response (x or y axes)
j	Direction of System Perturbation (x or y axes)

Abbreviations

OSR	Post-swirl Ratio as defined in Eq. (4)	[-]
PSR	Pre-swirl Ratio as defined in Eq. (3)	[-]

TABLE OF CONTENTS

Page

LIST OF FIGURES

Page

LIST OF TABLES

1. INTRODUCTION

Annular seals are mechanical devices in rotating machinery that restrict leakage flow from areas of differing pressures. To do this, seals inhibit flow from high pressure areas to low pressure areas, similar to the function of a restrictive orifice. Common applications for annular seals in centrifugal pumps are case wear rings, interstage seals, and balance-pistons as illustrated in Fig. 1. Annular seals can be a primary contributor to the overall pump vibration characteristics due to the large reaction forces they produce.

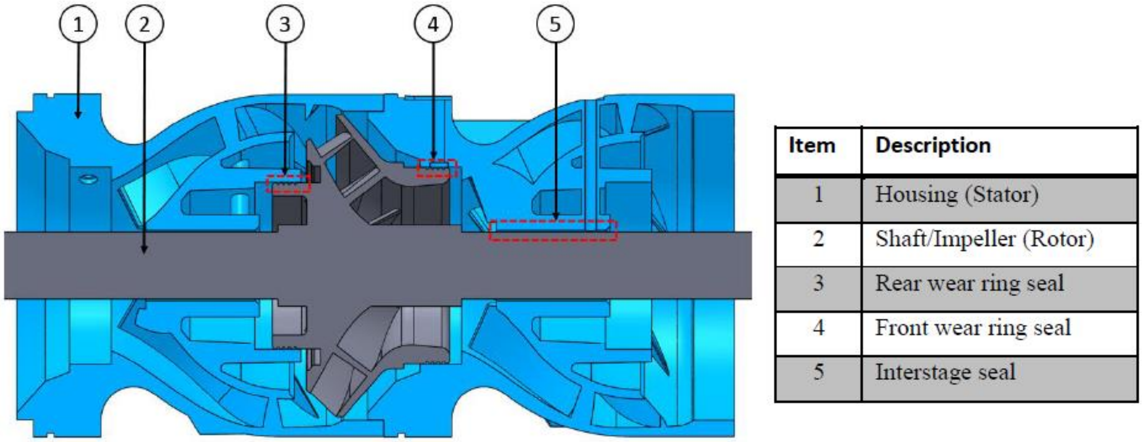

Item	Description
1	Housing (Stator)
2	Shaft/Impeller (Rotor)
3	Rear wear ring seal
4	Front wear ring seal
5	Interstage seal

Figure 1. Pump cross-section of representative seal locations in an electrical submersible pump. Adapted from Childs [1].

One of the driving factors of seal rotordynamic performance is the axial development of the circumferential fluid velocity of the lubricant as it approaches the annular seal. This inlet circumferential velocity depends on the upstream flow conditions and rotor speed, ω. The inlet swirl velocity affects the overall rotordynamic performance of a pump across common operating parameters by reducing the dynamic instability characteristics of the annular seals. While studies have previously shown that oil inlet swirl velocities in the direction of shaft rotation are a source of instability, few annular seal test rigs are designed to impose and measure pre- and post-swirl.

For most applications, annular seals experience fully-developed turbulent flow due to the typical ΔP, clearances, and the fluid being pumped. The typical clearance-to-radius ratio in an annular seal is 0.002-0.004. In some process flows, the abrasive particulates can cause the clearance between the seal surfaces to enlarge. Enlarged clearances between these surfaces markedly increase leakage rates and reduces the seal's centering forces.

As first discussed by Black [2], seals have a significant effect on the rotordynamic performance of a pump. To analyze the rotordynamic performance of an annular seal, the position of the rotor and the rotordynamic coefficients need to be identified. The position of the rotor or the static eccentricity ratio is defined as,

$$\epsilon_0 = e_0/C_r \, , \tag{1}$$

where e_0 is the static eccentricity, and C_r is the radial clearance between the rotor and the seal. The model for eccentrically operating seals developed by Nelson and Nguyen [3, 4] is,

$$\begin{aligned} -\begin{Bmatrix} f_{sx} \\ f_{sy} \end{Bmatrix} = \begin{bmatrix} K_{xx}(\epsilon_0) & K_{xy}(\epsilon_0) \\ K_{yx}(\epsilon_0) & K_{yy}(\epsilon_0) \end{bmatrix} \begin{Bmatrix} \Delta x \\ \Delta y \end{Bmatrix} + \begin{bmatrix} C_{xx}(\epsilon_0) & C_{xy}(\epsilon_0) \\ C_{yx}(\epsilon_0) & C_{yy}(\epsilon_0) \end{bmatrix} \begin{Bmatrix} \Delta \dot{x} \\ \Delta \dot{y} \end{Bmatrix} \\ + \begin{bmatrix} M_{xx}(\epsilon_0) & M_{xy}(\epsilon_0) \\ M_{yx}(\epsilon_0) & M_{yy}(\epsilon_0) \end{bmatrix} \begin{Bmatrix} \Delta \ddot{x} \\ \Delta \ddot{y} \end{Bmatrix}, \end{aligned} \tag{2}$$

where f_{sx} and f_{sy} are the seal reaction force components, and K_{ij}, C_{ij}, and M_{ij} are the stiffness, damping, and virtual mass matrix entries, respectively. Direct coefficients can be identified by the *xx* or *yy* subscripts, while the cross-coupled coefficients can be identified by the *xy* or *yx* subscripts. The terms Δx, Δy, $\Delta \dot{x}$, $\Delta \dot{y}$, $\Delta \ddot{x}$, and $\Delta \ddot{y}$ are components of the relative displacement, velocity, and acceleration vectors between the rotor and the stator, respectively.

Liquid annular seals generate a centering force in the following two ways [2]: (1) hydrodynamic pressure distributions due to the shaft rotation, and (2) the Lomakin effect. As shown in Fig. 2, the hydrodynamic pressure develops for an eccentrically positioned rotor when shearing forces from the rotation of the rotor drag the lubricant into converging and diverging wedges; labeled in Fig. 2 as “+” and “-“, respectively. In a bearing, flow in the converging region develops a local increase in pressure. In the diverging wedge of a bearing, cavitation eliminates the negative pressures, and provides the restoring forces [5]. In an annular seal, the elevated local pressure suppresses cavitation, and the seal must be displaced eccentrically to develop a hydrodynamic centering force.

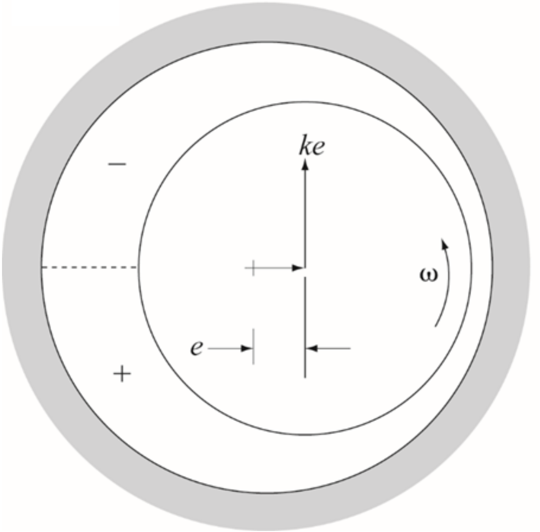

Figure 2. Pressure distribution for a displaced rotor in a fluid-filled annulus for counter-clockwise rotation. Adapted from Childs [6].

Unlike hydrodynamic bearings, annular seals see significant axial ΔPs and flow rates, $\dot{Q}$. These two factors give rise to the phenomenon known as the Lomakin Effect [7]. The relatively large ΔP causes the fluid to accelerate when it enters the seal causing an abrupt reduction in pressure near the inlet. As the lubricant flows through the seal, the fluid friction at the seal walls cause the axial pressure to drop further. When the rotor is eccentrically positioned, as shown by the dotted rotor in Fig. 3, there is a smaller radial clearance at the top and a larger clearance on the bottom of the rotor. This reduction in clearance at the top causes a drop in the axial Reynolds number and an increase in wall friction which generates the restoring force, F_r shown in Fig. 3; whereas the reverse is true for the enlarged clearance at the bottom.

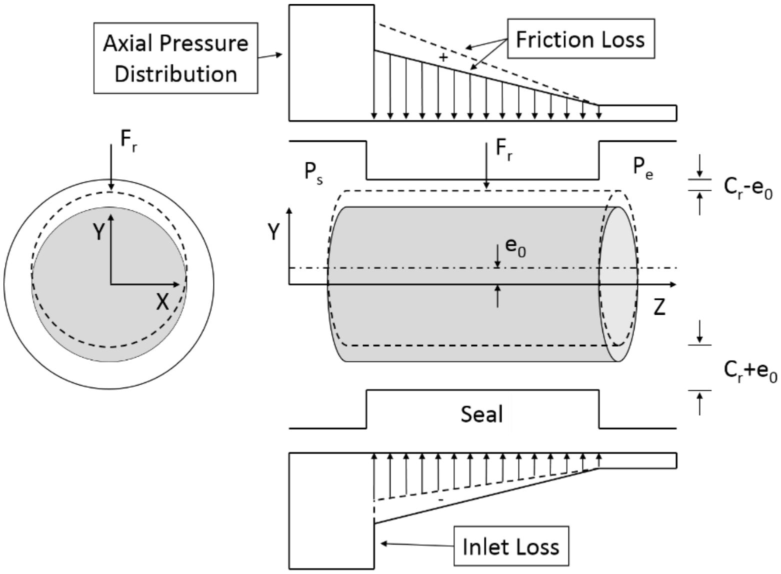

Figure 3. Depiction of Lomakin Effect centering forces. Adapted from Moreland [8].

Similar to a journal bearing, a less stable seal is likely to have large K_{xy} and K_{yx} coefficient values with opposing signs [9]. The destabilizing K_{xy} and K_{yx} coefficients increase with increasing average circumferential fluid velocity, v_{inlet}. Thus, if v_{inlet} can be decreased, then the destabilizing forces can also be reduced.

The pre-swirl ratio is defined [10] as,

$$PSR = \frac{v_{inlet}}{\omega R} \tag{3}$$

Iwatsubo et al. [11] used a seal rig with water to vary and measure pre-swirl velocities using a pitot tube. Their tests did not cover the same range of ω and ϵ_0 as detailed here.

The post-swirl ratio is similarly defined as,

$$OSR = \frac{v_{out}}{\omega R} \tag{4}$$

where v_{out} is the average circumferential fluid velocity downstream of the seal outlet. The only published measurements of the post-swirl in liquid annular seals are those taken using the current test rig by Moreland [8] and Torres [12].

1.1 Theoretical Literature

Numerous authors have published work on the static and dynamic rotordynamic characteristics of turbulent-flow liquid annular seals. In 1970 Jenssen [13] used a “short-seal” approach to develop theoretical predictions of the reactive forces for the experimental tests he conducted on smooth, annular seals. In 1983 Childs [14] performed a dynamic analysis based on Hirs lubrication equation and developed finite length solutions for rotordynamic coefficients of turbulent annular seals for small motion about a centered orbit. In 1988 Nelson and Nguyen [3,4] used a turbulent bulk-flow model for plain annular seals for non-centered seals and compared their simulated results to the measured results of Jenssen [13] and Falco et al [15]. Nelson and Nguyen calculated the rotordynamic coefficients of Eq. (2) for turbulent-flow seals for: for $0.1 \leq \epsilon_0 \leq 0.7$, ω < 7 krpm, and ΔP < 17.2 bar (250 psi). In 1996 Zirkelback and San Andrés [16] developed a bulk-flow model for the transition to a turbulent flow-regime for annular pressure seals. Despite all of the turbulent flow data, there has not been a substantial body of data published in the transitional regime to verify the model.

1.2 Experimental Literature

In 1984 Kanki et al. [17] tested smooth, annular water-lubricated seals. Kanki’s tests were conducted for $0 \leq \epsilon_0 \leq 0.9$, ω < 2 krpm, and ΔP < 14.7 bar (203 psi). In 1986 Falco et al [15] tested short, water-lubricated seals for $0 \leq \epsilon_0 \leq 0.7$ for ω = 4 krpm and ΔP = 10 bar. Jenssen

[13] tested the load-carrying capacities for smooth, annular, water-lubricated seals. Using a test rig similar to the one used for this investigation, in 1997 Marquette et al. [18] tested smooth, water-lubricated annular seals for $\epsilon_0 \leq 0.5$, ω = 10.2 - 24.6 krpm, and $\Delta P < 41.4$ bar (600 psi). Marquette et al. studied the effects of ϵ_0 on the rotordynamic coefficients of seals. Marquette recognized that a major drawback of the study was the lack of control and measurement of the inlet pre-swirl. In 2015 Salas [19] measured both static and dynamic characteristic behaviors for laminar-flow, smooth annular seals for $0 \leq \epsilon_0 \leq 0.8$.

Despite the large volume of research performed, at the time of writing, this author believes that the only published experimental studies that examine the rotordynamic effects of imposed pre-swirl in an oil-lubricated annular seal for the testing conditions discussed in the scope of work are those by Moreland [8] in 2016 and Torres [12] in 2016. And at the time of writing, there has been no published data to validate the accuracy of the XLAnSeal [16] model predictions in the transitional regime.

2. STATEMENT OF WORK

Based on current published literature, there is a large gap of knowledge on the effects of pre-swirl on rotordynamic coefficients over a full range of eccentricity ratios, ϵ_0 and the effect of the transitional regime on the prediction of rotordynamic coefficients. This thesis seeks to establish a measured data base for analysis of the static and rotordynamic parameters of seals when a range of pre-swirls are imposed.

Most of the available literature on the impact of PSR on seal rotordynamic performance employ water as the test fluid for ϵ_0 less than 0.5. Furthermore, other studies that discuss the rotordynamic of smooth seals in relation to PSR did not test a large range of running speeds, ω, and ϵ_0. The only studies available presenting measured outlet swirl ratio, OSR, are those by Moreland [8] and Torres [12] for a smooth seal-grooved rotor and grooved seal-smooth rotor, respectively, taken from the present test rig. All of the test data available for plain annular seals is either comfortably turbulent, or laminar. The author is unaware of any published test data that provides a substantial body of data in the transitional regime.

The plain annular seals tested were based on the characteristic dimensions of a typical electrical submersible pump, ESP: L = 50.8 mm (2.00 inches), D_i = 102 mm (4.016 inches), and C_r = 0.203 mm (0.008 inches). Target test conditions as outlined in Table 1 were imposed for each level of pre-swirl (zero, medium, and high) using ISO VG 2 oil at 46.1°C (115°F). The target test conditions were selected based on common operating conditions found in ESPs. Measured static data from these tests include: volumetric leakage rate ($\dot{Q}$), inlet and exit circumferential fluid velocity, and rotor position. The rotordynamic coefficients identified from these tests include direct and cross-coupled: stiffness, damping, and virtual mass. The test conditions discussed in the scope of work were selected based on the most common operating conditions of electrical submersible pumps. The test rig is a modified version of the test rig design by Kaul [20] based on the “floating stator” concept developed by Glienicke [21].

Table 1. Test matrix for each of the three PSR inserts

ω [krpm]	ΔP [bar]	ϵ_0 [-]	ω [krpm]	ΔP [bar]	ϵ_0 [-]	ω [krpm]	ΔP [bar]	ϵ_0 [-]	ω [krpm]	ΔP [bar]	ϵ_0 [-]
2	2.07	0.00	4	2.07	0.00	6	2.07	0.00	8	2.07	0.00
		0.27			0.27			0.27			0.27
		0.53			0.53			0.53			0.53
		0.80			0.80			0.80			0.80
	4.14	0.00		4.14	0.00		4.14	0.00		4.14	0.00
		0.27			0.27			0.27			0.27
		0.53			0.53			0.53			0.53
		0.80			0.80			0.80			0.80
	6.21	0.00		6.21	0.00		6.21	0.00		6.21	0.00
		0.27			0.27			0.27			0.27
		0.53			0.53			0.53			0.53
		0.80			0.80			0.80			0.80
	8.27	0.00		8.27	0.00		8.27	0.00		8.27	0.00
		0.27			0.27			0.27			0.27
		0.53			0.53			0.53			0.53
		0.80			0.80			0.80			0.80

The results from these imposed conditions will be compared to predictions from XLAnseal of the XLTRC^2 software suite based on Zirkelback and San Andrés model [16] and will seek to show the effects of the imposed testing conditions on the rotordynamic coefficients for smooth annular seals.

3. TEST APPARATUS

The most recent tests performed using the test rig involved various types of journal and tilt-pad bearings. Hence, the rig had to be modified to test annular seals. A cutaway of the test rig can be seen in Fig. 4. The test rig consists of the following major components: driver, rotor, stator, loading system, instrumentation, oil system. Each of the following sections will detail the major changes that the test rig experienced after the setup used by Salas [17] and before the setup used by Moreland and Torres [8, 12]. As shown in Fig. 4, there are two pedestals bases supporting the rotor that are rigidly mounted to a large bed plate. The bearings are contained between a lower and upper pedestal mount. The upper pedestal has hydraulic shakers rigidly mounted that attach to the stator. The ceramic ball bearings have oil mist lubrication.

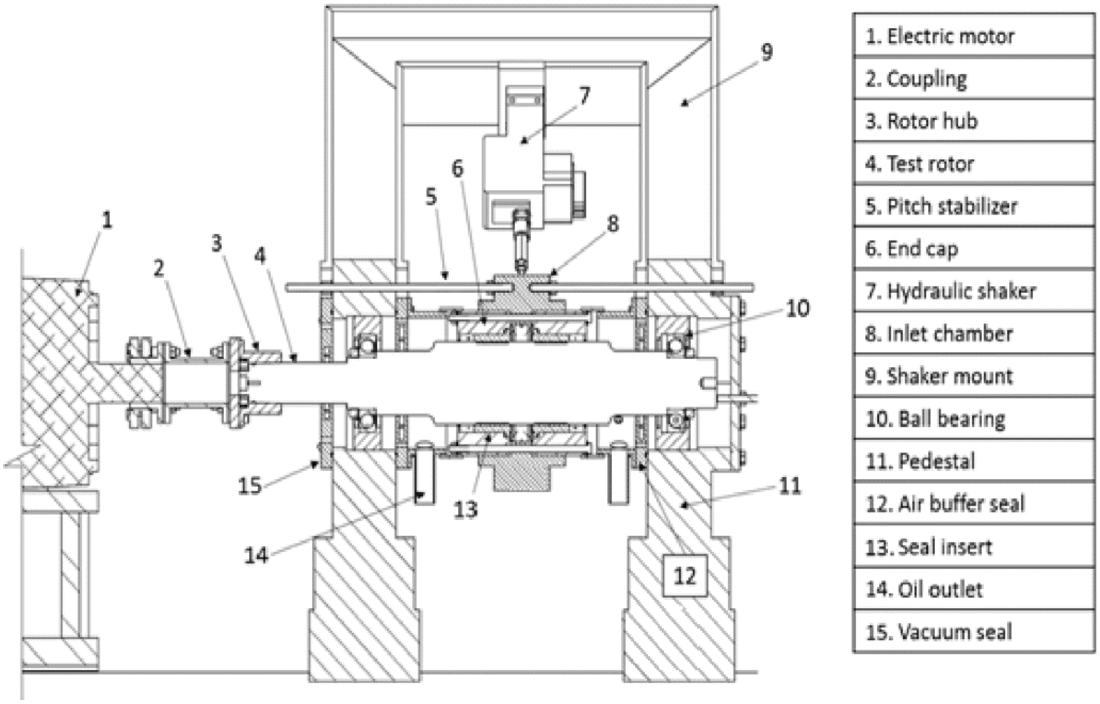

Figure 4. Test Rig Components. Adapted from Moreland [8].

Figure 5 provides a side view of the test rig showing how the static loader attaches to the stator. A-A shows the yoke attachment to the stator and B-B is the plane the where the oil inlet ports are located. A connection exists from the static loader to the stator through a yoke and heavy gauge steel cabling which allows it to apply force in the negative *Y*-direction.

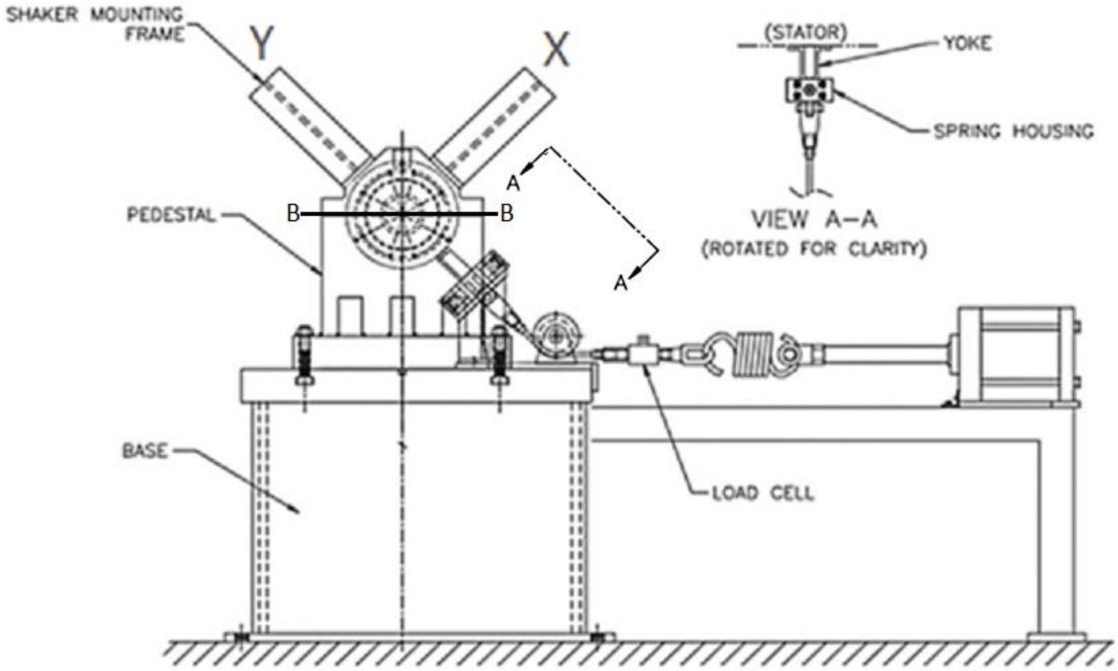

Figure 5. Non-drive end view of test rig showing the static loader. Adapted from and modified from Kulhanek [22].

Except for the flow meter, the instrumentation used in this experiment is cited in Fig. 6. The flowmeter used is described in further detail in Section 3.5.

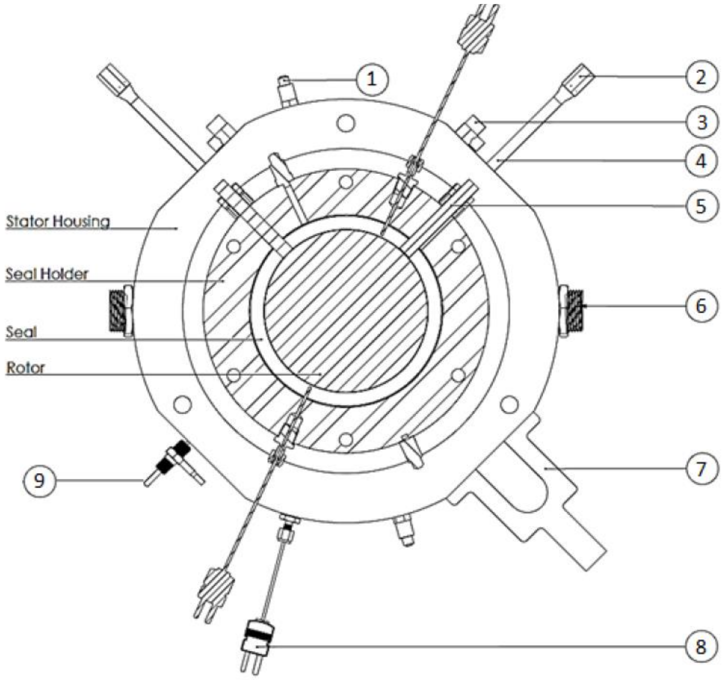

Item	Description
1	Pressure Transducer
2	Load Cell
3	Accelerometer
4	Dynamic Shaker
5	Proximity Probe
6	Oil Inlet
7	Static Loader
8	Thermocouple
9	Pitot Tube

Figure 6. Cross-section of the stator with the attached instrumentation. Adapted and modified from Torres [12].

3.1 Driver

The driver for the test rig was originally a 33 kW (45 hp) air turbine, but due to inadequate speed control, the driver was replaced with an electric motor with a variable-frequency driver. The electric motor is a 133 Hz (8 krpm), 30 kW (40 hp) Baldor design, complemented by a Schneider Electric Altivar M-Flex 71 variable frequency drive. The motor allows for a control accuracy of ±0.025 Hz (±0.0015 krpm) compared to an accuracy of ±0.83 Hz (0.050 krpm) with the air turbine. The coupling was replaced by a custom (R+W LP300) coupling. An adaptor was developed to accomodate greater misalignment and the ability to disconnect and reconnect the coupling quickly. The coupling uses a keyed, slip-fit on the motor side and a hydraulic press fit on the rotor side.

3.2 Rotor

The rotor is made of 4140 Stainless Steel and has a test section diameter of 101.6 ±0.005 mm (4.000 ± 0.0002 in) and is supported by a pair of ceramic angular ball bearings contained within two bearing cartridges mounted at both ends. The surface finish was ~0.41 µm (16 µin). The test rotor is shown in Fig. 7.

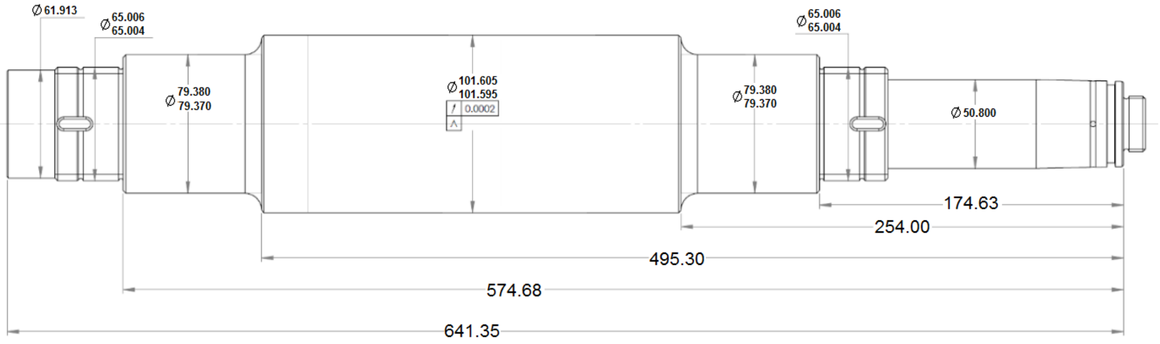

Figure 7. Smooth test rotor. All dimensions are in millimeters. Adapted and modified from Moreland [8].

3.3 Stator Assembly

As shown in Fig. 8, the stator assembly is composed of two opposing test seals, a pre-swirl insert, a central test housing, and two seal-holder end caps. The stator is assembled on a precision ground mandrel to ensure that both the drive end and non-drive end seals are concentric. The nominal mandrel-to-seal clearance is 25.4 µm (0.001 inches). The assembly is held together using bolts that are carefully torqued in a star pattern during assembly.

During testing, the oil enters the stator from two ports located along the horizontal plane 180° apart. The oil then enters the test section of the stator, passes through the pre-swirl insert, and then enters the seal. When it exits the seal, the oil collects in the seal holder cavity where it is then drained back to the reservoir at atmospheric pressure. The seal-holder end caps also contain a labyrinth tooth at the oil exit to maintain a back pressure and prevent air intrusion.

The stator assembly is the key to the entire test section; it contains instrumentation, aligns the seals, allows oil to enter the test section, and holds the pre-swirl insert. The stator and end caps have bolt holes and unique cutaways that minimize misalignment or mis-installation of the seals. The pitch stabilizers shown in Fig. 4 are threaded into the stator and connect it to the pedestals. When tensioned down properly, the pitch stabilizers remove the pitch and yaw from the system. This is verified by observing the alignment-agreement of the two sets of Lion proximity probes, which measure displacement in both the *X*- and *Y*- planes on the drive and non-drive ends of the test section. These proximity probes measure the relative dynamic movement of the stator and have a repeatability of ±0.009%.

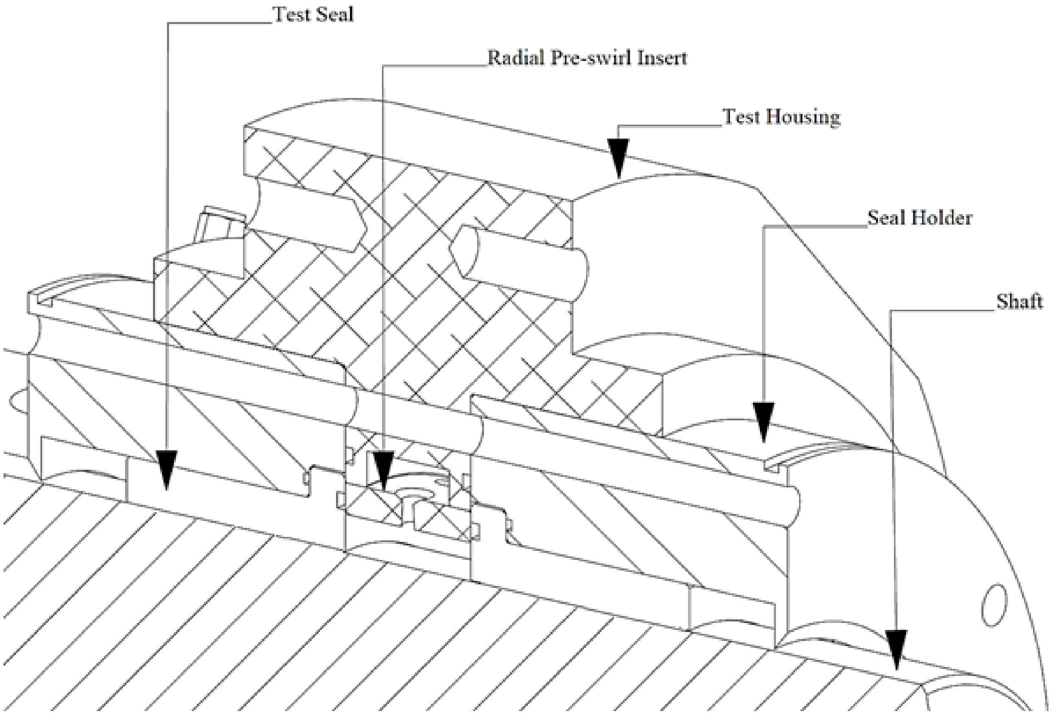

Figure 8. Cross-section of the test rig showing the zero pre-swirl insert. Adapted and modified from Torres [12]

3.3.1 Test Seals

The test seals were made from 660 Bronze with a nominal diameter of 101.6 mm (4 inches) with a nominal-radial clearance of 203.2 µm (0.008 inches) and a length of 50.8 mm (2 inches). They were designed with a line-to-line fit with the end caps so that when they are press-fitted into the end caps there is no plastic deformation of the components. The face-to-face length of the seal is 50.8 mm (2.0 in), which gave a length to diameter ratio, L/D, of 0.5. A 3-D representation of the seal is shown in Fig. 9.

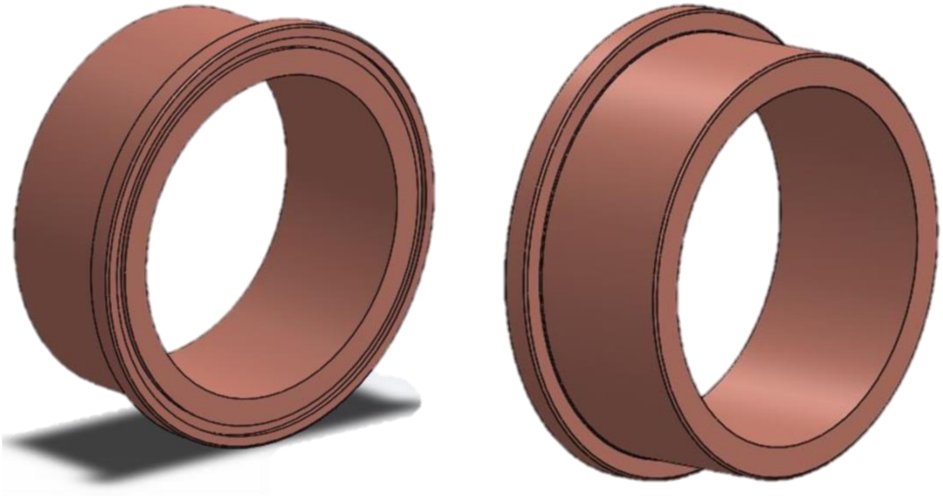

Figure 9. Front and back views of the annular seal used in the experiment. Adapted from an internal memo.

3.3.2 Pre-swirl Inserts

The stator has two radial injection ports that are located along the horizontal plane 180° apart along the B-B line in Fig. 5. The fluid exits the inlet ports and flows through the pre-swirl insert and enters the seal inlet cavity. The inlet and outlet oil pressures are measured by three Kulite XTM-190 transducers; the transducers have an upper range of 17.2 bar (250 psi) with a repeatability of ±1%. The pressure transducer on the stator measures the inlet pressure just behind the pre-swirl insert, while the outlet pressure is measured on both the drive and non-drive side end caps. The oil temperature is measured upstream and downstream of the seal by Omega thermocouples that have an upper range of 200°C (392°F) with a repeatability of ±2.2°C (±3.96°F).

Three different pre-swirl inserts were manufactured out of 7075-T6 Aluminum. The inserts were designed to achieve 0.0, 0.4, and 0.8 (zero, medium, and high) PSR at 3.6 krpm for the specified operating conditions in Table 2 by changing the number, angle and diameter of the oil injection nozzles.

Table 2. Specified conditions for the pre-swirl insert design.

Parameter	Metric Units	English Units
ΔP	2.41 – 3.1 bar	35-45 psig
C_r	0.381 mm	0.015 in.
ω	3.6 krpm	
Lubricant	ISO VG 2	

Figure 10 shows the cross-sections for the zero, medium, and high pre-swirl inserts. The nozzle diameters were varied from 4.978 mm (0.1960 in) for the zero and medium pre-swirl insert to 4.039 mm (0.1590) for the high pre-swirl conditions. The angle of attack, α, of the nozzles of the medium and high pre-swirl inserts is 55.7°. The fluid velocity leaving the pre-swirl insert can be defined as,

$$v_{insert} = \frac{\dot{Q}}{12\pi r_{nozzles}^2} \tag{5}$$

where $r_{nozzles}$ is the radius of each nozzle in the pre-swirl insert.

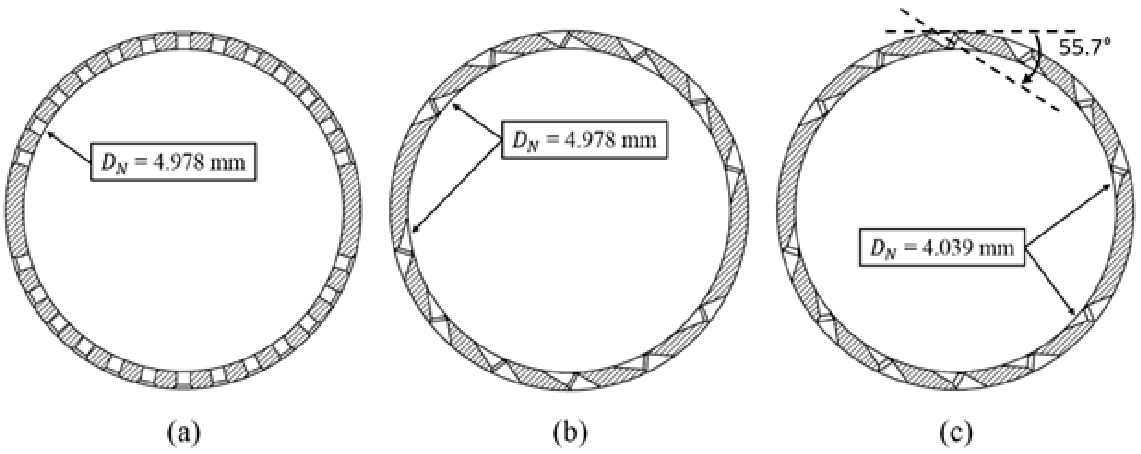

Figure 10. Pre-swirl inserts. (a) Zero pre-swirl. (b) Medium pre-swirl. (c) High pre-swirl. Adapted and modified from Moreland [8].

Figure 11 shows the cross-section of the stator assembly and the placement of the pitot tubes in relation to the pre-swirl injection ports. As shown in Fig. 11, the pre-swirl pitot tube is installed in the stator assembly at a point where the flow will be as developed as nearly as possible just before the fluid enters the drive-end seal. The pitot tube is located orthogonal to the direction of the static load. The OSR pitot tube is installed on the drive side end cap as close as possible to the fluid exit of the seal. The static and dynamic pressures from the pitot tube are measured using a Rosemont differential pressure transmitter with an accuracy of ±0.14% of span.

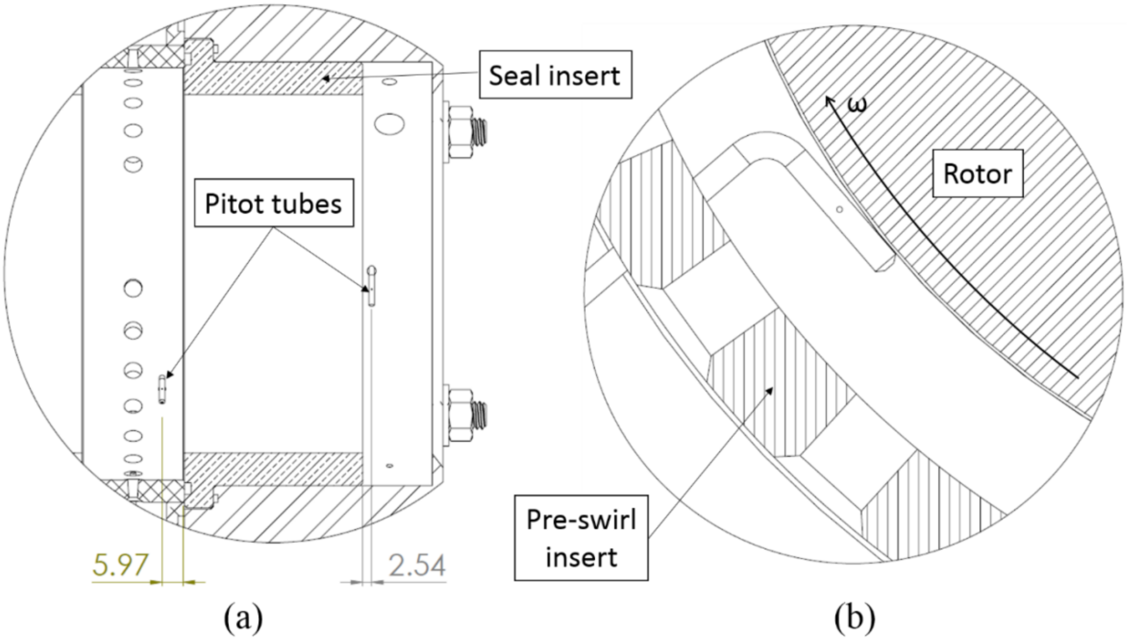

Figure 11. Cross-section of the stator showing (a) axial and (b) radial position of the pitot tubes. All dimensions are in millimeters. Adapted from Moreland [8].

Figure 12 shows the overall shape and dimensions of the pitot tube.

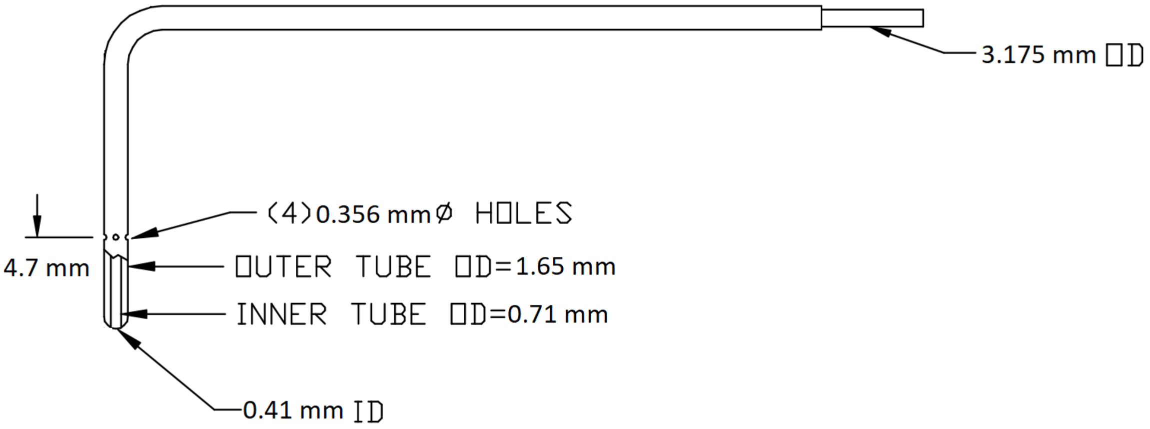

Figure 12. Pitot tube dimensions.

Figure 13 shows the installed radial position of the pre- and post-swirl pitot tubes. Both the pre- and post-swirl pitot tube radial distance from the rotor is equal to C_r or 0.2032 mm.

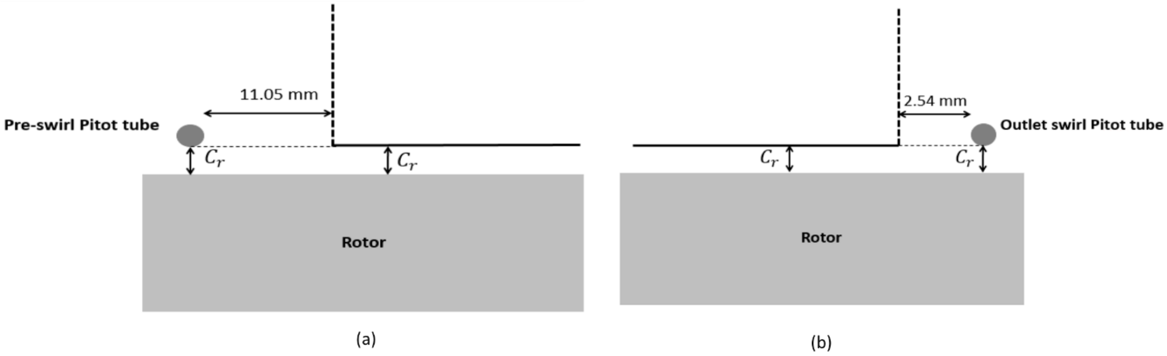

Figure 13. Radial position of the (a) pre-swirl and (b) post-swirl pitot tube. Note: figure is not drawn to scale. Adapted from Najeeb. [23]

3.4 Static and Dynamic Loading

Figure 14 shows a simplified view of stator-stinger connection locations and the relative position of the applied static load from the non-drive end. The shakers are driven by two hydraulic pumping units manufactured by Zonic. Each stinger is attached to an exciter head and a dual loop master controller in the *x*-*y* planes. A load cell is connected to the stator so that each Zonic can control the load being transmitted to the stator assembly. The Zonic shakers can provide both static and dynamic loads. The hydraulic shakers can apply dynamic loads at frequencies up to 1 kHz. To measure the acceleration of the stator at high frequencies, a pair of PCB accelerometers with repeatability of ±5.0% of the measured value were connected via NPT fittings on the stator itself providing a solid connection between the measuring device and the test section. The *y*-axis shaker can provide up to 4500 N (1000 lbf) of tensile and 9000 N (2000 lbf) of compressive static forces. The *x*-axis shaker can provide up to 4500 N (1000 lbf) in compressive and tensile static forces. When using the Zonic shakers to provide static loads, the amount of static load had to be restricted such that the hydraulic pressure had enough capacity to provide adequate dynamic loading capability. When the static load exceeded the capabilities of the Zonic shakers, a pneumatic piston, or static loader, connected via an extension spring was used to apply the necessary force, F_s, to move the stator into the desired eccentric position.

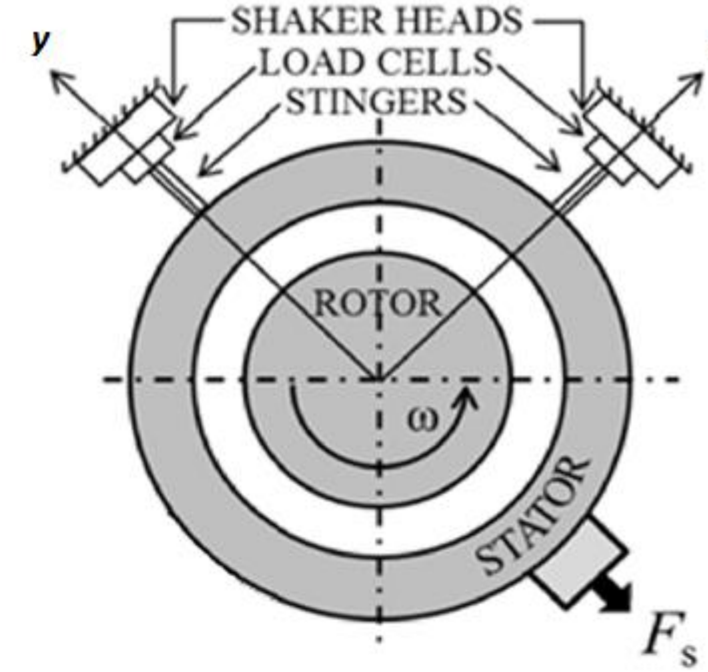

Figure 14. Drive end view of the stator-stinger connection locations. Adapted and modified from Kluitenberg [24].

3.5 Oil System

Based on preliminary simulations, the flow required for the test seals was much higher than the previous test rig could deliver, Salas [17]. To accommodate the required flow requirements with a low viscosity fluid, a pair of Viking spur gear pumps were installed to provide flow capabilities up to ~265 liters per minute (70 gpm). The oil reservoir for the oil system consists of two tanks, a 950 liter (250 gallon) main tank and a 380 liter (100 gallon) return tank. The pumps are connected via a series of pneumatic control valves controlled with a PID temperature controller that allows the lubricant to be pumped to the test section at a relatively constant 46°C (115°F) ±1.11°C (±2°F). The temperature of the system is measured at both the inlet and outlets of the test section, and the oil flow rate to the test rig is measured by an FTI turbine flow meter ~4.6 meters (15 ft.) upstream from the test section with a range of 0-265 liters per minute (0-70 gpm) and a repeatability of ±0.05% of the reading. A schematic of the oil system is shown in Fig. 15.

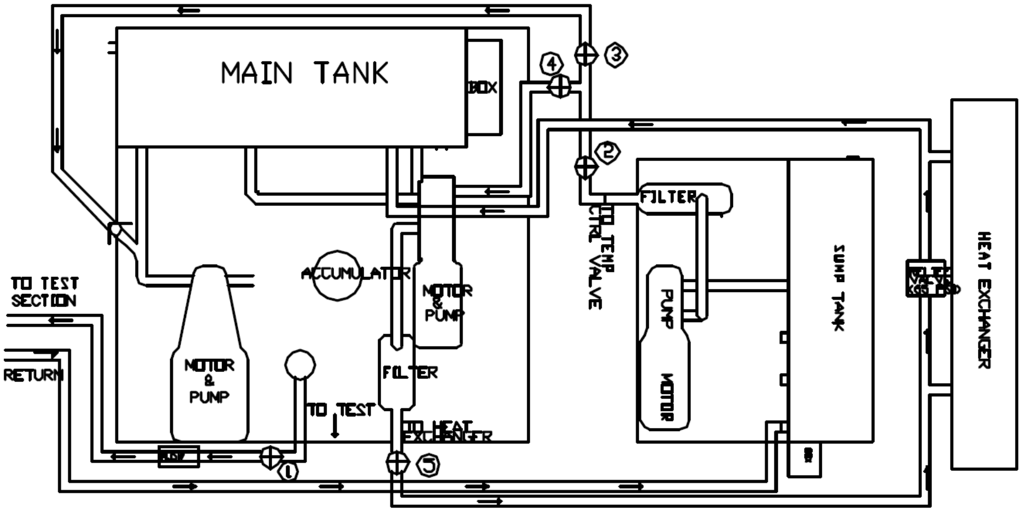

Figure 15. Schematic of oil supply and control system. Adapted from Kaul [20].

The viscosity and density of the system oil were separately measured to ensure accurate Reynolds number calculations. These measurements were taken using a Brookfield Viscometer with a repeatability of ±0.2% of the measured value. The viscosity and density data gathered are shown in Fig. 16.

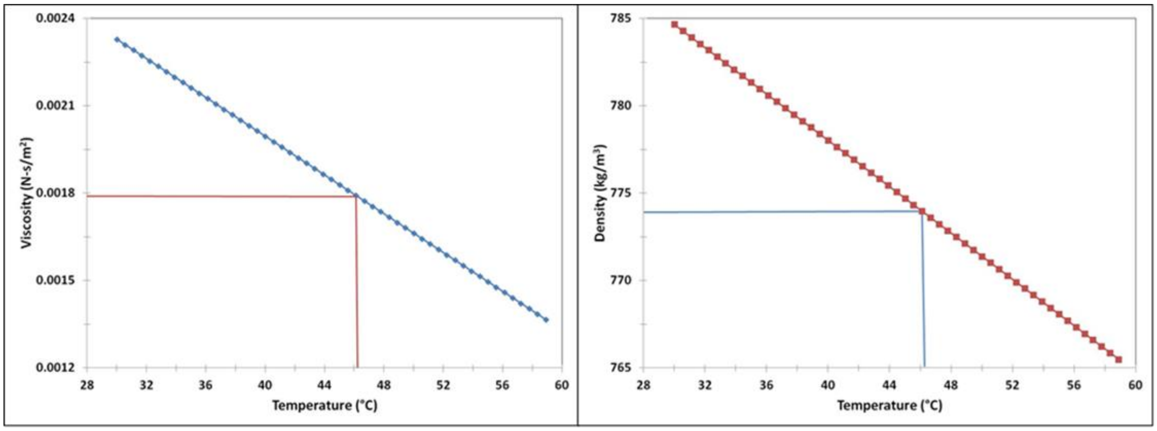

(a) (b)

Figure 16. ISO VG 2 oil (a) viscosity and (b) density vs. temperature.

4. STATIC RESULTS

4.1 Cold-Clearance Measurement

After the test section is assembled and prior to the introduction of any liquid, a “cold” clearance is taken. The cold clearance measurement is performed by using the hydraulic shakers to first push the stator into the stationary rotor and then precess the stator around the rotor. The measurements from separate sets of proximity probes at both ends of the stator are averaged to obtain the diametral clearance of the seals at room temperature.

4.2 Hot-Clearance

ISO VG-2 is used to bring the system up to steady-state conditions using the heater and oil pumps. When the system reaches 46.1°C (115°F), the pumps are shut off, and the clearance measurement is immediately repeated; this "hot" clearance is used for predictions. The hot clearance taken on each testing day is a key indicator that the rig is ready for testing and that the instrumentation is properly set. The radial clearance averaged 185.3μm (0.00729 in.) over the three days required for testing. Representative clearance figures from each configuration are shown in Fig. 17. The discrepancy between the nominal radial seal clearance 203.2 μm (0.008 in.) and the average measured value is due to machining tolerances and the thermal expansion that the seals experienced during testing.

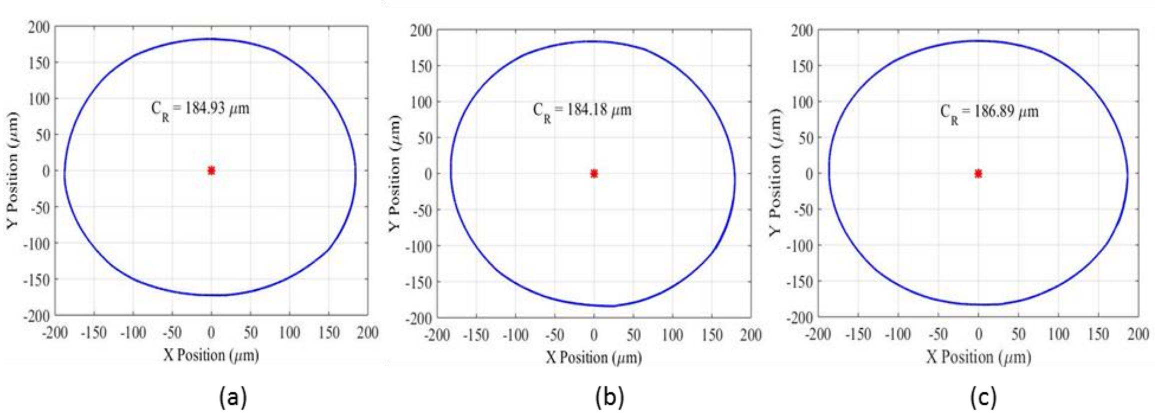

Figure 17. Representative hot-clearance for the (a) zero (b) medium, and (c) high pre-swirl insert.

4.3 Leakage

Figure 18 shows a representative relationship of the test data and the predictions between $\dot{Q}$ and ΔP for each of the tested ϵ_0 values using the zero pre-swirl insert. As can be seen, $\dot{Q}$ is largely unaffected by increasing ϵ_0, but is strongly affected by differential pressure. As ΔP increases, $\dot{Q}$ increases by a factor of almost 4. The measured results and the XLAnseal predictions are also shown. For the zero pre-swirl insert and low ω, there is good agreement between the measured results and XLAnseal. (Note: The full $\dot{Q}$ data set are provided in Appendix A: Tabulated Results)

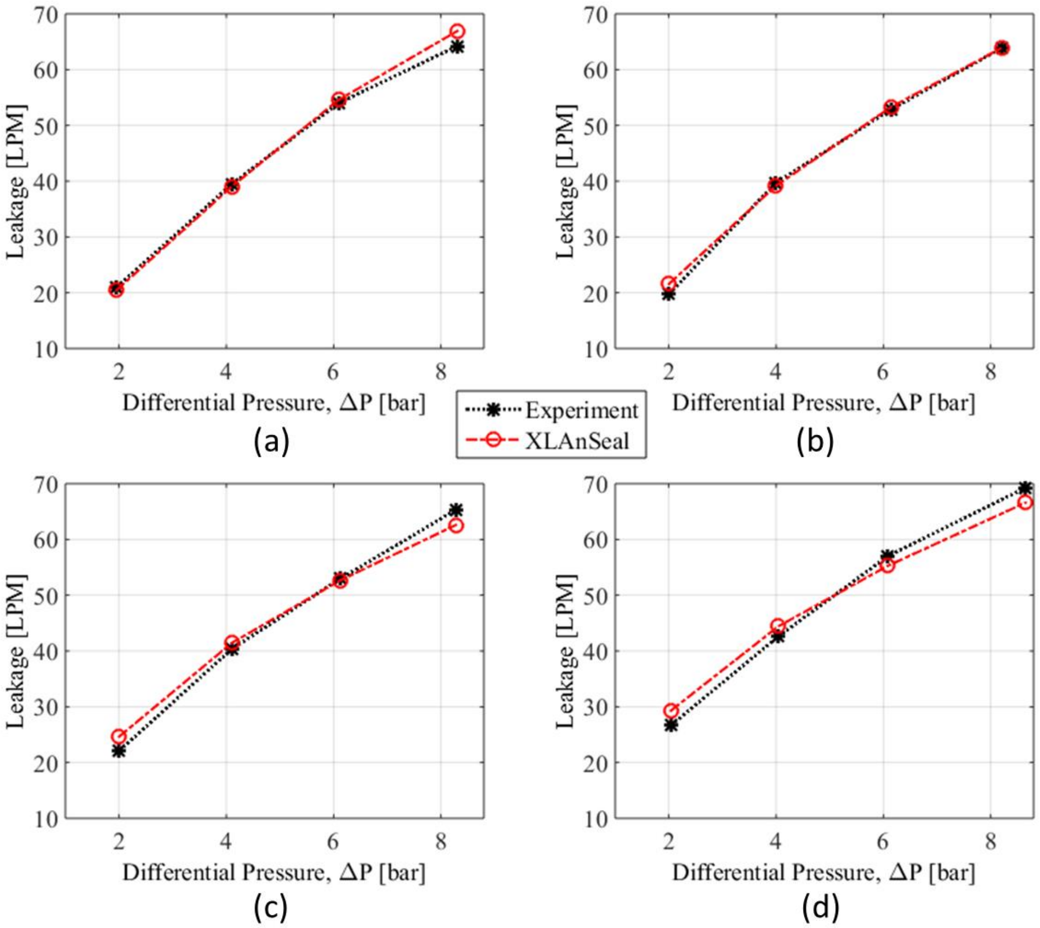

Figure 18. $\dot{Q}$ **vs.** ΔP **at ω = 2 krpm for the zero pre-swirl insert for** ϵ_0 **= (a)** 0.00**, (b)** 0.27 **(c)** 0.53**, and (d)** 0.80**.**

Figure 19 shows a representative relationship between $\dot{Q}$ and ΔP at $\omega = 6$ krpm. Comparing Fig. 18 and Fig. 19, show that as ω increases, $\dot{Q}$ decreases, and the predicted leakage rates from XLAnseal start to diverge from measured values. These relationships hold true for all of the pre-swirl inserts.

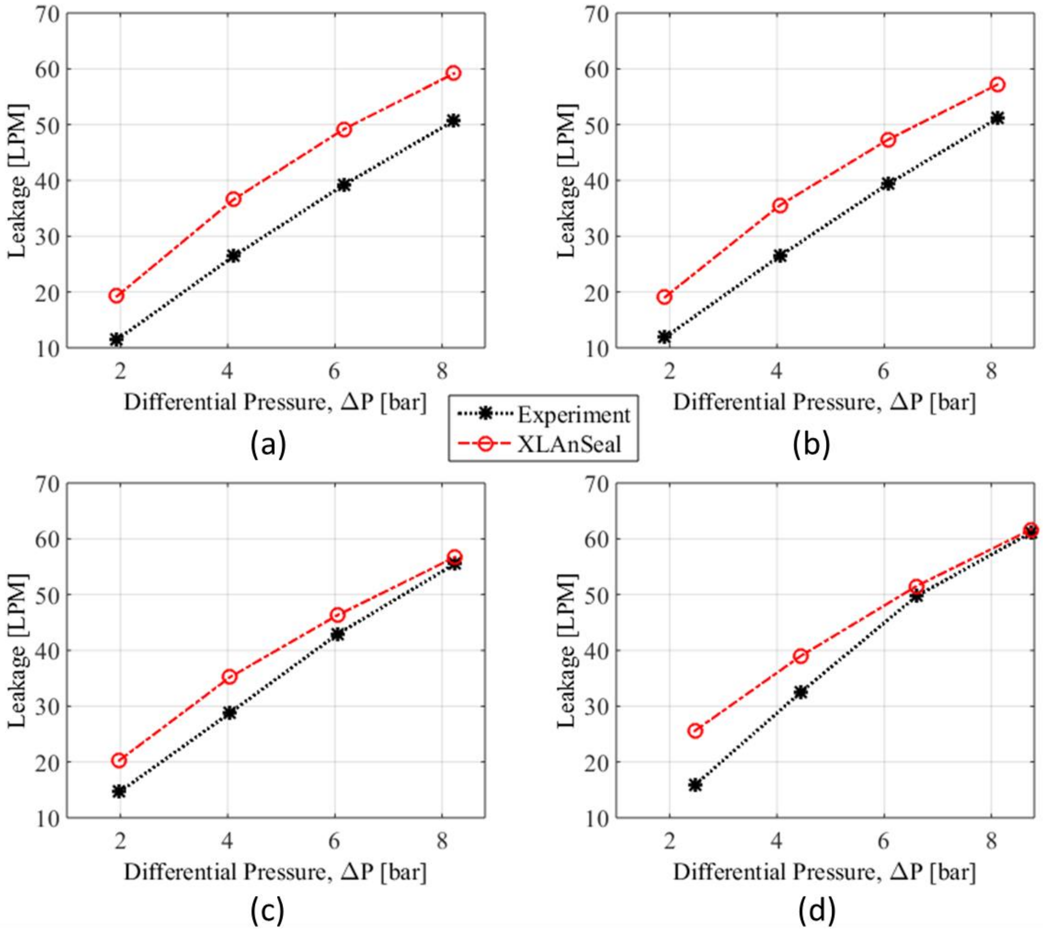

Figure 19. $\dot{Q}$ vs. ΔP at ω = 6 krpm for the zero pre-swirl insert for ϵ_0 = (a) 0.00, (b) 0.27 (c) 0.53, and (d) 0.80.

Figure 20 shows a representative relationship between $\dot{Q}$ and ω for ϵ_0 = 0.53. As ω increases, $\dot{Q}$ gradually decreases. When ΔP increases from 2.1 bar to 8.27 bar, $\dot{Q}$ increases approximately 300%. At high ω and low ΔP, the XLAnseal predictions diverge from the measured experimental values. For ω = 2krpm, the predictions over-predict the experimental results by ~10 LPM. As ω and ΔP increases, the predictions and the experimental results converge.

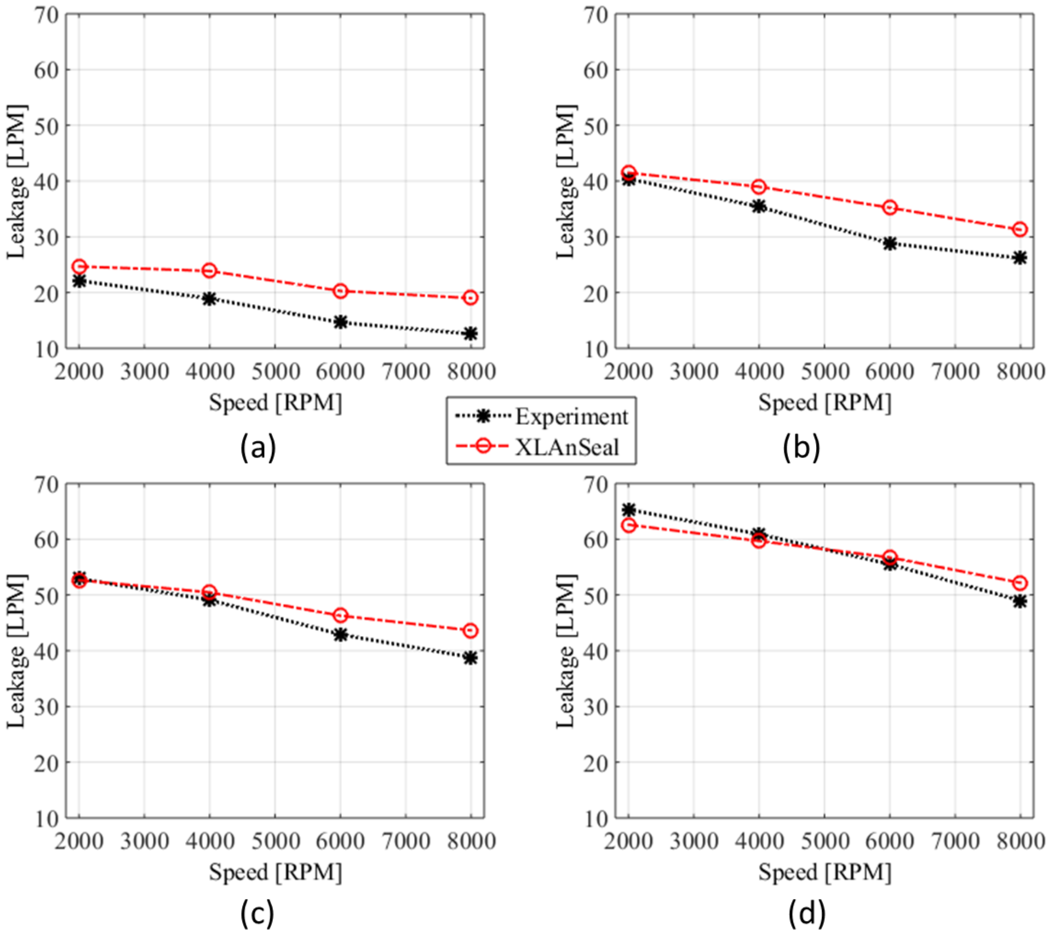

Figure 20. $\dot{Q}$ **vs. ω for the zero pre-swirl insert at** ϵ_0 **= 0.53 for Δ*P* = (a) 2.1, (b) 4.13, (c) 6.21, and (d) 8.27 bar.**

Overall, measured $\dot{Q}$ ranged from 9.73 LPM (2.57 gpm) with the medium pre-swirl insert at ω = 8 krpm, ΔP = 2.07 bar, and ϵ_0 = 0.00 to 69.27 LPM (18.3 gpm) with the zero pre-swirl insert at ω = 2 krpm, ΔP = 8.27 bar, and ϵ_0 = 0.80. $\dot{Q}$ was generally unaffected by increasing pre-swirl.

4.4 Reynolds Number

The Reynolds number used for flow-regime calculations is the Euclidean norm of the axial and circumferential Reynolds numbers. Axial Reynolds number is defined as,

$$Re_z = \frac{\dot{Q} C_r \rho}{A\mu}, \tag{6}$$

where A is the annular clearance area defined as,

$$A = 2\pi R C_r + \pi C_r^2 \tag{7}$$

Circumferential Reynolds number is defined as,

$$Re_\theta = \frac{R\omega C_r \rho}{2\mu}, \tag{8}$$

Following Zirkelback and San Andrés [16], C_r is used as the hydraulic radius. The total Reynolds number is therefore defined as,

$$Re = \sqrt{Re_z^2 + Re_\theta^2}, \tag{9}$$

Following San Andrés [16], flow regimes will be defined as shown in Table 2,

Table 3. Flow-regime categorizations

Flow-Regime	Reynolds Number
Laminar	Re < 1000
Transitional	1000 $\leq$ Re $\leq$ 3000
Turbulent	3000 < Re

Figure 21a shows that Re_z generally decreases as ω increases. There is a strong, positive correlation between Re_z and ΔP; as ΔP increases, Re_z also increases. Figure 21b shows the linear relationship between ω and Re_θ; it also shows that there is no relative relationship between ΔP and Re_θ. These relationships are evident in Fig. 21c; as ω and ΔP increase, Re also increases. At higher ω, Re tends to converge regardless of the imposed ΔP. In general, the choice of imposed pre-swirl insert did not affect Re. The range of Reynolds numbers covers the transitional and turbulent regimes.

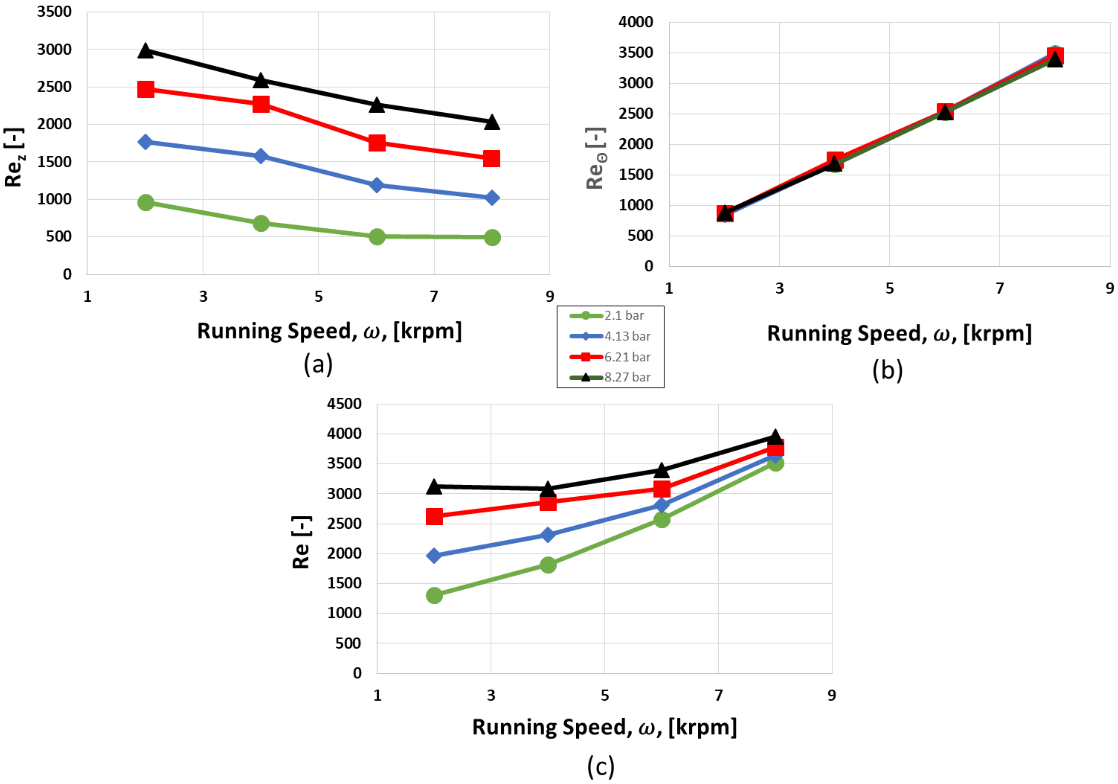

(a)

(b)

(c)

Figure 21. (a) Re_z, (b) Re_θ, and (c) Re vs. ω for the zero pre-swirl insert at ϵ_0 = 0.00.

Figure 22 shows the relatively small effect that changing ϵ_0 has on Re relative to the effects of ω. For every 2 krpm increase in ω, there is an increase of approximately 500 in Re.

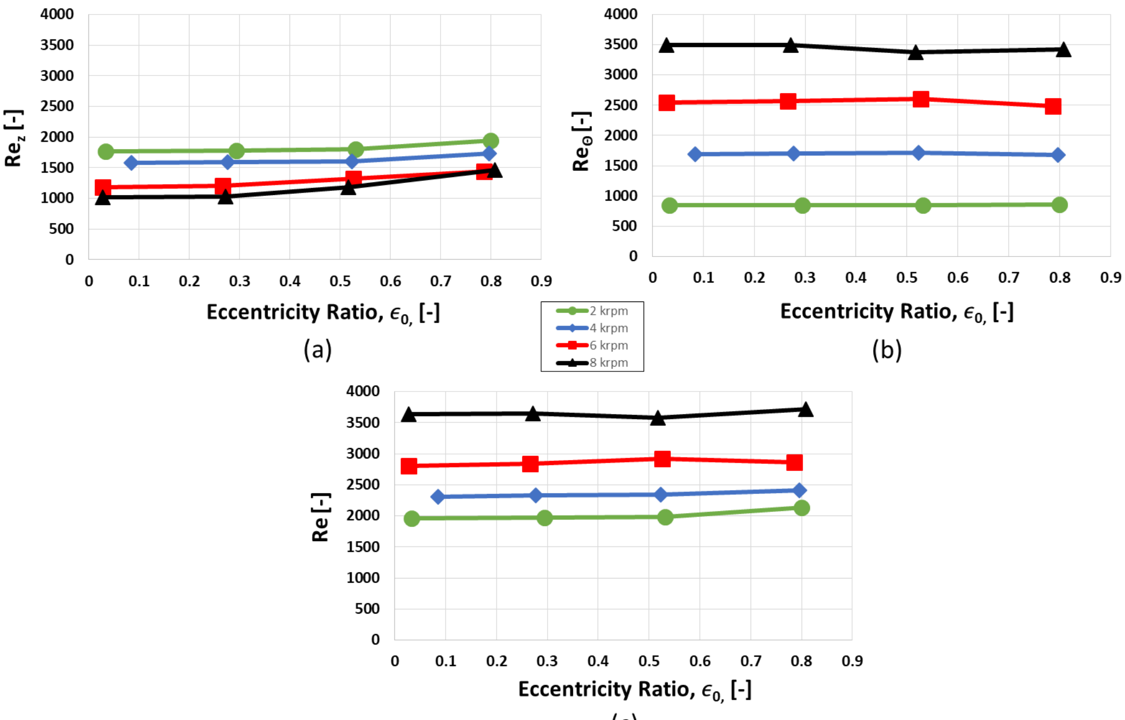

(a)

(b)

(c)

Figure 22. (a)Re_z, (b) Re_θ, and (c) Re vs. ϵ_0 for the zero pre-swirl insert at ΔP = 4.13 bar.

XLAnseal predicted that the flow would range the transitional, and turbulent regimes as defined in Table 3. Tests showed that the flow was mostly transitional, with occasional test points in the laminar and transitional regimes. Measured Re ranged between 437 and 4340. A plot representative of the Re experienced by the seals is given below in Fig. 23. At low ϵ_0 for all ω, XLAnSeal struggles to accurately predict the expected Reynolds numbers. As ϵ_0 increases, the predictions from XLAnseal match the measured results more closely.

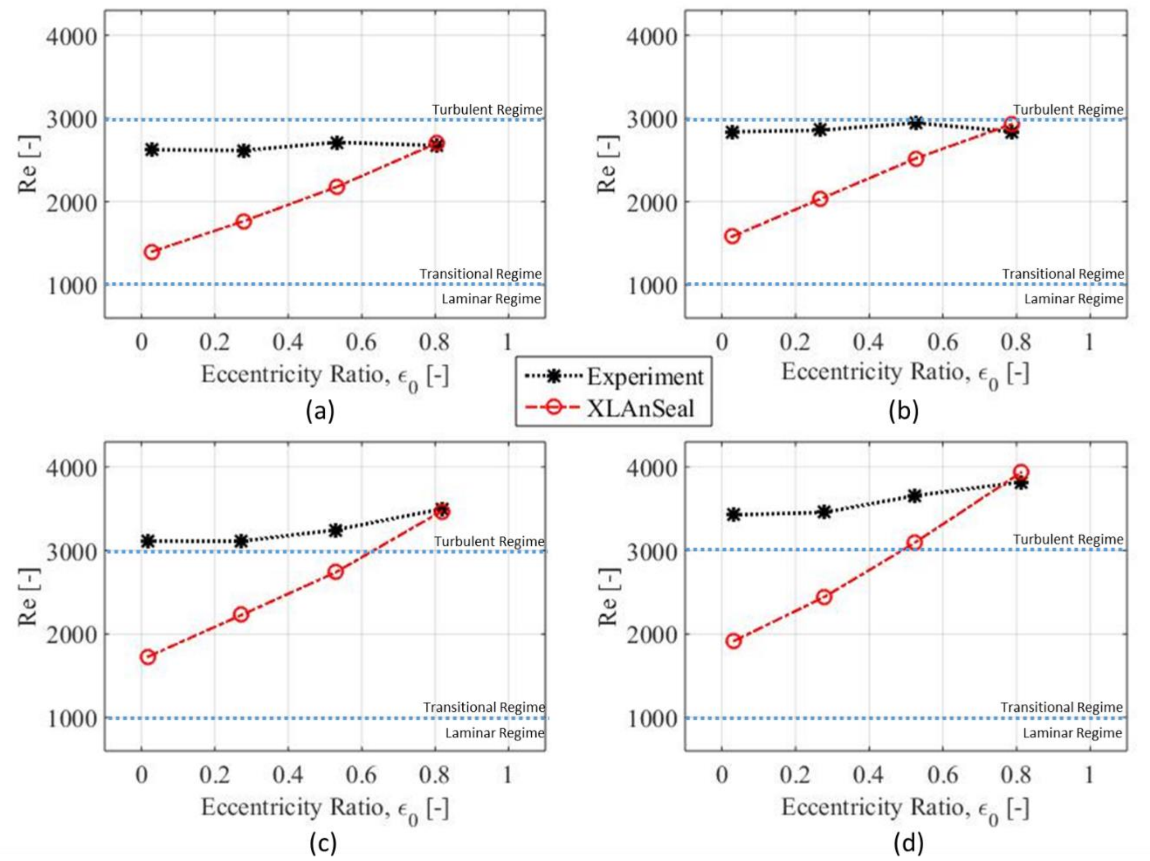

Figure 23. Re vs. ϵ_0 at ω = 6 krpm for the zero pre-swirl insert for ΔP = (a) 2.1, (b) 4.13, (c) 6.21, and (d) 8.27 bar.

4.5 Pre-swirl Ratio

Measured circumferential fluid velocity is used to calculate PSR and OSR and is defined as,

$$v_{inlet\ or\ outlet} = \sqrt{\frac{2\Delta P_v}{\rho}}, \tag{10}$$

where ΔP_v is the differential pressure experienced by the pitot tube, and ρ is the fluid density at the operating temperature. The predictions shown in Section 6 use the measured values of pre-swirl ratio.

Figure 24a shows that for the zero pre-swirl insert, v_{inlet} increases as ω increases and ΔP decreases; i.e., due to the decrease in inlet flow rate, the fluid is able to obtain more injection circumferential fluid velocity. Figure 24b and Fig. 24c shows that v_{inlet} is relatively unaffected by increasing ω, but generally increases for increasing ΔP. As expected, the medium and high pre-swirl inserts significantly increase v_{inlet} at low speeds. At higher speeds, v_{inlet} is relatively unaffected by moving to higher pre-swirl inserts.

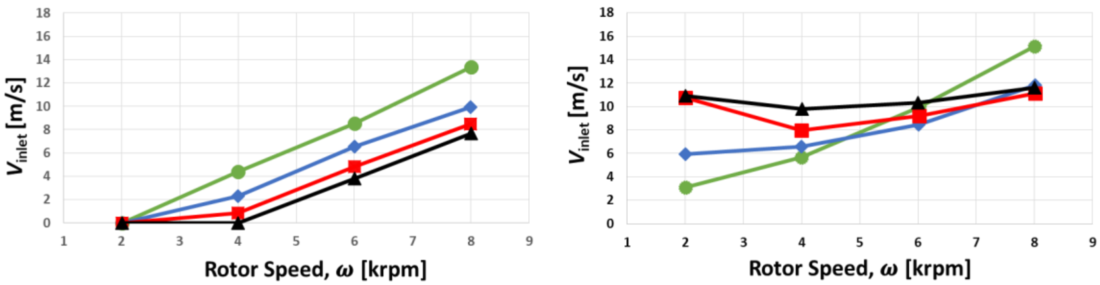

(a) zero

(b) medium

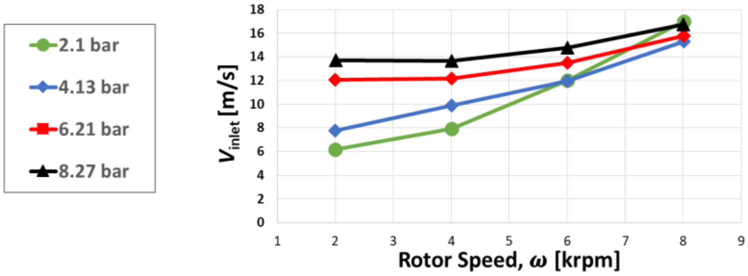

(c) high

Figure 24. v_{inlet} **vs.ω at** ϵ_0 **=0.53 for the (a) zero, (b) medium, and (c) high pre-swirl insert.**

Recall the definition of pre-swirl ratio from Eq. (3). Figure 25 shows a representative correlation of the PSR data collected. Clearly PSR is a strong function of ω and ΔP. Figure 25a shows for the zero pre-swirl insert, as ΔP increases, PSR decreases due to increased $\dot{Q}$. For the high pre-swirl insert in Fig. 25b, as ΔP increases, PSR increases due to the enhanced circumferential flow from the insert. As ω increases, the PSRs tend to converge to ∼0.4.

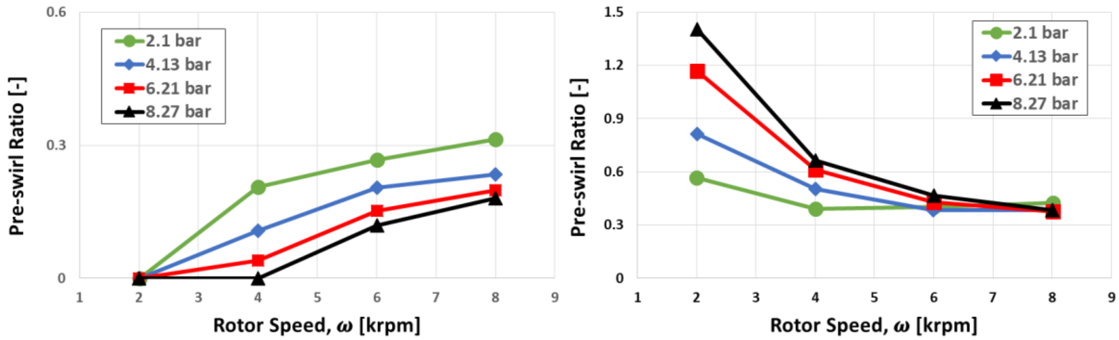

(a) zero (b) high

Figure 25. PSR vs. ω at ϵ_0 = 0.53 for the (a) zero and (b) high pre-swirl insert.

Table 3 shows the maximum and minimum PSRs achieved for each ω. As expected from Eq. (3), the maximum PSR decreases as ω increases, appearing to converge to ~0.4.

Table 4. Minimum and maximum PSR values for each ω.

Running Speed [krpm]	Minimum Pre-swirl Ratio [-]	Maximum Pre-swirl Ratio [-]
2	0	1.41
4	0	0.66
6	0.12	0.47
8	0.16	0.43

Note that the circumferential velocity is measured at one location only and may not be entirely representative of the average inlet circumferential velocity to the seals.

4.6 Post-swirl Ratio

Recall the definition of post-swirl ratio given in Eq. (4). For a smooth, long seal the OSR is expected to be ~0.5 when the fluid exits the seal irrespective of the pre-swirl ratio. However, as was shown in Fig. 11, the exit circumferential velocity measurement is made downstream from the seal exit at a single point and is not necessarily a measure of the average exit circumferential velocity. The OSR ranged between 0.10 and 0.45. Figure 26a shows OSR increasing with a increasing ϵ_0 when ω = 2 krpm. There is a relatively weak, positive correlation between OSR and ϵ_0 at low ω. At ω above 2 krpm, there is no clear correlation between ϵ_0 and OSR. Figure 26a shows that as ΔP increases, OSR only slightly increases. Figure 26b shows that for high ΔP, OSR is relatively unaffected by increasing ϵ_0.

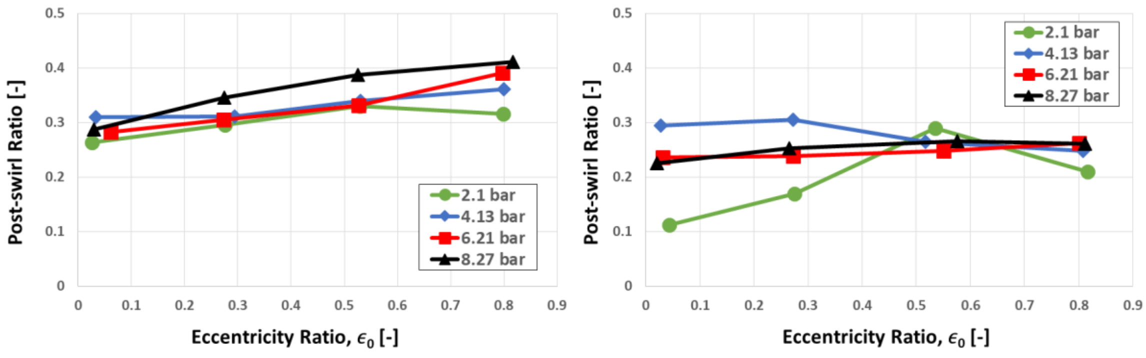

(a) ω = 2 krpm (b) ω = 8 krpm

Figure 26. OSR vs. ϵ_0 for ω = (a) 2 krpm and (b) 8 krpm.

Figure 27 shows a representative relationship of OSR vs. ω for $\epsilon_0 = 0.00$. As running speed increases, OSR tends to generally decrease, particularly for ΔP = 2.07 bar. There is no clear or consistent relationship between OSR and ΔP. The pressure at the seal outlet was relatively constant across all inlet pressure drops. The trends for the medium and high pre-swirl insert were similar to those for the zero pre-swirl insert. At low ΔP, the OSR unexpectedly dropped when ω = 6 krpm and ω = 8 krpm. The author believes this to be due in part to the placement of the post-swirl pitot tube.

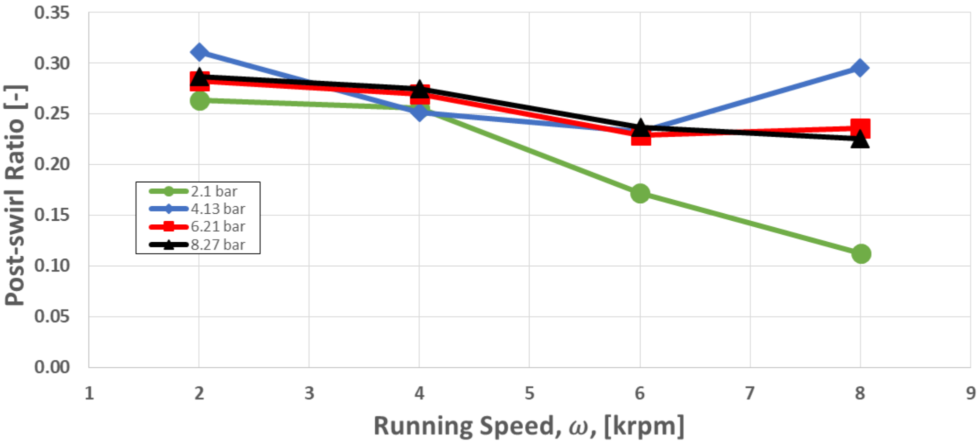

Figure 27. OSR vs. ω for the zero pre-swirl insert at ϵ_0 = 0.00.

4.7 Static Load Displacement

The static eccentricity, e_0, is the distance between the center of the seal and the center of the shaft. Figure 28 shows the coordinate system used for this test program and the relative position of the shaft center, O_j, located at $(\epsilon_{0x}, \epsilon_{0y})$ to the relative position of the seal center, O_s located at (O_{Sx}, O_{Sy}). The eccentricity ratio is defined as,

$$\epsilon_0 = \sqrt{{\epsilon_{0x}}^2 + {\epsilon_{0y}}^2} \tag{11}$$

where

$$\epsilon_{0x} = \frac{e_{0x} - O_{Sx}}{C_r},\ \epsilon_{0y} = \frac{e_{0Y} - O_{Sy}}{C_r} \tag{12}$$

The attitude angle ϕ, is defined as the angle between e_0 and the static load vector,

$$\phi = \tan^{-1}\left(\frac{\epsilon_{0x}}{\epsilon_{0y}}\right) \tag{13}$$

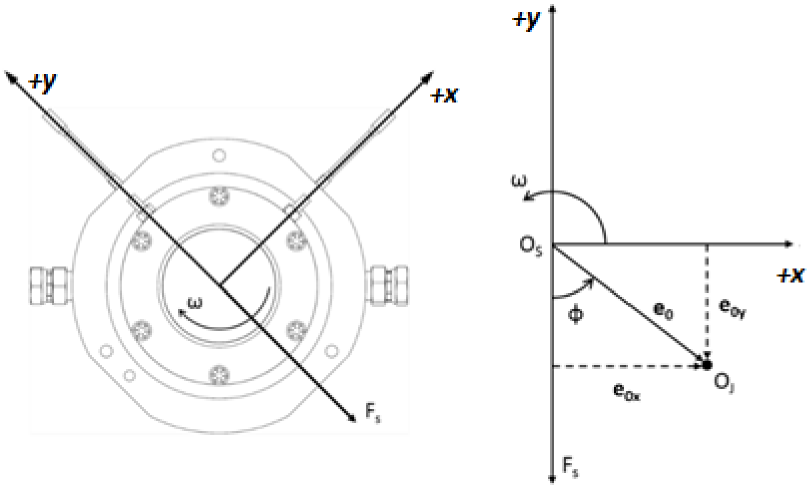

(a) (b)

Figure 28. (a) NDE view of rig coordinate system. (b) Presented coordinate system. Adapted and modified from Moreland [8].

Note that ϵ_0 = 0.00 represents a perfectly centered seal, and ϵ_0 = 1.00 represents contact between the rotor and seal.

4.8 Eccentricity Loci

Figure 29 shows the load-eccentricity-vector loci for the tested seals with the zero pre-swirl injection at 2, 4, and 8 krpm. Recall that F_s is applied in the –y direction. As can be readily seen, as ω increases the attitude angle begins to approach 90° meaning that the hydrodynamic effect begins to dominate the Lomakin effect. As Salas [17] noted, with a constant ω, as ΔP increases the attitude angle generally decreases. The other tests performed with imposed pre-swirl follow the same trends shown here with the same general magnitude of attitude angle. The complete data set for ϕ and ϵ_0 are available in Appendix A.

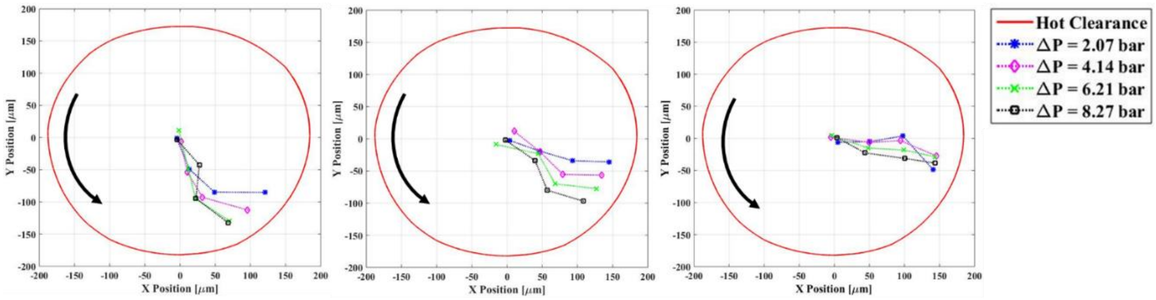

(a) (b) (c)

Figure 29. Clearance loci for the zero pre-swirl insert at ω = (a) 2 krpm (b) 4 krpm and (c) 8 krpm.

Note that for lower values of ω, the 0.00 eccentricity point is not actually in the center. During the tests due to the fact that K_{xx} and K_{yy} < 0 at $\epsilon_0 = 0.00$, the seals experience strong decentering forces, forcing the rotor to $\epsilon_0 =$ ~0.05-0.10 when “in the centered position". At higher ω, the seal decentering reaction force decreased and the seal operated closer to $\epsilon_0 = 0.00$.

5. DYNAMIC RESULTS

5.1 Dynamic Testing and Data Reduction

The method detailed by Childs and Hale [25] is used to calculate the rotordynamic coefficients. Starting with the equation of motion for the stator-system,

$$M_s \begin{Bmatrix} \Delta\ddot{x} \\ \Delta\ddot{y} \end{Bmatrix} = \begin{Bmatrix} f_x \\ f_y \end{Bmatrix} + \begin{Bmatrix} f_{sx} \\ f_{sy} \end{Bmatrix} \tag{14}$$

where M_s is the mass of the stator, f_x and f_y are the applied dynamic forces imparted by the shaker system, and f_{sx} and f_{sy} are the fluid film reaction-force components. Substituting the fluid-film reaction forces from Eq. (2) into Eq. (14) yields,

$$\begin{Bmatrix} f_x \\ f_y \end{Bmatrix} - M_s \begin{Bmatrix} \ddot{x}_s \\ \ddot{y}_s \end{Bmatrix} = \begin{bmatrix} K_{xx} & K_{xy} \\ K_{yx} & K_{yy} \end{bmatrix} \begin{Bmatrix} \Delta x \\ \Delta y \end{Bmatrix} + \begin{bmatrix} C_{xx} & C_{xy} \\ C_{yx} & C_{yy} \end{bmatrix} \begin{Bmatrix} \Delta\dot{x} \\ \Delta\dot{y} \end{Bmatrix} + \begin{bmatrix} M_{xx} & M_{xy} \\ M_{yx} & M_{yy} \end{bmatrix} \begin{Bmatrix} \Delta\ddot{x} \\ \Delta\ddot{y} \end{Bmatrix} \tag{15}$$

The dynamic data are measured in the time domain and converted into the frequency domain using a Fast Fourier Transform (FFT). The new frequency-domain sets are written as follows: displacement ($\boldsymbol{D}_x$, $\boldsymbol{D}_y$), acceleration ($\boldsymbol{A}_x$, $\boldsymbol{A}_y$), and excitation forces ($\boldsymbol{F}_x$, $\boldsymbol{F}_y$). The equation of motion from Eq. (15) can now be written as,

$$\begin{Bmatrix} \boldsymbol{F}_x - M_s\boldsymbol{A}_x \\ \boldsymbol{F}_y - M_s\boldsymbol{A}_y \end{Bmatrix} = -\begin{bmatrix} \boldsymbol{H}_{xx} & \boldsymbol{H}_{xy} \\ \boldsymbol{H}_{yx} & \boldsymbol{H}_{yy} \end{bmatrix} \begin{Bmatrix} \boldsymbol{D}_x \\ \boldsymbol{D}_y \end{Bmatrix} \tag{16}$$

The dynamic-stiffness coefficient, $\boldsymbol{H}_{ij}$, is related to the rotordynamic coefficients by,

$$\boldsymbol{H}_{ij} = \left(K_{ij} - \Omega^2 M_{ij}\right) + \boldsymbol{j}\left(\Omega C_{ij}\right), \tag{17}$$

where Ω is the excitation frequency and $\boldsymbol{j}$ is $\sqrt{-1}$. Separately shaking in two orthogonal directions, the system can be expressed as,

$$\begin{bmatrix} \boldsymbol{F}_{xx} - M_s\boldsymbol{A}_{xx} & \boldsymbol{F}_{xy} - M_s\boldsymbol{A}_{xy} \\ \boldsymbol{F}_{yx} - M_s\boldsymbol{A}_{yx} & \boldsymbol{F}_{yy} - M_s\boldsymbol{A}_{yy} \end{bmatrix} = -\begin{bmatrix} \boldsymbol{H}_{xx} & \boldsymbol{H}_{xy} \\ \boldsymbol{H}_{yx} & \boldsymbol{H}_{yy} \end{bmatrix} \begin{bmatrix} \boldsymbol{D}_{xx} & \boldsymbol{D}_{xy} \\ \boldsymbol{D}_{yx} & \boldsymbol{D}_{yy} \end{bmatrix} \tag{18}$$

There are now four equations with four unknown dynamic stiffness coefficients, $\boldsymbol{H}_{ij}$.

Taking Eq. (17) and separating the $\boldsymbol{H_{ij}}$ into real and imaginary parts gives,

$$Re(\boldsymbol{H_{ij}}) = K_{ij} - \Omega^2 M_{ij} = K_{ij} - \Lambda M_{ij} \tag{19}$$

$$Im(\boldsymbol{H_{ij}}) = \Omega C_{ij} \tag{20}$$

Using Eq. (17) to extract the rotordynamic coefficients, a least-squares regression curve fit is applied to the dynamic stiffness values. The stiffness and virtual mass coefficients are the *Y*-intercept and slope of the curve fit of the real part of $\boldsymbol{H_{ij}}$ versus $\Lambda = \Omega^2$, respectively. The damping coefficients are the slope of the curve fit for the imaginary part of $\boldsymbol{H_{ij}}$.

Following Beckwith [26], we can obtain the rotordynamic coefficients by calculating the slope and *Y*-intercept. Looking at a simplified linear representation of the above equations,

$$y(x_i) = a + bx_i, \tag{21}$$

the *Y*-intercept and slope can be calculated by,

$$a = \frac{\sum y_i \sum x_i^2 - \sum x_i \sum x_i y_i}{n \sum x_i^2 - (\sum x_i)^2}, \tag{22}$$

and

$$b = \frac{n \sum x_i y_i - \sum x_i \sum y_i}{n \sum x_i^2 - (\sum x_i)^2}, \tag{23}$$

respectively. This method is applied for frequencies up to 200 Hz (12 krpm), or 150% of the maximum tested ω of 133.33 Hz (8 krpm).

To isolate the dynamic stiffness for the seals alone (no fluid in the seals), the baseline dynamic stiffness is subtracted from the calculated dynamic stiffness. Because there are two seals, the resultant dynamic stiffness is halved to represent the reaction force of a single seal. The time domain data are averaged together, and repeatability is calculated as outlined in Appendix

B. The stator is excited at each of the test frequencies multiple times to establish the necessary dynamic baselines.

Figure 30a and Fig. 30b show (a) Re H_{II} and (b) Re H_{IJ} as functions of excitation frequency. Figure 30a, shows that direct dynamic stiffness decreases with increasing excitation frequency, but overall provide a good fit to Eq. (19). The *y*-intercept and curvature of Fig. 30a produce the direct stiffness and direct virtual mass coefficients, respectively. The *y*-intercept and curvature of Fig. 30b produce the cross-coupled stiffness and cross-coupled virtual mass coefficients, respectively. Figure 30b shows that the cross-coupled stiffness has relatively little dependence on the excitation frequency implying that $|M_{xy}| \cong |M_{yx}| \cong 0$.

These figures are representative of the relationship for the entire data set. The calculated dynamic stiffness shows good agreement with the model from Eq. (17) with the exception of a few outliers that appear at excitation frequencies above 160 Hz for a few of the data points. The maximum running speed was ω = 8 krpm (133 Hz), therefore the curve fit works well for excitation frequencies through the tested running speeds.

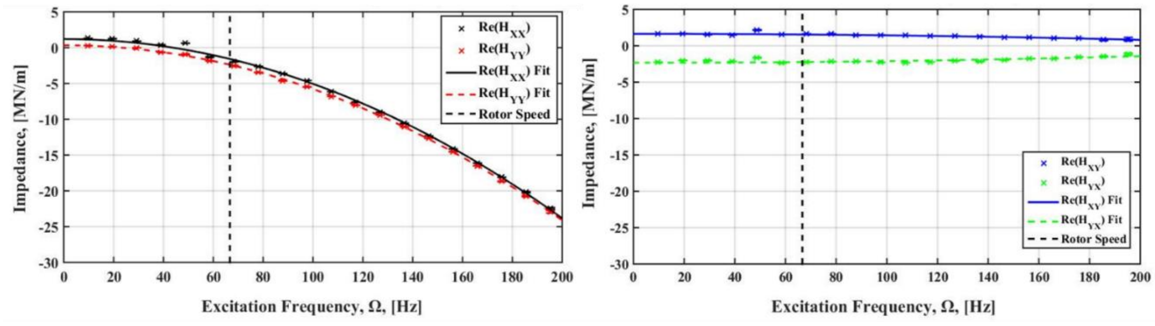

(a) (b)

Figure 30. Real component of the (a) direct and (b) cross-coupled stiffness for the zero pre-swirl insert vs. excitation frequency, Ω, for ω = 4 krpm, ΔP = 4.13 bar, and for ϵ_0 = 0.27.

Figure 31a and Fig. 31b show (a) Im H_{II} and (b) Im H_{IJ} as functions of excitation frequency. Figure 31a shows that $Im(H_{xx}) = \Omega C_{xx}$. Therefore the slope of Fig. 31a produces the direct damping coefficient.

As shown in Fig. 31b, as excitation frequency increases, the imaginary cross-coupled dynamic stiffness components are approximately equal and opposite implying that $C_{xy} \cong -C_{yx}$. The slopes of Fig. 31b produce the cross-coupled damping coefficients.

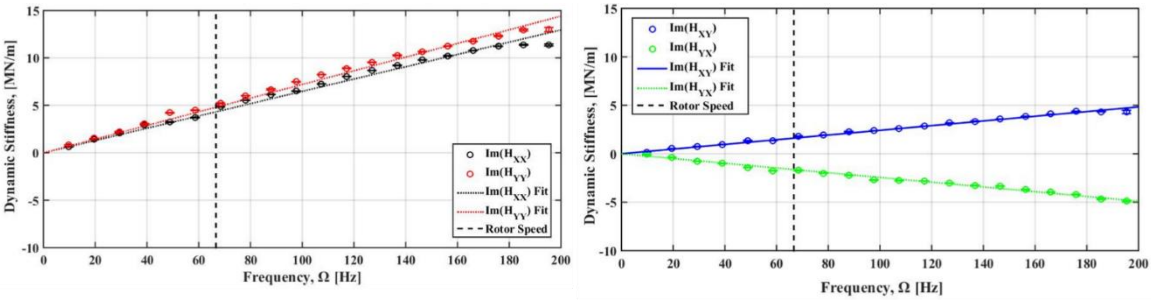

(a) (b)

Figure 31. Imaginary component of the (a) direct and (b) cross-coupled stiffness for the zero pre-swirl insert vs. excitation frequency, Ω, for ω = 4 krpm, *ΔP* = 4.13 bar, and for ϵ_0 = 0.27.

5.2 Rotordynamic Stiffness Coefficients

5.2.1 Direct Stiffness Coefficients

For the zero pre-swirl insert, Fig. 32 shows a representative relationship between K_{xx} and $K_{yy,}$ and ϵ_0. Figure 32a shows the weak correlation between ϵ_0 and K_{yy} until $\epsilon_0 > 0.5$ at which point K_{yy} increases significantly. K_{yy} remains positive for all values of ω and ϵ_0. Figure 32a also shows that $K_{yy} > 0$ for most of the measured values of K_{yy}. Figure 32b shows the lack of relationship between K_{xx} and ϵ_0. K_{xx} is clearly independent of ϵ_0 until 0.5. At ϵ_0 = 0.8, and ω < 8 krpm, K_{xx} is negative. For low values of ϵ_0, $K_{xx} \approx K_{yy}$, but for large values of ϵ_0, $K_{yy} > K_{xx}$.

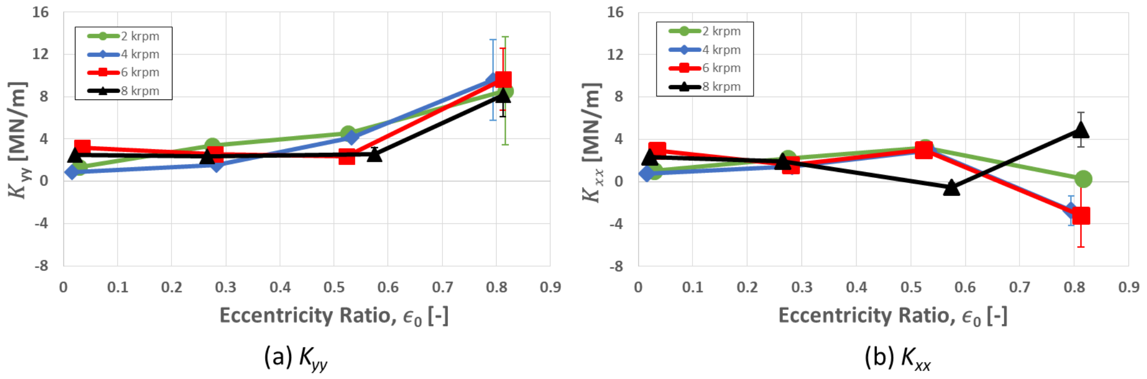

Figure 32. (a) K_{yy} and (b) K_{xx} vs. ϵ_0 for the zero pre-swirl insert at ΔP = 8.27 bar.

For the high pre-swirl insert, Fig. 33 shows a representative relationship between K_{xx} and $K_{yy,}$ and ϵ_0. Figure 33a shows that K_{yy} generally follows the same trend for both the zero and high pre-swirl insert. Comparing Fig. 32b and Fig. 33b, K_{xx} is independent of the imposed pre-swirl condition. K_{xx} and K_{yy} shown in Fig. 33 are slightly lower when compared to those shown in Fig. 32. Overall, the pre-swirl inserts had very little effect on K_{xx} and K_{yy}.

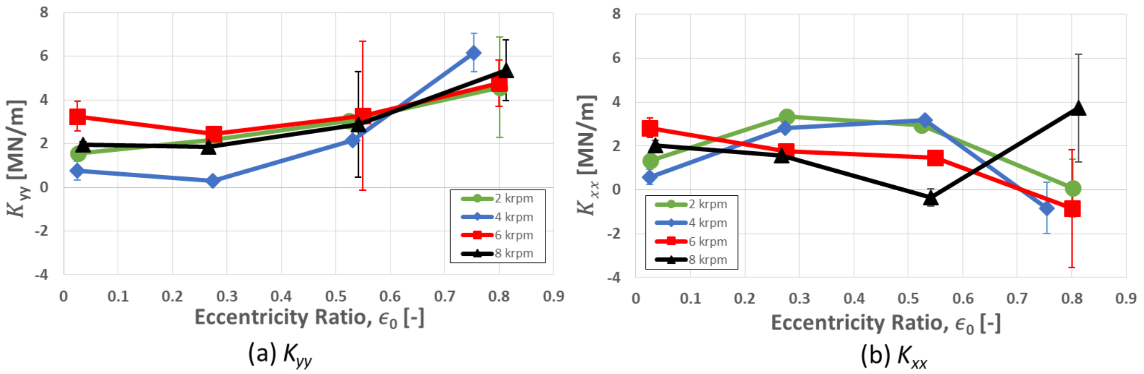

Figure 33. (a) K_{yy} and (b) K_{xx} vs. ϵ_0 for the high pre-swirl insert at ΔP = 8.27 bar.

Figure 34 shows representative relationships between ΔP and the direct stiffness. For low ΔP, K_{xx} and K_{yy} are negative for ω > 2krpm. These negative values of direct stiffness indicate that a pump supported by the seals would have a lower natural frequency at this operating point, which would tend to destabilize the pump rotor. Figure 34 shows that as ΔP increases, the direct stiffness generally increases except for ω = 2 krpm where the stiffness dramatically decreases between ΔP = 4.13 bar and ΔP = 6.21 bar.

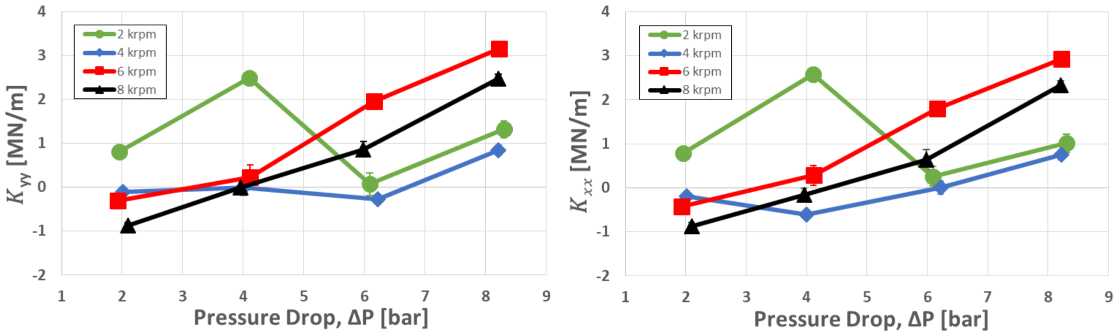

(a) K_{yy} (b) K_{xx}

Figure 34. (a) K_{yy} and (b) K_{xx} vs. ΔP for the zero pre-swirl insert at $\epsilon_0 = 0.00$.

Figure 35 shows K_{yy}, K_{xx}, and Re versus ΔP at the centered position. The Reynolds number is mostly transitional for this data set. The significant drop in K_{xx}, and K_{yy}, occurs as the Reynolds number traverses the transitional regime. As the Reynolds number continues to increase towards the turbulent regime, the rotordynamic stiffness begins increasing with increasing ΔP.

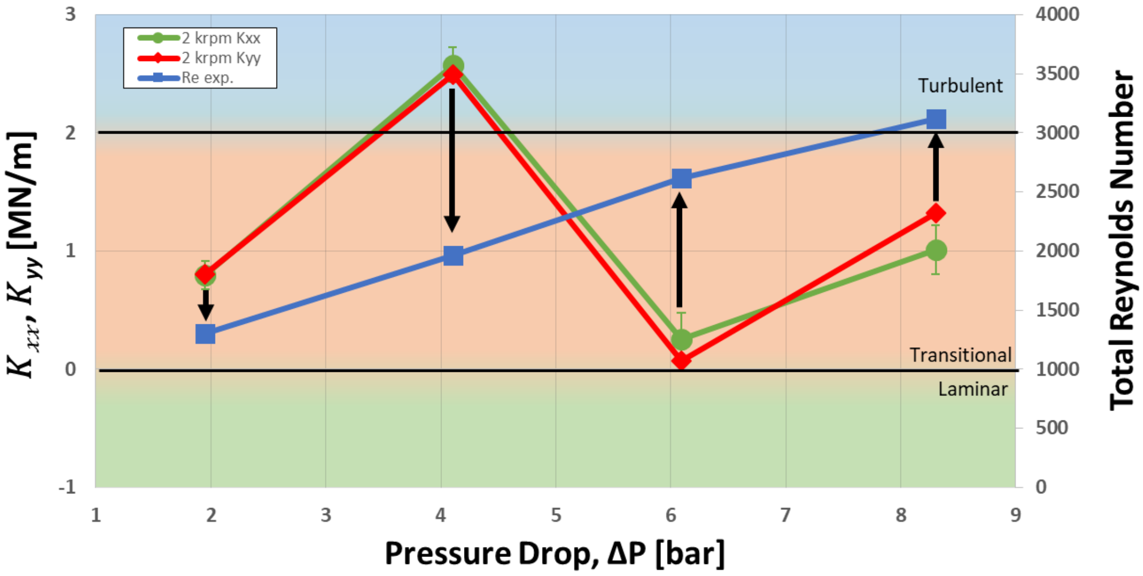

Figure 35. ***K_{yy}*** **and** ***K_{xx}*** **vs. Δ*P* for ω = 2 krpm and** ***ϵ_0*** **= 0.00 for the data set from Fig. 33 overlaid with Reynolds Numbers.**

5.2.2 Cross-coupled Stiffness Coefficients

For the zero pre-swirl insert, Fig. 36 shows a representative relationship between K_{xy} and K_{yx}, and ϵ_0. Figure 36a shows that K_{xy} is generally unaffected by increasing values of ϵ_0. Figure 36b shows that K_{yx} is unaffected by increasing values of ϵ_0 until ϵ_0 = 0.80 where K_{yx} rapidly increases in magnitude. Figure 36 shows that for ϵ_0 < 0.80, K_{xy} and K_{yx} diverge, and increase in magnitude. Figure 36 shows that as ω increases, $\left|K_{xy} - K_{yx}\right|$ increases in magnitude; hence recalling the earlier discussion, the seal forces become increasingly destabilizing. Except for ω = 2 krpm, K_{xy} and K_{yx} have opposite signs throughout the entire data range.

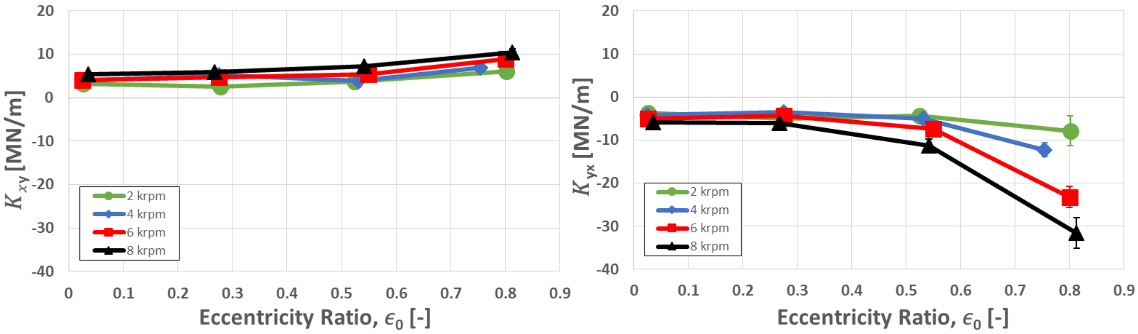

(a) K_{xy} (b) K_{yx}

Figure 36. (a) K_{xy} and (b) K_{yx} vs. ϵ_0 for the zero pre-swirl insert at ΔP = 8.27 bar.

For the high pre-swirl insert, Fig. 37 shows representative relationships between K_{xy} and K_{yx} and ϵ_0. The data for the high pre-swirl insert in Fig. 37 follows the same trends as Fig. 36 for the zero pre-swirl insert. For ϵ_0 < 0.80, the cross-coupled stiffnesses diverge, increase in magnitude, and $K_{xy} \cong -K_{yx}$. At ϵ_0 = 0.80, K_{xy} and K_{yx} diverge for ω = 6 krpm and 8 krpm. At low values of ϵ_0, $|K_{xy}|$ and $|K_{yx}|$ are noticeably larger in magnitude for the high pre-swirl insert data shown in Fig. 37 than the zero pre-swirl insert data shown in Fig. 36.

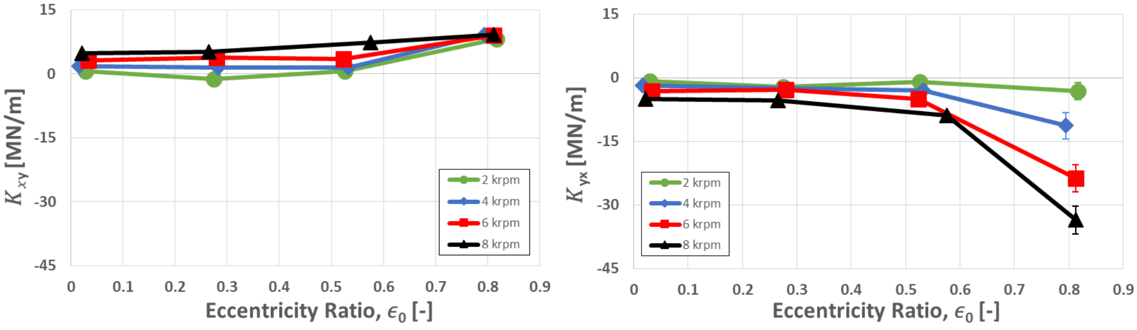

(a) K_{xy} (b) K_{yx}

Figure 37. (a) K_{xy} and (b) K_{yx} vs. ϵ_0 for the high pre-swirl insert at ΔP = 8.27 bar.

Figure 38 shows representative relationships between K_{xy} and K_{yx}, and ΔP. Figure 38a shows that, as speed increases, K_{xy} increases in magnitude. Figure 38b shows that as speed increases, $|K_{yx}|$ also increases in magnitude. Figure 38 shows that there is relatively little relation between cross-coupled stiffness and ΔP, and that $K_{xy} = |-K_{yx}|$.

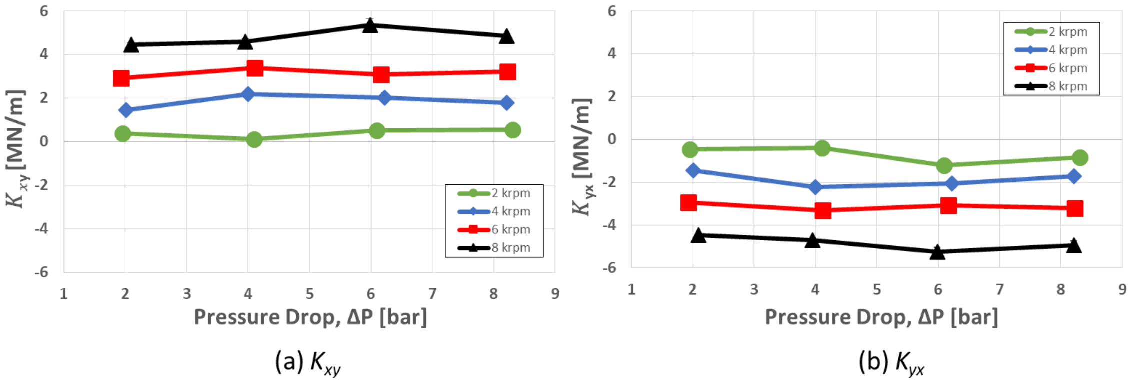

(a) K_{xy} (b) K_{yx}

Figure 38. (a) K_{xy} and (b) K_{yx} vs. ΔP for the zero pre-swirl insert at ϵ_0 = 0.00.

5.2.3 Pre-swirl Effects on Stiffness Coefficients

Figure 39 shows K_{xx}, K_{yy}, K_{xy}, and K_{yx} versus PSR for ω = 6 krpm, ΔP = 8.27 bar, and ϵ_0 = 0.53. Each connected point in Fig. 39 is for a different pre-swirl insert for the same test conditions. (i.e. the left most point is for the zero pre-swirl insert, the middle point is the medium pre-swirl insert, and the far right data point is the high pre-swirl insert.)

As PSR increases, K_{yy} generally increases and K_{xx} generally decreases. For low values of PSR, $K_{yy} \approx K_{xx}$, but as PSR increases, $K_{yy} > K_{xx}$. For most test points, the direct stiffness does not show a clear increasing trend until the PSR is greater than 0.3. As PSR increases, $|K_{xy} - K_{yx}|$ increases, creating more seal destabilizing reaction forces.

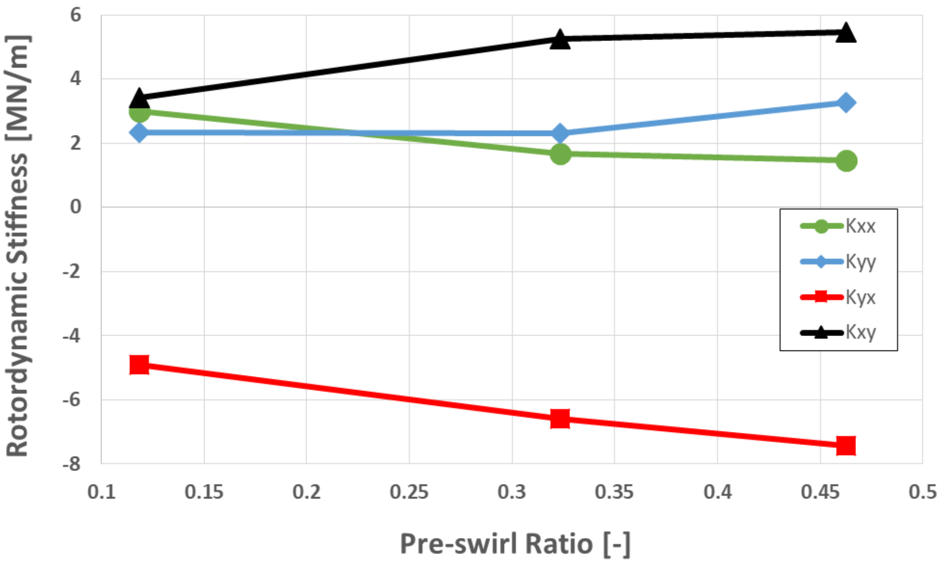

Figure 39. K_{xx}, K_{xy}, K_{yx}, *and* K_{yy} **vs. PSR for three pre-swirl inserts at ω = 6 krpm,** ΔP **= 8.27 bar, and** ϵ_0 **= 0.53.**

5.3 Rotordynamic Damping Coefficients

5.3.1. Direct Damping Coefficients

For the zero pre-swirl insert, Fig. 40 shows a representative relationship between C_{xx}, C_{yy}, and ϵ_0, for ϵ_0 > 0.53, Fig. 40a shows that C_{xx} increases with increasing ω. Contrary to C_{xx} in Fig. 40a, C_{yy} in Fig. 40b decreases with increasing ω. For the data shown in Fig. 40, the direct damping values are largely unaffected by increasing ϵ_0 until ϵ_0 > 0.53 at which point they increase significantly. Until this change at ϵ_0 > 0.53, $C_{xx} \approx C_{yy}$.

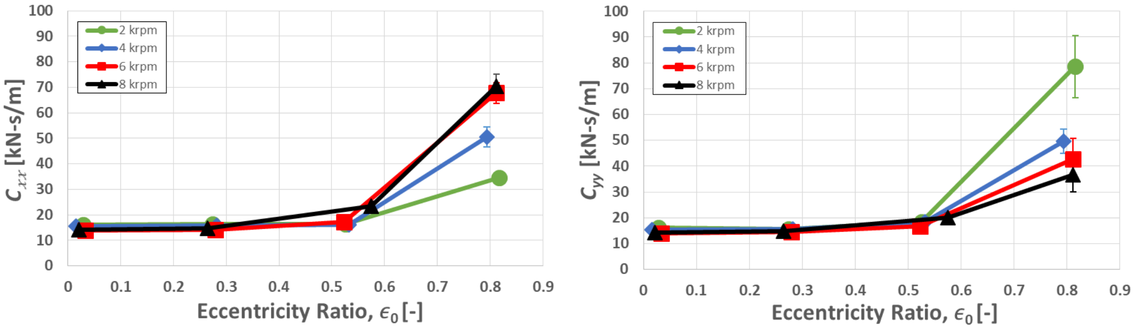

(a) C_{xx} (b) C_{yy}

Figure 40. (a) C_{xx} and (b) C_{yy} vs. ϵ_0 for the zero pre-swirl insert at ΔP = 8.27 bar.

Figure 41 shows the same data range for the high pre-swirl insert as Fig. 40 for the zero pre-swirl insert. C_{xx} values shown in Fig. 41a for the high pre-swirl insert are approximately equal to that of the zero pre-swirl insert shown in Fig. 40a. C_{yy} shown in Fig. 41b is lower for the high pre-swirl insert than the comparable values in Fig. 40b , particularly at higher values of ϵ_0 and low values of ω. Overall the trends for Fig. 41 are very similar to those of the zero pre-swirl insert in Fig. 40. Figure 41 also shows that for the high pre-swirl insert, C_{xx} and C_{yy} are less dependent on ω than the zero pre-swirl insert.

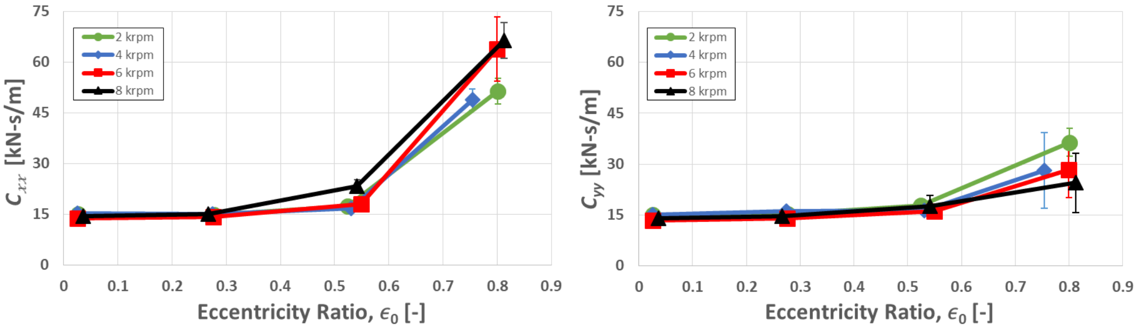

(a) C_{xx} (b) C_{yy}

Figure 41. (a) C_{xx} and (b) C_{yy} vs. ϵ_0 for the high pre-swirl insert at ΔP = 8.27 bar.

For the zero pre-swirl insert, Fig. 42 shows a representative relationship between C_{xx}, C_{yy}, and ΔP. As ΔP increases, the direct damping increases in magnitude. In general, $C_{xx} = C_{yy}$, and there is no clear trend between ω and direct damping.

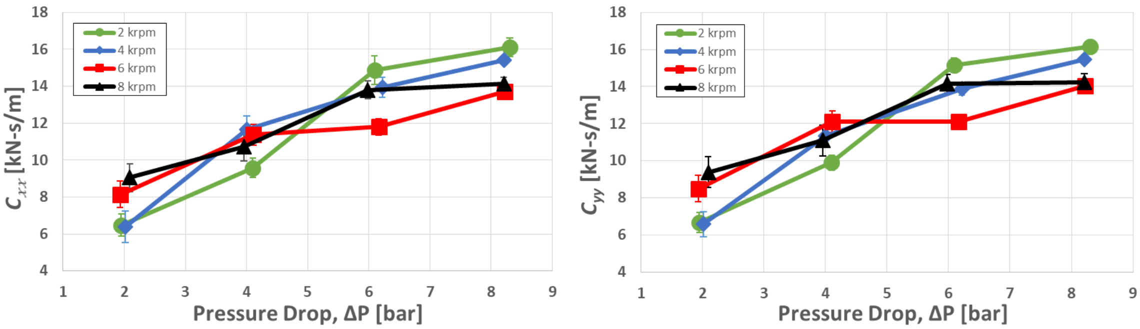

(a) C_{xx} (b) C_{yy}

Figure 42. (a) C_{xx} and (b) C_{yy} vs. ΔP for the zero pre-swirl insert at $\epsilon_0 = 0.00$.

5.3.2. Cross-coupled Damping Coefficients

Figure 43 shows that for low ϵ_0, $C_{xy} \cong |C_{yx}|$ particularly for low ω. Overall, the cross-coupled damping increases in magnitude with increasing ϵ_0. When C_{xy} and C_{yx} have opposite signs, the cross-coupled damping acts as gyroscopic terms and do not dissipate energy. When $\epsilon_0 >$ ~0.6 C_{xy}, C_{yx} have the same sign, and hence dissipate energy. The cross-coupled damping was approximately equal for the zero, medium and high pre-swirl inserts.

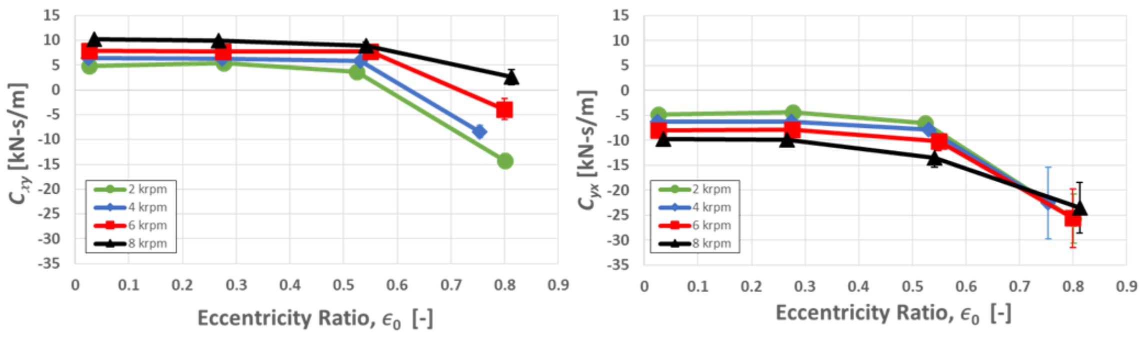

(a) C_{xy} (b) C_{yx}

Figure 43. (a) C_{xy} and (b) C_{yx} vs. ϵ_0 for the zero pre-swirl insert at ΔP = 8.27 bar.

Figure 44a shows that as ω increases, C_{xy} increases in magnitude. Figure 44b shows that as ω increases, $|C_{yx}|$ also increases in magnitude. Figure 44 shows that there is relatively little correlation between cross-coupled damping and ΔP, and that $C_{xy} = |-C_{yx}|$. As before, when C_{xy} and C_{yx} have opposite signs, the cross-coupled damping acts as gyroscopic terms and do not dissipate energy.

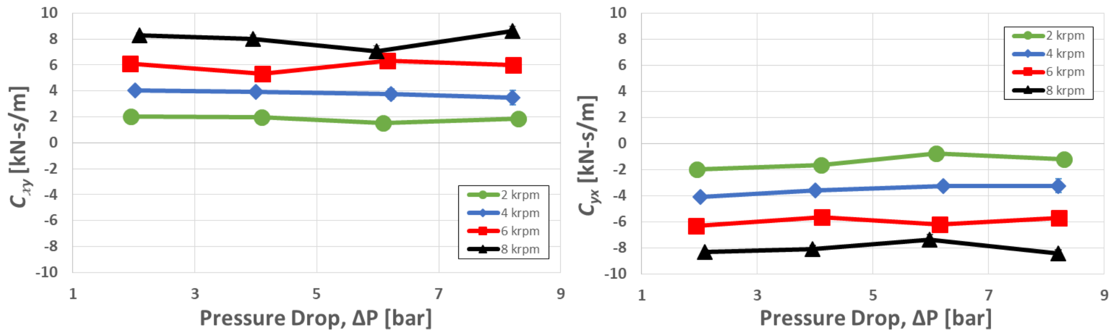

(a) C_{xy} (b) C_{yx}

Figure 44. (a) C_{xy} and (b) C_{yx} vs. ΔP for the zero pre-swirl insert at ϵ_0 = 0.00.

5.3.3. Pre-swirl Effects on Damping Coefficients

Figure 45 shows C_{xx}, C_{yy}, C_{xy}, and C_{yx} versus PSR for ω = 6 krpm, ΔP = 8.27 bar, and ϵ_0 = 0.53. Each connected data point in Fig. 45 is for a different pre-swirl insert for the same test conditions. (i.e. the left most point is for the zero pre-swirl insert, the middle point is the medium pre-swirl insert, and the far right data point is the high pre-swirl insert.) As PSR increases, C_{xx} and C_{yy} diverge slightly, but stay relatively equal. Figure 45 also shows that as PSR increases, C_{xy} and C_{yx} diverge slightly but are approximately equal in magnitude. Overall the rotordynamic damping coefficients appear to be largely unaffected by increasing PSR.

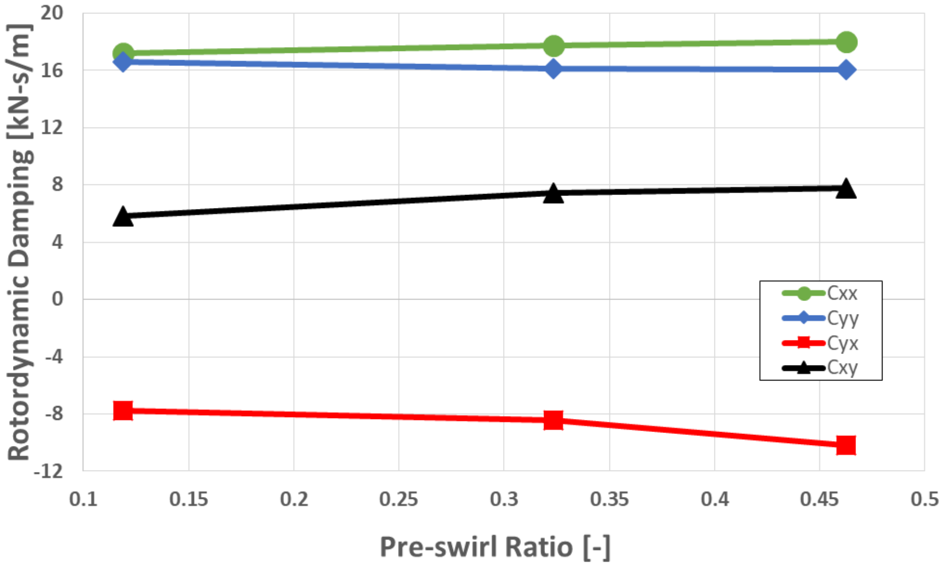

Figure 45. C_{xx}, C_{xy}, C_{yx}, **and** C_{yy} **vs. PSR for three pre-swirl inserts at ω = 6 krpm,** ΔP **= 8.27 bar, and** ϵ_0 **= 0.53.**

5.4 Rotordynamic Virtual Mass Coefficients

5.4.1. Direct Virtual Mass Coefficients

Figure 46a shows that for the zero pre-swirl insert, there is relatively little change in M_{xx} until $\epsilon_0 > 0.53$, at which point M_{xx} increases by a factor of ~1.5. Figure 46b shows that for ω < 8 krpm, there is relatively little change in M_{yy} until ϵ_0 > 0.53. When comparing Fig. 46a and Fig. 46b $M_{yy} > M_{xx}$ for ϵ_0 > 0.5 and $M_{xx} \cong M_{yy}$ for $\epsilon_0 \leq 0.5$, Fig. 46 also shows that generally, M_{xx} increases and M_{yy} decreases with increasing ω.

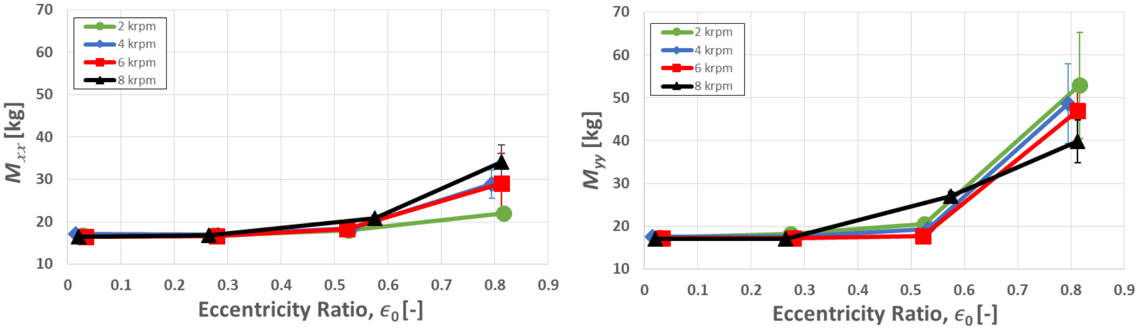

(a) M_{xx} (b) M_{yy}

Figure 46. (a) M_{xx} and (b) M_{yy} vs. ϵ_0 for the zero pre-swirl insert at ΔP = 8.27 bar.

The values of M_{xx} presented in Fig. 47a for the high pre-swirl insert have a similar trend and are approximately equal in magnitude to that for the zero pre-swirl insert presented in Figure 46 46a. Compared to the data presented in Fig. 46b, the data presented in Fig. 47b shows a reduced dependence between M_{yy} and ϵ_0. For ϵ_0 < 0.53, M_{yy} is approximately equal for the zero pre-swirl insert shown in Fig. 46b and the high pre-swirl insert in Fig. 47b. At ϵ_0 = 0.5, and for ω > 6 krpm, M_{yy} is ~25% greater for the high pre-swirl insert than for the zero pre-swirl insert, but for ϵ_0 = 0.80 M_{yy} is ~50% less than that of the zero pre-swirl insert.

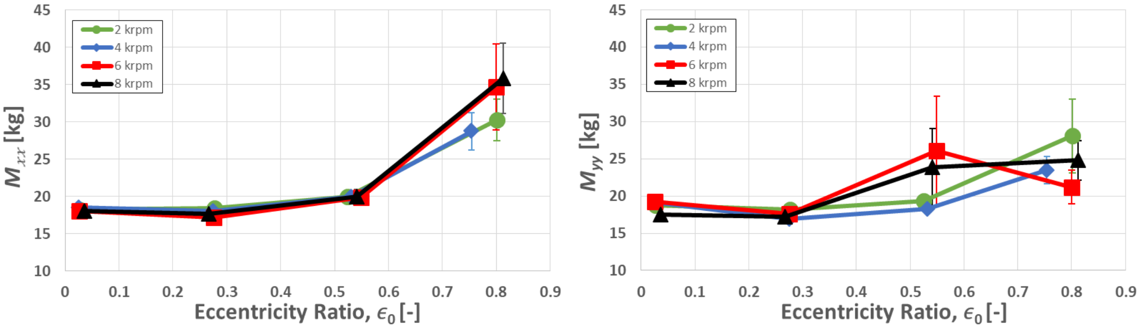

(a) M_{xx} (b) M_{yy}

Figure 47. (a) M_{xx} and (b) M_{yy} vs. ϵ_0 for the high pre-swirl insert at ΔP = 8.27 bar.

For the zero pre-swirl insert, Fig. 48 shows a representative relationship between M_{xx}, M_{yy}, and ΔP. As ΔP increases, $M_{xx}$and M_{yy} converge to ~17 kg. In general, as ω increases, M_{xx}, and M_{yy} are less dependent on ΔP.

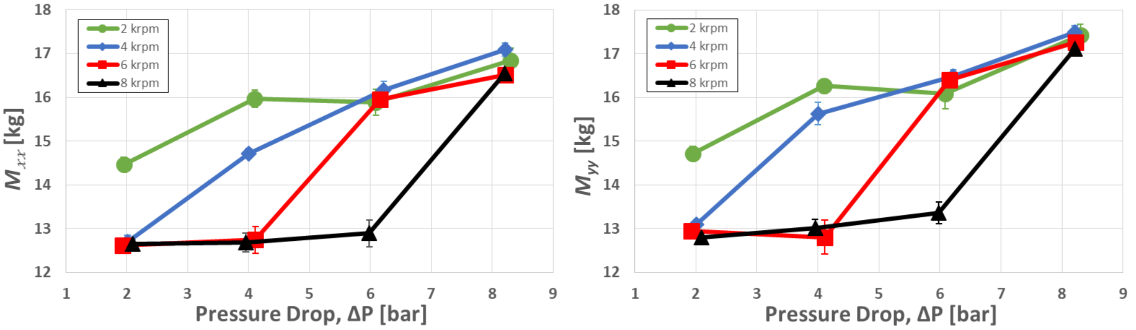

(a) M_{xx} (b) M_{yy}

Figure 48. (a) M_{xx} and (b) M_{yy} vs. ΔP for the zero pre-swirl insert at ϵ_0 = 0.00.

5.4.2. Cross-coupled Virtual Mass Coefficients

For the zero pre-swirl insert, Fig. 49 shows a representative relationship for M_{yx} and M_{xy} and ϵ_0. Figure 49a shows that M_{xy} is negative, and relatively unaffected by increasing ϵ_0. Figure

49b shows that M_{yx} is negative and unaffected by increasing ϵ_0 until 0.5. As seen in Fig. 49b, for ϵ_0 > 0.5, M_{yx} rapidly increases in magnitude. Note for all ϵ_0, the values of the M_{yx} and M_{xy} remain negative have the same sign, and have approximately equivalent magnitudes and thus minimal impact on the overall stability.

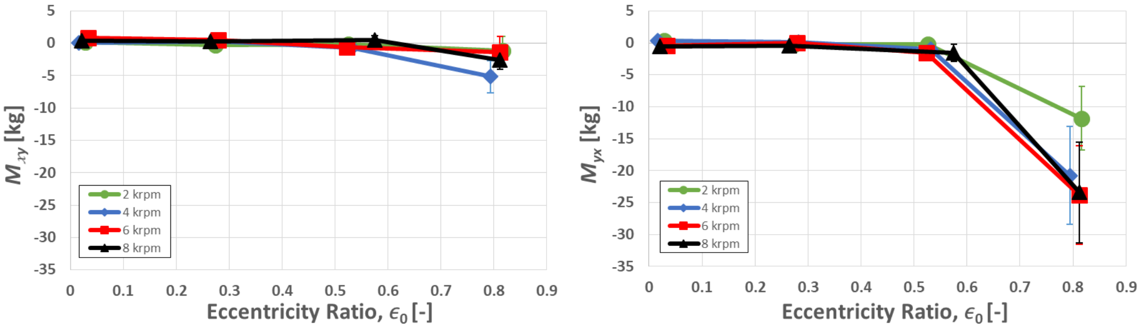

(a) M_{xy} (b) M_{yx}

Figure 49. (a) M_{xy} and (b) M_{yx} vs. ϵ_0 for the zero pre-swirl insert at ΔP = 8.27 bar.

For the high pre-swirl insert, Fig. 50 shows a representative relationships between M_{yx} and M_{xy} and ϵ_0. Figure 50a and Fig. 50b are nearly identical for the zero and high pre-swirl insert. The main difference is the reduction in magnitude of M_{yx} for ω greater than 4 krpm for the high pre-swirl insert. The values of the M_{yx} and M_{xy} are generally negative and have the same sign, and thus no impact on the overall stability.

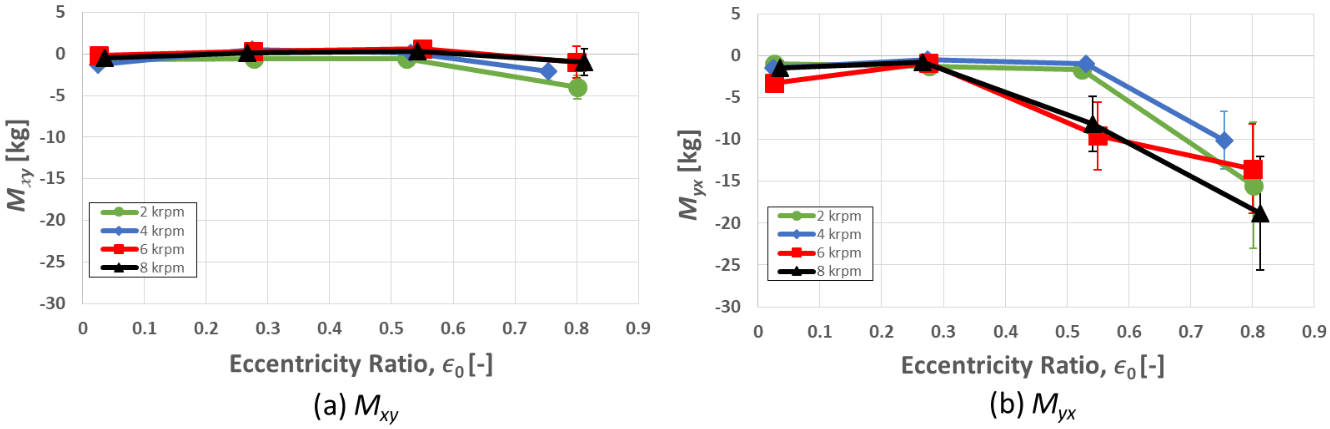

(a) M_{xy} (b) M_{yx}

Figure 50. (a) M_{xy} and (b) M_{yx} vs. ϵ_0 for the high pre-swirl insert at ΔP = 8.27 bar.

For the zero pre-swirl insert, Fig. 51 shows a representative relationship between M_{xy}, M_{yx}, and ΔP at ϵ_0 = 0.00. M_{xy} and M_{yx} are relatively unaffected by increasing ΔP. M_{xy} and $|M_{yx}|$ increase with increasing ω. Generally, when ϵ_0 < 0.53, M_{xy} and M_{yx} are both approximately equal in magnitude, and have opposite signs. The differing signs for M_{xy} and M_{yx} will directly impact the stability of the seal. These terms are accounted for in C_{eff} to be discussed in Section 5.6.

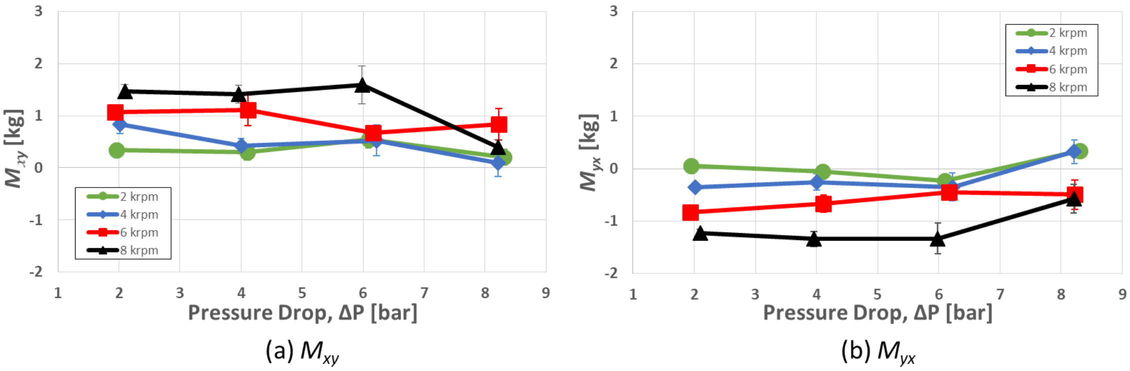

(a) M_{xy} (b) M_{yx}

Figure 51. (a) M_{xy} and (b) M_{yx} vs. ΔP for the zero pre-swirl insert at ϵ_0 = 0.00.

5.4.3. Pre-swirl Effects on Virtual Mass Coefficients

Figure 52 shows M_{xx},, M_{yy}, M_{xy}, and M_{yx} versus imposed PSR for ω = 6 krpm, ΔP = 8.27 bar, and ϵ_0 = 0.53. Each connected data point in Fig. 52 is for a different pre-swirl insert for the same test conditions. (i.e. the left most point is for the zero pre-swirl insert, the middle point is the medium pre-swirl insert, and the far right data point is the high pre-swirl insert.) As PSR increases, M_{yy} increases while M_{xx} remains relatively constant. The cross-coupled virtual mass shows a similar trend as the direct terms; M_{xy} is approximately zero for the entire range, while M_{yx} steadily decreases in value for the range of imposed pre-swirls.

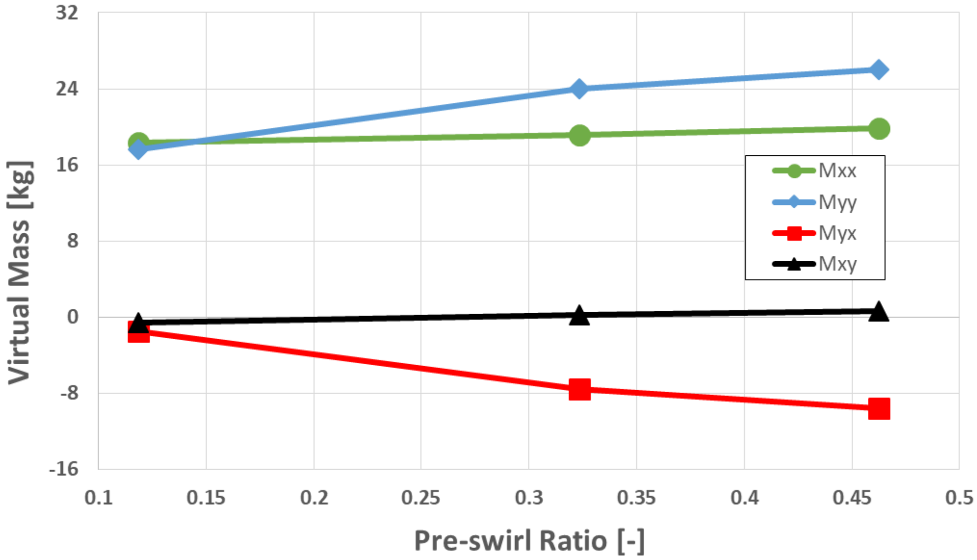

Figure 52. ***M_{xx}*, *M_{xy}*, *M_{yx}*, and *M_{yy}* vs. PSR for three pre-swirl inserts at ω = 6 krpm, *ΔP* = 8.27 bar, and *ϵ_0* = 0.53.**

5.5 Whirl Frequency Ratio

Lund [9] defined the whirl-frequency ratio, f_w, as a function of the rotordynamic coefficients for a flexible rotor supported on plain journal bearings, as,

$$OSI = \frac{\omega_n}{f_w} \tag{24}$$

where ω_n is the first flexural natural frequency and OSI is the onset speed of instability. f_w is useful for defining seal performance for a single geometry at various operating conditions. For most of the tested points, M_{xy} and M_{yx} have differing signs meaning that they were not negligible and we have to use the extended model provided by San Andrés et al. [27]

For the zero pre-swirl insert, Fig. 53a shows that f_w is not strongly dependent on ϵ_0. An interesting observation is that in Fig. 53a, f_w increases as ω increases; however, for the high pre-swirl insert, Fig. 53b shows that f_w decreases as ω increases. For the various pre-swirl inserts, as ω increases, f_w tends to converge to ~0.4-0.6. In general, the high pre-swirl insert has a f_w greater than 0.5. For $\omega = 2$ krpm, f_w is impacted by the increase in PSR from the high pre-swirl insert. For $\omega > 2$ krpm, f_w is generally unaffected by the increase in PSR.

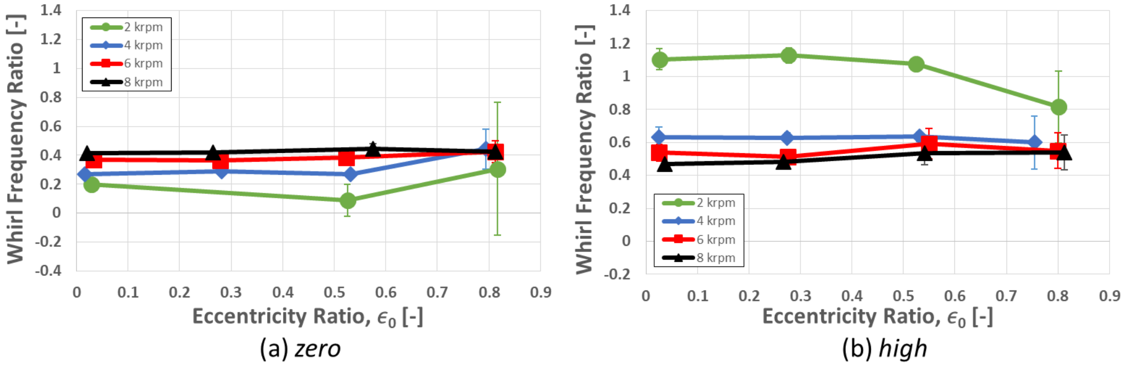

(a) *zero* (b) *high*

Figure 53. f_w vs. ϵ_0 for the (a) zero and (b) high pre-swirl insert at $\Delta P = 8.27$ bar. Note the excluded point in (a) at $\epsilon_0 = 0.27$.

Figure 54a and Fig. 54b shows f_w versus ΔP for the zero and high pre-swirl insert respectively. Figure 54a shows that f_w drops with increasing ΔP. For the high pre-swirl insert, Fig. 54b shows as ΔP increases, f_w increases significantly for ω = 2 krpm.

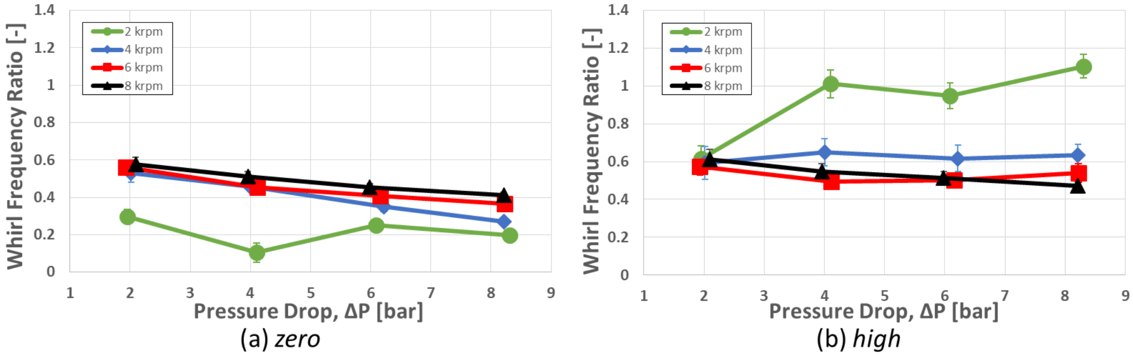

(a) *zero* (b) *high*

Figure 54. f_w **vs.** ΔP **for the (a) zero and (b) high pre-swirl insert at** $\epsilon_0 = 0.00$**.**

Figure 55 shows f_w versus PSR for ω = 6 krpm, ΔP = 8.27 bar, and ϵ_0 = 0.53. Note that the relationship behaves differently for low ω. At ω = 2 krpm and ω = 4 krpm, f_w increases with increasing PSR. For ω = 6 krpm and ω = 8 krpm, as ω increases, f_w appears to converge to ~0.5. Note that for both the medium and high pre-swirl inserts, $f_w > 0.5$; meaning that the seals exhibit stability characteristics worse than that of a plain journal bearing (~0.5).

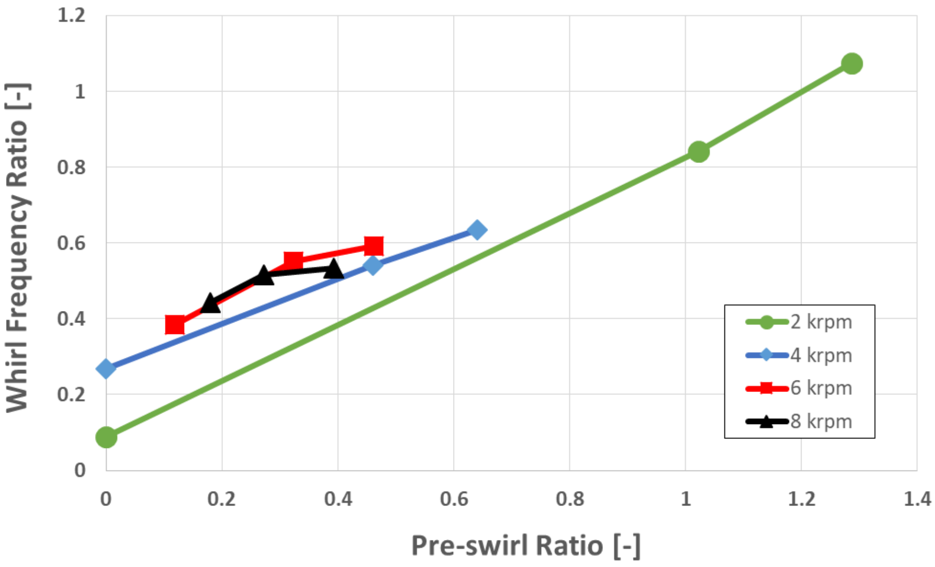

Figure 55. f_w **vs. PSR for the three pre-swirl inserts for** ΔP **= 8.27 bar, and** ϵ_0 **= 0.53.**

5.6 Effective Damping Coefficients

When comparing annular seals, a more stabilizing seal will exhibit higher values of effective damping for the full range of operating conditions for $\epsilon_0 = 0.0$. Effective damping C_{eff} is defined as,

$$C_{eff} = C - \frac{k}{\omega} + m\omega \tag{25}$$

where $C = C_{xx} = C_{yy}$, $k = K_{xy} = -K_{yx}$, and $m = M_{xy} = -M_{yx}$ will be used to compare the rotordynamic characteristics of the different tests performed about a centered orbit.

Figure 56 shows that C_{eff} generally increases with increasing ΔP, except for the medium and high pre-swirl insert at ω = 2 krpm in Fig. 56a. Overall, Fig. 56a and Fig. 56b shows that C_{eff} decreases significantly at lower speeds in moving from the zero to the medium to the high pre-swirl insert. Figure 56a and Fig. 56b shows that for ω = 2 krpm and ω = 4 krpm, the most stable seal configuration was the zero pre-swirl insert. Note that as ω increases, the choice of pre-swirl insert has less effect on C_{eff}. Figure 56c and Fig. 56d show that for ω = 6 krpm and ω = 8 krpm there is almost no difference between the values of C_{eff} for the zero, medium and high pre-swirl insert.

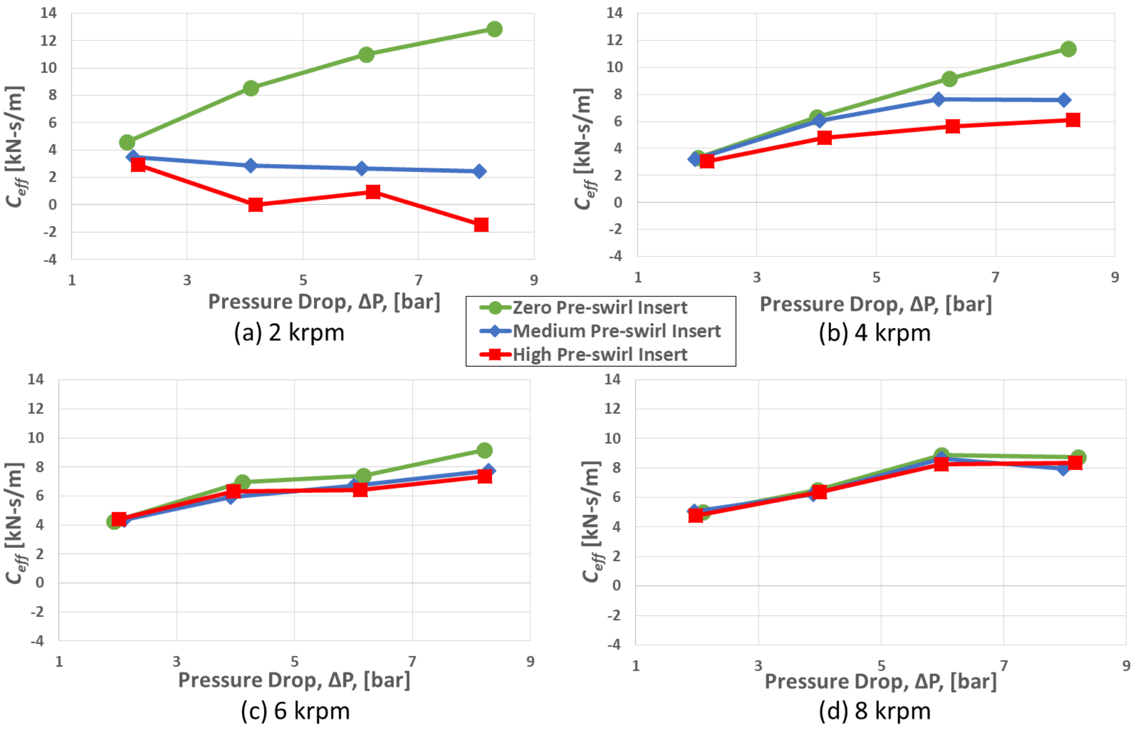

(a) 2 krpm

(b) 4 krpm

(c) 6 krpm

(d) 8 krpm

Figure 56. C_{eff} vs. ΔP for (a) 2, (b) 4, (c) 6, and (d) 8 krpm.

Figure 57 shows C_{eff} versus ω for each of the tested centered data points. For ΔP = 2.1 bar, Fig. 57a shows that changing ω has little to no effect on C_{eff}. For ω = 8 krpm, Fig. 57 shows that C_{eff} is relatively unaffected by increasing ΔP. Note that in Fig. 57b, Fig. 57c, and Fig. 57d the zero pre-swirl insert's C_{eff} tends to be a decreasing function of ω while the medium and high pre-swirl insert's C_{eff} are increasing functions of ω. In general, Fig. 57 shows that at high ω, C_{eff} tends to converge to similar value independent of the imposed pre-swirl. Overall, for the range of tested data, the zero pre-swirl insert provides the most stable configuration. As pre-swirl increases, C_{eff} drops.

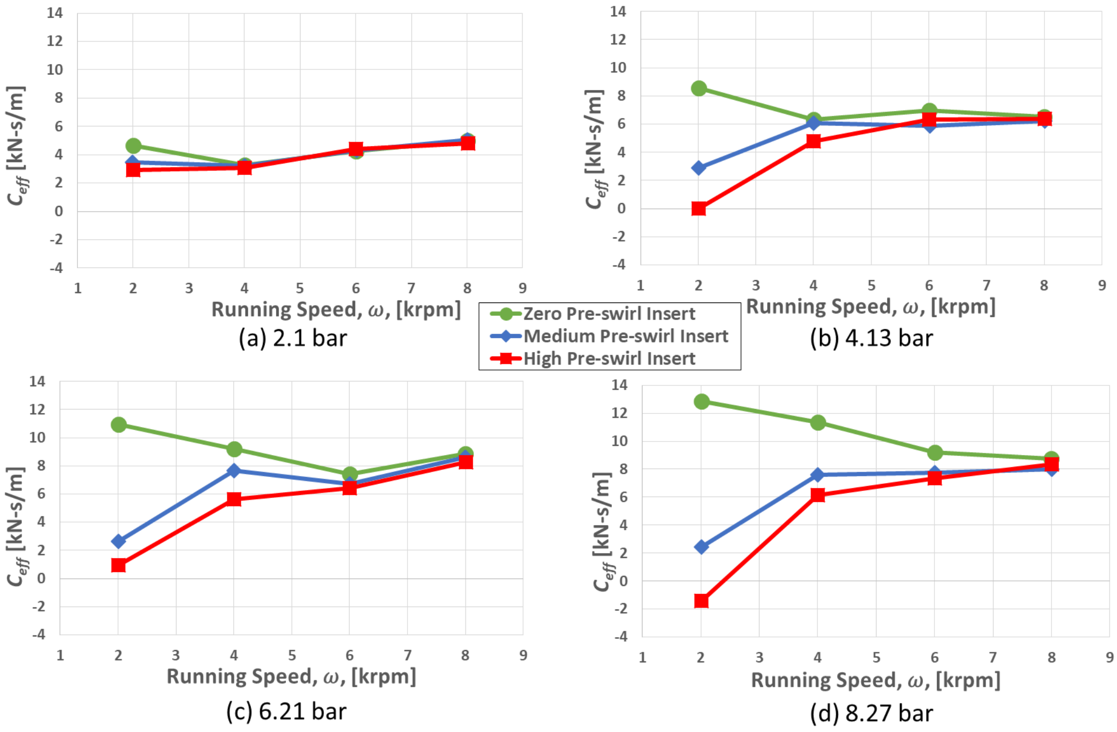

(a) 2.1 bar

(b) 4.13 bar

(c) 6.21 bar

(d) 8.27 bar

Figure 57. C_{eff} vs. ω for Δ*P* = (a) 2.1, (b) 4.13, (c) 6.21, and (d) 8.27 bar.

Figure 58 shows C_{eff} vs. PSR for each of the tested ΔPs. Figure 58a shows that PSR has very little effect on C_{eff} for ΔP = 2.1 bar. In moving from Fig. 58b to Fig. 58c to Fig. 58d, as ΔP increases C_{eff} becomes a stronger, decreasing function of PSR. Figure 58 shows that the most stable configuration is the zero pre-swirl insert because the medium and high pre-swirl inserts have significantly reduced values of C_{eff} as PSR increases, and therefore are less stabilizing.

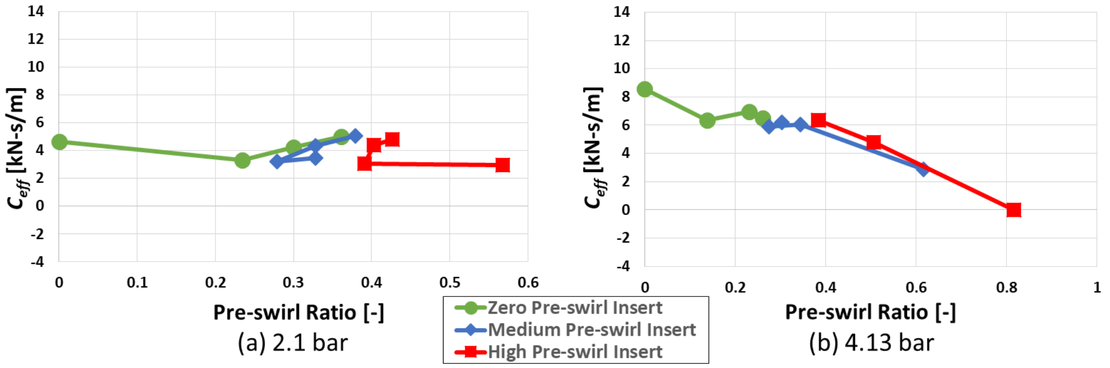

(a) 2.1 bar

(b) 4.13 bar

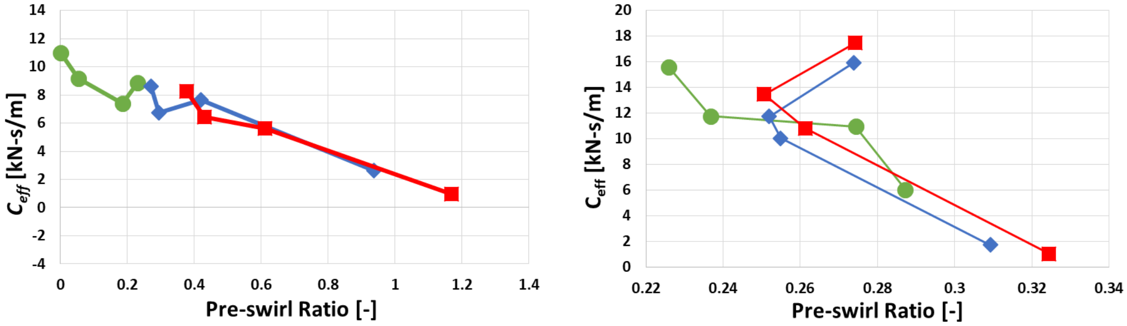

(c) 6.21 bar

(d) 8.27 bar

Figure 58. C_{eff} vs. PSR for ΔP = (a) 2.1, (b) 4.13, (c) 6.21, and (d) 8.27 bar for ϵ_0 = 0.00.

6. MEASUREMENTS VS. PREDICTIONS

6.1 Stiffness Coefficients

6.1a Direct Stiffness Coefficients

Figure 59 shows representative relationships between K_{xx} and K_{yy} for the predicted and experimental results versus ϵ_0 for the zero pre-swirl insert at ω = 2 krpm and ΔP = 8.27 bar. Note that for all figures in Section 6, the measured value of pre-swirl was used for calculating the predicted values presented. K_{xx} and K_{yy} are smaller than predicted for $\epsilon_0 < 0.53$ and larger than predicted above 0.53. For $\epsilon_0 = 0.53$, predicted K_{xx} value very closely approximate the experimental results and were larger than the experimental values by ~6% and then diverge as ϵ_0 approaches 0.80. These relationships are also true for the medium, and high pre-swirl insert. For $\epsilon_0 = 0.00$, the predicted values of K_{xx} are larger than the experimental values by a factor of 3. The total Reynolds number at this location is ~3100. This result indicates that the friction factor model for this set of conditions does not accurately predict the experimental data.

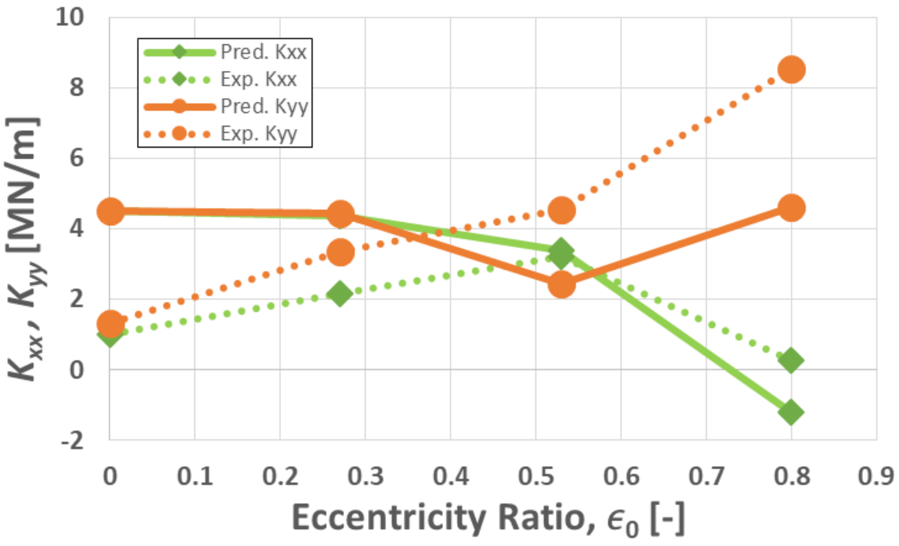

Figure 59. K_{xx} **and** K_{yy} **vs** ϵ_0 **for** ΔP **= 8.27 bar and ω = 2 krpm for the zero pre-swirl insert.**

For the zero pre-swirl insert at ω = 6 krpm and ΔP = 8.27 bar, Fig. 60 show representative relationships for the predicted and experimental relationships of K_{xx} and K_{yy} versus ϵ_0. K_{xx} and K_{yy} predictions more accurately approximate the experimental results at ω = 6 krpm. For ϵ_0 < 0.53, the direct stiffness predictions are off by ~2%. At ϵ_0 > 0.53 the K_{xx} and K_{yy} predictions are larger than the experimental results by ~35-50%. These relationships hold true for the medium, and high pre-swirl insert.

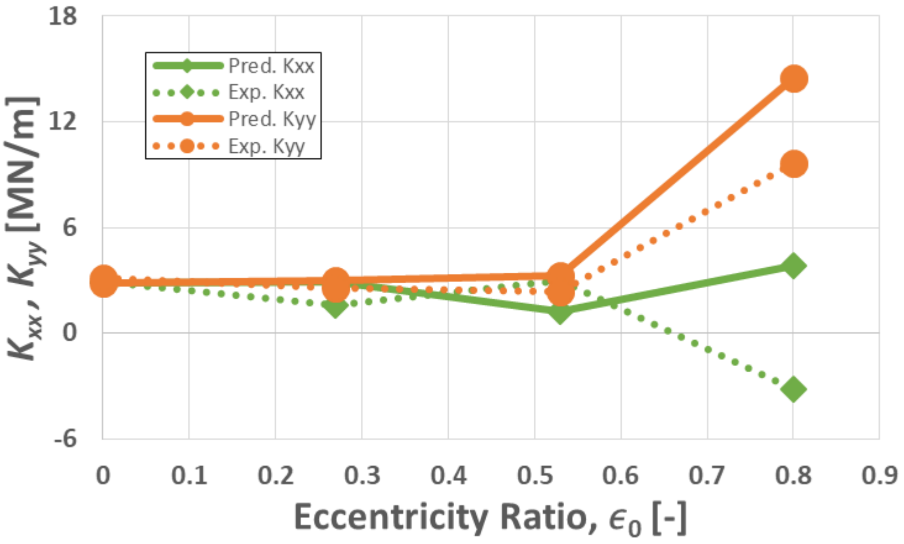

Figure 60. ***K_{xx}*** **and** ***K_{yy}*** **vs** ***ϵ_0*** **for Δ*P* = 8.27 bar and ω = 6 krpm for the zero pre-swirl insert.**

Recall Fig. 35 that depicted the direct stiffness results for ω = 2 krpm, and ϵ_0 =0.00 for the zero pre-swirl insert. Recall that the direct stiffness experienced a significant drop in magnitude between 4.13 bar and 6.21 bar as the Reynolds number traversed the transitional regime. Figure 61 shows the predicted values of K_{xx} and K_{yy} versus Reynolds number for the data set in Fig. 35 and shows no drop in K_{xx} and K_{yy} for the Reynolds number range shown.

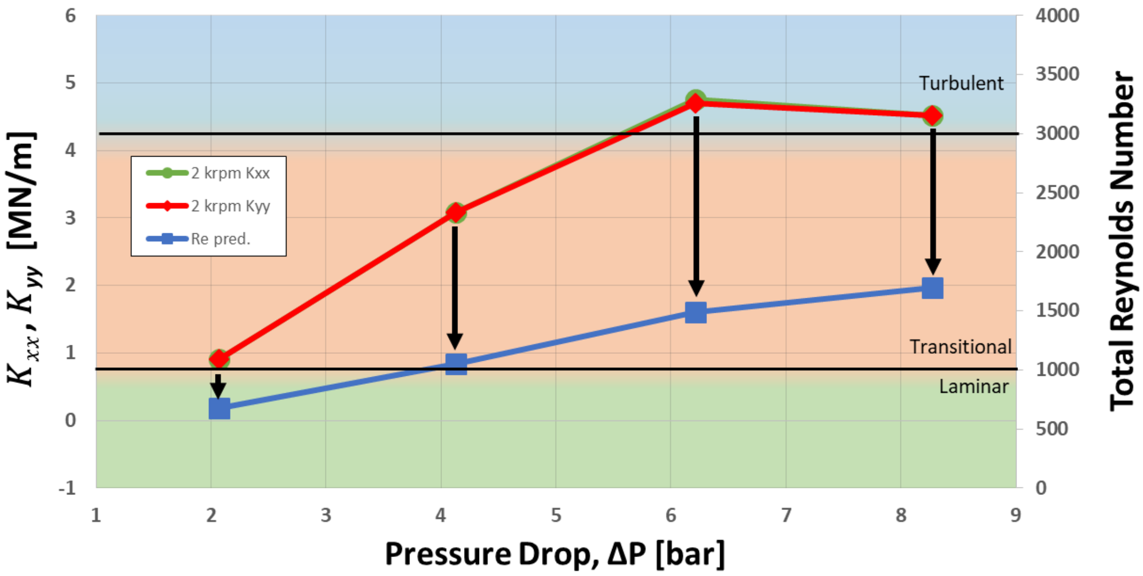

Figure 61. Predicted K_{xx}, K_{yy} and Re vs. ΔP for ϵ_0 = 0.00 and ω = 2 krpm.

For the zero pre-swirl insert at ω = 2 krpm and ϵ_0 = 0.00, Fig. 63 shows representative relationships for the predicted and experimental results of K_{xx} and K_{yy} versus ΔP. In Fig. 63, the predicted values of K_{xx} and K_{yy} are continually increasing with respect to increasing ΔP and $K_{xx} \cong K_{yy}$. The experimental data showed that the direct stiffnesses were equal but experienced a drop at ΔP = 4.13 bar. Looking back at the experimental results in Fig. 35, when ΔP = 2.07 bar, the predicted stiffnesses closely approximate those shown in Fig. 35. Similar to the data presented in Fig. 62, the Reynolds number transitions from laminar to transitional throughout the data presented in Fig. 63. The transition from laminar to transitional is predicted to occur near ΔP = 4.13 bar. Note the predicted values of K_{xx} and K_{yy} are nearly identical and are shown one on top of the other.

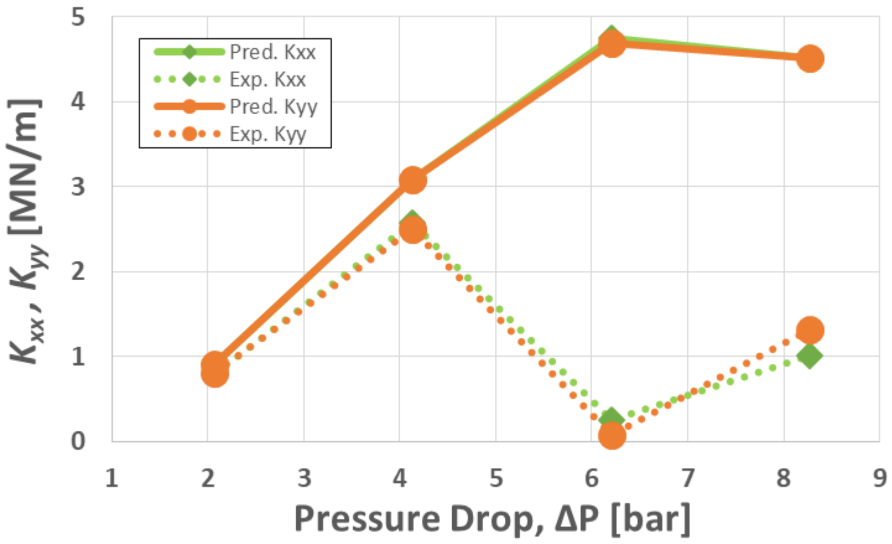

Figure 62. K_{xx} and K_{yy} vs ΔP for ϵ_0 = 0.00 and ω = 2 krpm for the zero pre-swirl insert.

For the zero pre-swirl insert at ω = 2 krpm and ϵ_0 = 0.80, Fig. 63 shows representative relationships for the predicted and experimental results of K_{xx} and K_{yy} versus ΔP. In Fig. 63, the predictions more closely match the experimental data. The magnitude of the experimental values of K_{xx} and K_{yy} are over-predicted by ~50%. Note the ~400% increase in magnitude when ΔP = 8.28 bar. Note that the data presented in Fig. 63 is uncharacteristic for direct stiffness and appears to represent cross-coupled stiffness. Recalling Fig. 59, as you move from ϵ_0 = 0.53 to ϵ_0 = 0.80, there is a large drop in K_{xx}. The negative K_{xx} value seen in Fig. 59 are seen in Fig. 63 for ϵ_0 = 0.80, and ω = 2 krpm, for all of the tested ΔP.

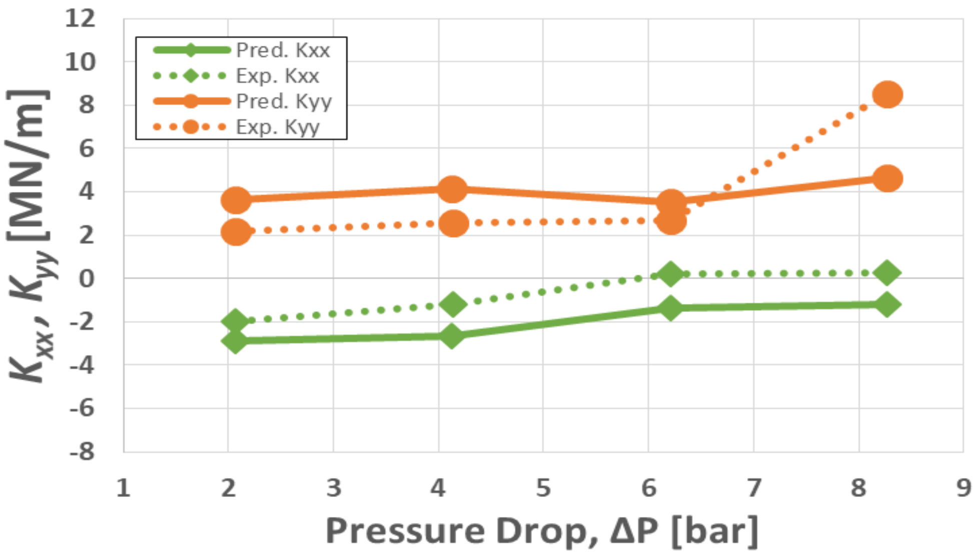

Figure 63. K_{xx} **and** K_{yy} **vs** ΔP **for** ϵ_0**= 0.80 and ω = 2 krpm for the zero pre-swirl insert.**

For the zero pre-swirl insert at ω = 6 krpm and ϵ_0 = 0.00, Fig. 64 shows representative relationships for the predicted and experimental results of K_{xx} and K_{yy} versus ΔP. As ω increases the predictions more closely align with the experimental results. For ΔP = 2.07, the predicted results are positive, while the experimental results were approximately equal in magnitude, but were opposite in sign. Experimental K_{xx} and K_{yy} values are under-predicted, but start to align with the predicted values as ΔP increases. K_{xx} and K_{yy} predictions for the medium, and high pre-swirl insert were similar to those for the zero pre-swirl insert shown in Fig. 64.

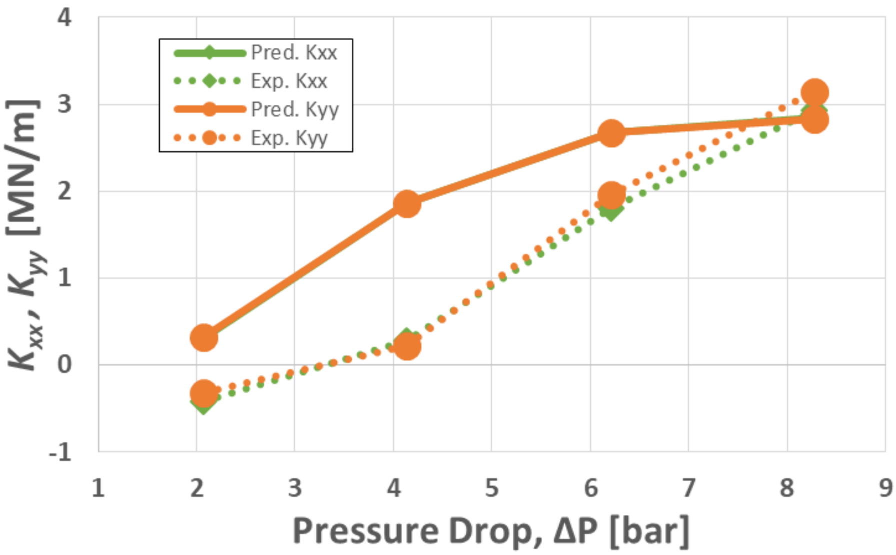

Figure 64. ***K_{xx}* and *K_{yy}* vs Δ*P* for *ϵ_0*= 0.00 and ω = 6 krpm for the zero pre-swirl insert.**

6.1b Cross-coupled Stiffness Coefficients

For the zero pre-swirl insert at ω = 2 krpm and Δ*P* = 8.27 bar, Fig. 65 shows representative relationships for the predicted and experimental results of K_{xy} and K_{yx} versus ϵ_0. When ϵ_0 = 0.00, the predicted K_{xy} and K_{yx} values closely approximate experimental results. As ϵ_0 increases, the predicted K_{yx} closely approximate the experimental results with the exception of ϵ_0 = 0.27. For K_{xy}, the predicted results follow the same trend as the experimental values while over-predicting most of the experimental values by ~50-75%. These relationships hold true for the medium, and high pre-swirl insert.

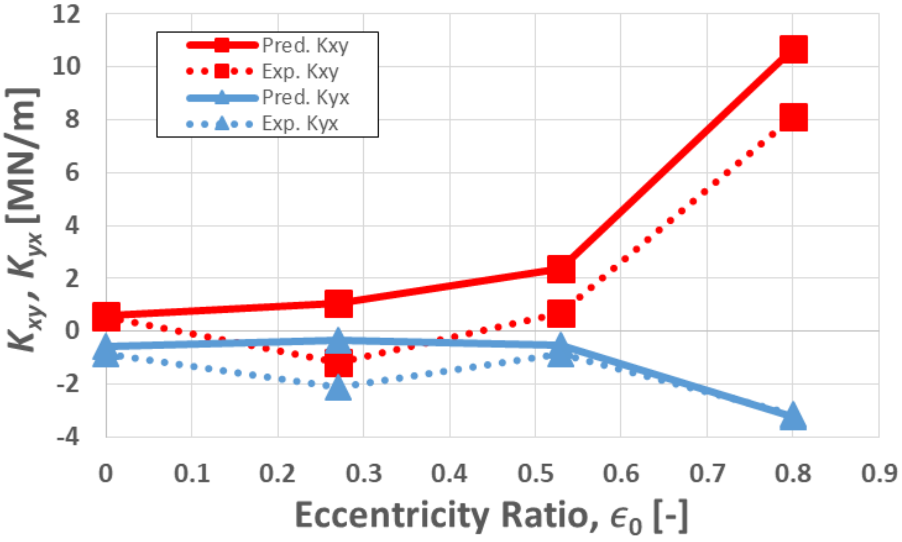

Figure 65. K_{xy} **and** K_{yx} **vs** ϵ_0 **for** ΔP **= 8.27 bar and ω = 2 krpm for the zero pre-swirl insert.**

Figure 66 shows the same data set as Fig. 65 for ω = 6 krpm. Overall for $\epsilon_0 \leq 0.53$, K_{xy} and K_{yx} predictions closely approximate the experimental results. Unlike Fig. 65 at ϵ_0 = 0.80, the K_{yx} predictions diverge from the experimental results and under-predict the magnitude of the experimental results by a factor of ~2.5.

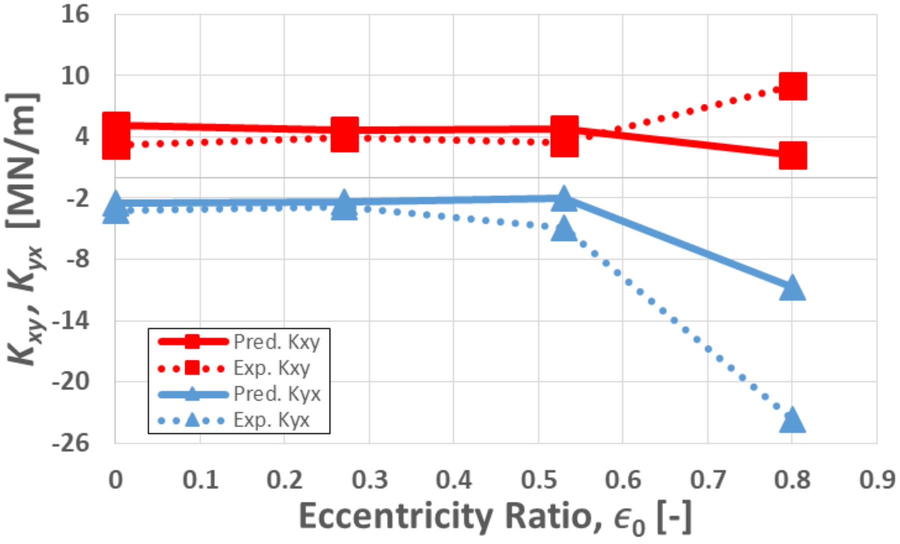

Figure 66. K_{xy} **and** K_{yx} **vs** ϵ_0 **for** ΔP **= 8.27 bar and ω = 6 krpm for the zero pre-swirl insert.**

For the zero pre-swirl insert at ω = 6 krpm and ϵ_0 = 0.00, Fig. 67 shows representative relationships for the predicted and experimental results of K_{xy} and K_{yx} versus ΔP. Predicted values of K_{xy} are underpredicted by ~10% except at $\Delta P = 6.21$ bar, where experimental values of K_{xy} are underpredicted by a factor of 2.5. Predicted values of K_{yx} exceed the experimental values by ~50-850%. There is a significant decrease in the experimental values of K_{yx} at $\Delta P >$ 6.21 bar. Note from the same data set given in Fig. 61 and Fig. 62, the transition between laminar and transitional is predicted to occur at $\Delta P = 4.13$ bar.

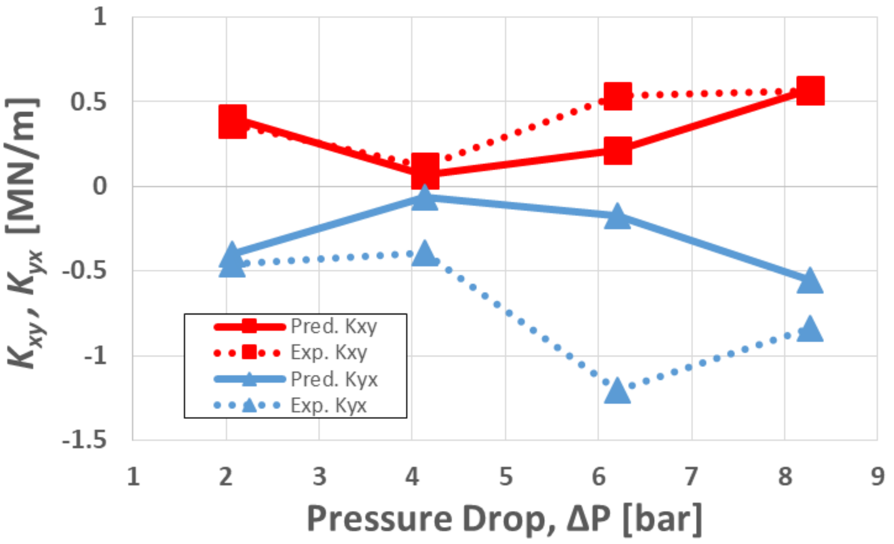

Figure 67. K_{xy} **and** K_{yx} **vs** ΔP **for** ϵ_0**= 0.00 and ω = 2 krpm for the zero pre-swirl insert.**

For the zero pre-swirl insert at ω = 2 krpm and ϵ_0 = 0.80, Fig. 68 shows representative relationships for the predicted and experimental results of K_{xy} and K_{yx} versus ΔP. The most accurate predictions of K_{yx} are at higher ΔP while the reverse is true for K_{xy}. As ϵ_0 increases, the experimental results more closely match the predicted results as compared to Fig. 67.

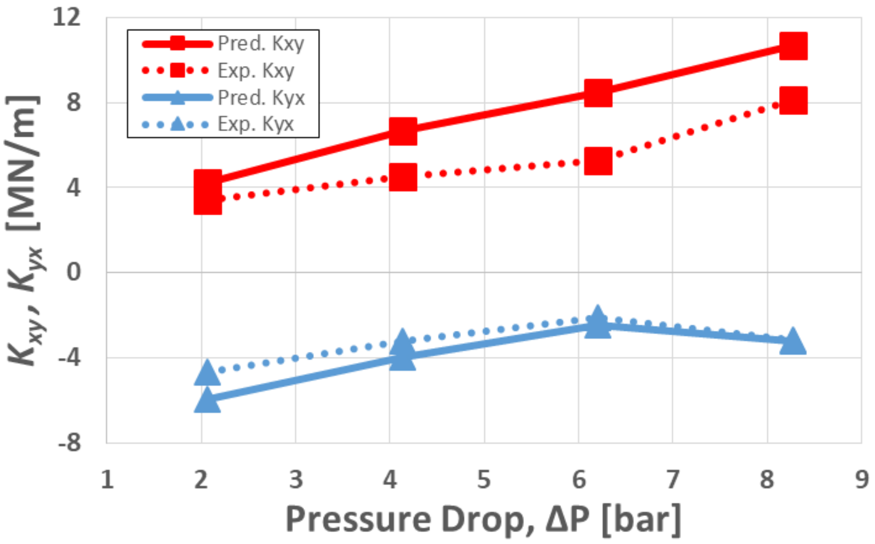

Figure 68. K_{xy} **and** K_{yx} **vs** ΔP **for** ϵ_0**= 0.80 and ω = 2 krpm for the zero pre-swirl insert.**

For the zero pre-swirl insert at ω = 6 krpm and ϵ_0 = 0.00, Fig. 69 shows representative relationships for the predicted and experimental results of K_{xy} and K_{yx} versus ΔP. The K_{xy} and K_{yx} values are ~1-3% overpredicted until ΔP > 6.21 bar at which point the experimental data is under-predicted by 40% and 100% for ΔP = 6.21 bar and ΔP = 8.27 bar respectively. It is important to note that the trends for both the experimental and predicted values for K_{xy} and K_{yx} are approximately equal in magnitude and opposite in sign.

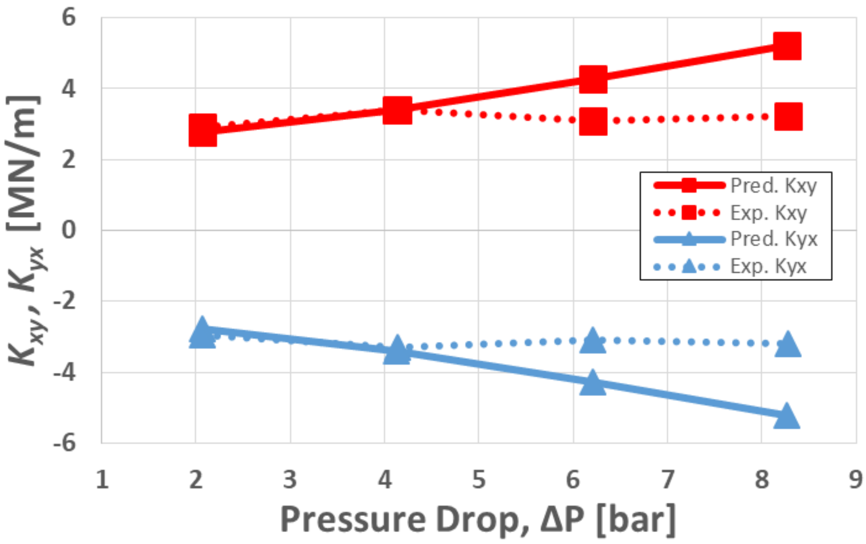

Figure 69. K_{xy} **and** K_{yx} **vs** ΔP **for** $\epsilon_0 = 0.00$ **and ω = 6 krpm for the zero pre-swirl insert.**

For the high pre-swirl insert at ω = 6 krpm and $\epsilon_0 = 0.00$, Fig. 70 shows representative relationships for the predicted and experimental results of K_{xy} and K_{yx} versus ΔP. Figure 70 shows that the predicted values of K_{xy} align closely with the experimental data similar to those shown in Fig. 69. Unlike the data shown in Fig. 69 for K_{yx}, those in Fig. 70 were under-predicted by ~100% across the entire range of measured ΔP. The relationships shown were also true for the medium and high pre-swirl inserts.

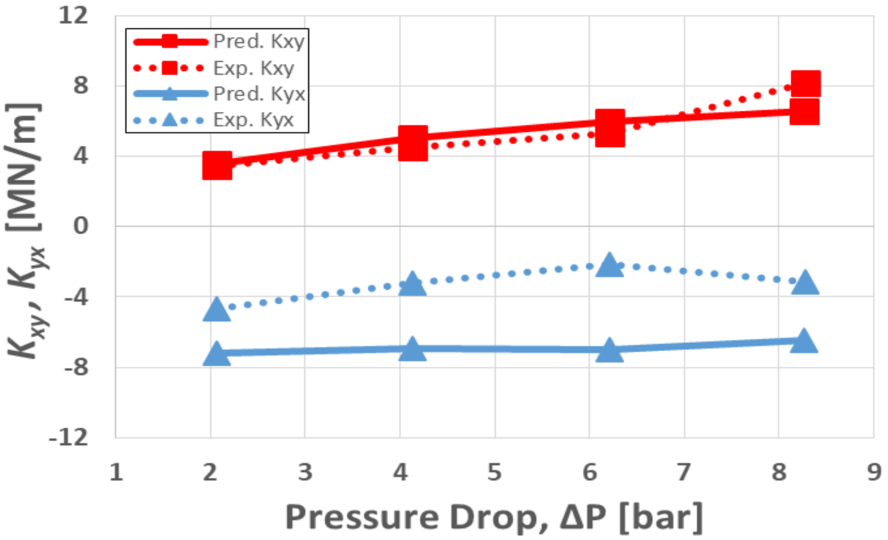

Figure 70. K_{xy} **and** K_{yx} **vs** ΔP **for** ϵ_0**= 0.00 and ω = 6 krpm for the high pre-swirl insert.**

6.2 Damping Coefficients

6.2a Direct Damping Coefficients

A large portion of the relationships between the experimental and predicted C_{xx} and C_{yy} can be represented by Fig. 71, which shows a representative relationship between C_{xx} and C_{yy} for the predicted and experimental results versus ϵ_0 for the zero pre-swirl insert at ω = 2 krpm and ΔP = 8.27 bar. At low values of ϵ_0, the predictions are larger than the experimental data by a factor of 1.15. When $\epsilon_0 > 0.53$, the predicted values are larger than the experimental results by 1.50 for both C_{xx} and C_{yy}.

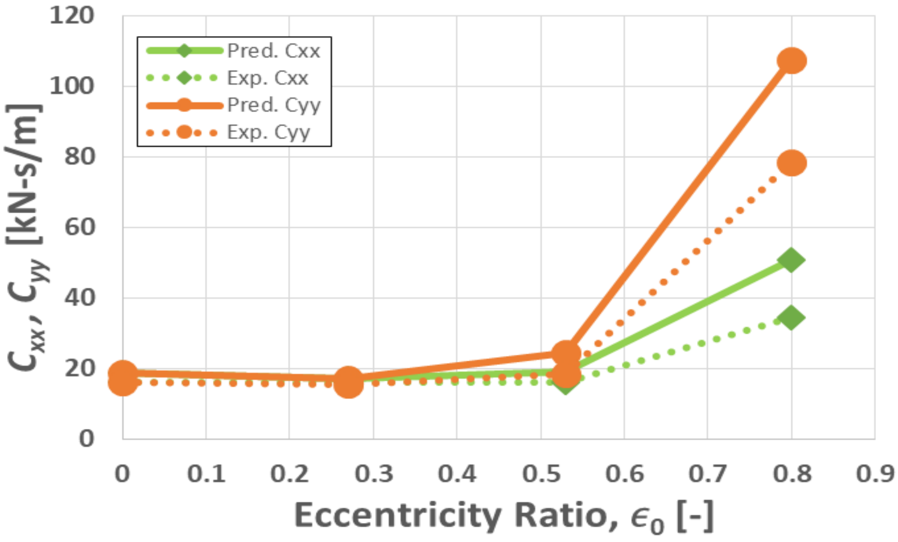

Figure 71. C_{xx} and C_{yy} vs ϵ_0 for ΔP = 8.27 bar and ω = 2 krpm for the zero pre-swirl insert.

For the zero pre-swirl insert at ω = 6 krpm and ΔP = 8.27 bar, Fig. 72 shows representative relationships for the predicted and experimental results of C_{xx} and C_{yy} versus ϵ_0. C_{xx} and C_{yy} predictions more closely match the experimental results for low values of ϵ_0. At ϵ_0 = 0.80, the predictions are larger than the experimental results by ~10% compared to the ~50% from Fig. 71. The relationships shown hold for the medium and high pre-swirl inserts.

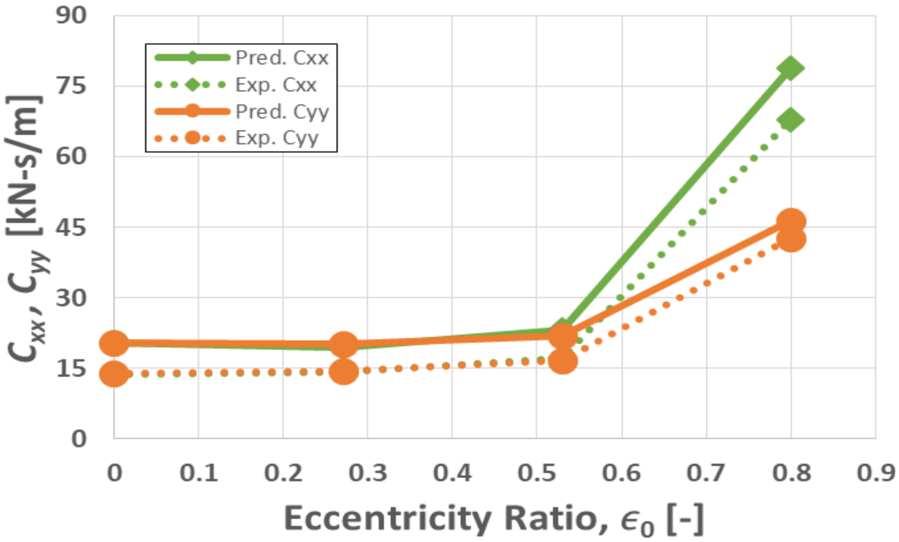

Figure 72. C_{xx} **and** C_{yy} **vs** ϵ_0 **for** $\Delta P = 8.27$ **bar and ω = 6 krpm for the zero pre-swirl insert.**

For the zero pre-swirl insert at ω = 2 krpm and $\epsilon_0 = 0.00$, Fig. 73 shows representative relationships for the predicted and experimental results of C_{xx} and C_{yy} versus ΔP. The C_{xx} and C_{yy} predictions are smaller than the experimental values by ~10% except for $\Delta P > 6.21$ bar where the predictions over-predict the experimental results by ~10%.

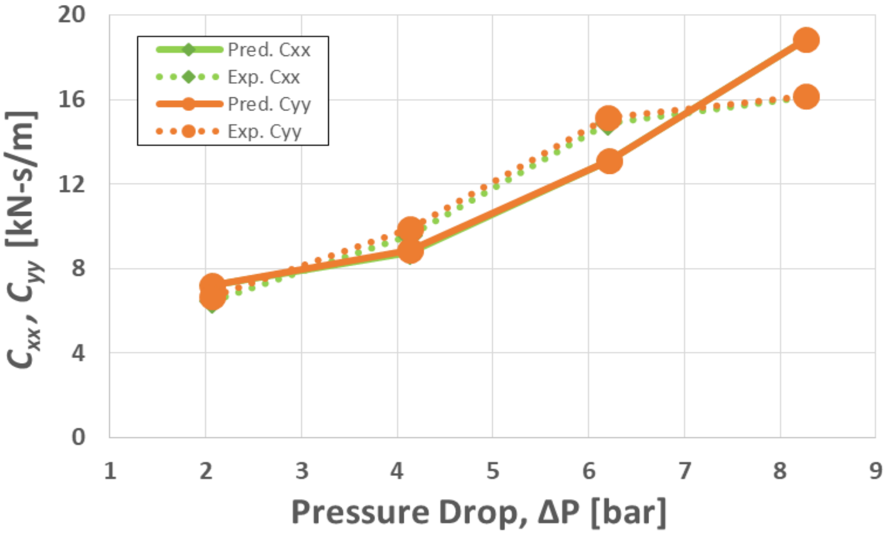

Figure 73. C_{xx} and C_{yy} vs ΔP for ϵ_0 = 0.00 and ω = 2 krpm for the zero pre-swirl insert.

For the high pre-swirl insert at ω = 2 krpm and ϵ_0 = 0.80, Fig. 74 shows representative relationships for the predicted and experimental results of C_{xx} and C_{yy} versus ΔP. The values of C_{yy} and C_{xx} are over-predicted by ~50%.

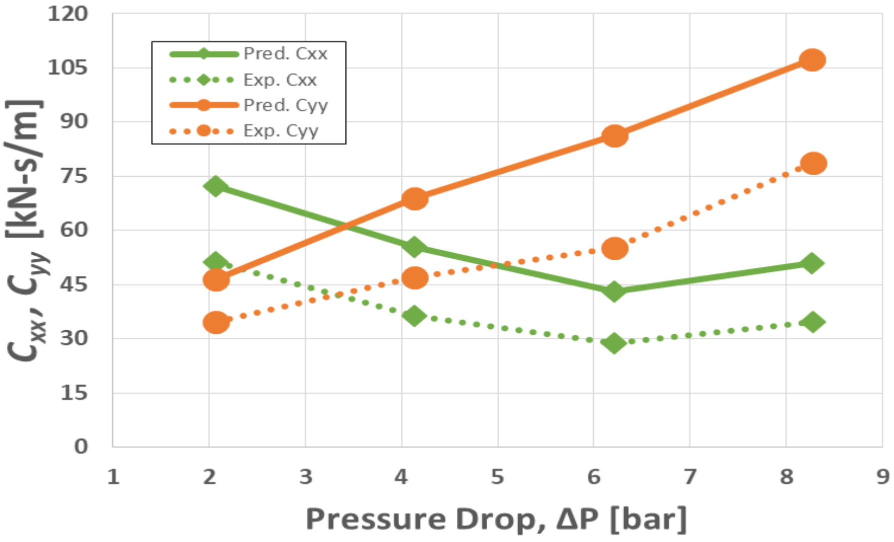

Figure 74. C_{xx} and C_{yy} vs ΔP for ϵ_0 = 0.80 and ω = 2 krpm for the zero pre-swirl insert.

For the high pre-swirl insert at ω = 6 krpm and ϵ_0 = 0.00, Fig. 75 shows representative relationships for the predicted and experimental results of C_{xx} and C_{yy} versus ΔP. As ω increases, the experimental results diverge from the predicted results. The direct damping results were over predicted by ~50-100%. As ΔP increases beyond 4.27 bar, the predictions and experimental results start to diverge.

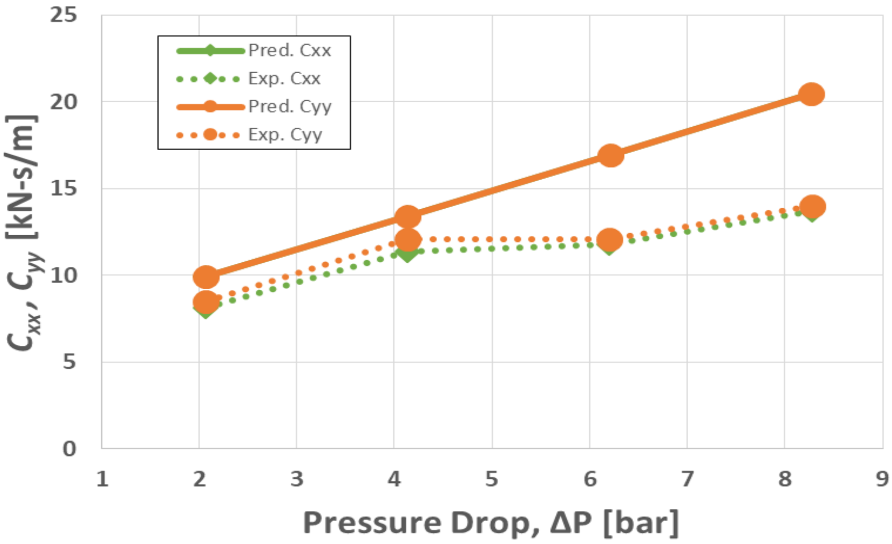

Figure 75. C_{xx} **and** C_{yy} **vs** ΔP **for** ϵ_0 **= 0.00 and ω = 6 krpm for the zero pre-swirl insert.**

For the high pre-swirl insert at ω = 2 krpm and ϵ_0 = 0.80, Fig. 76 shows representative relationships for the predicted and experimental results of C_{xx} and C_{yy} versus ΔP. Contrary to the zero pre-swirl insert data shown in Fig. 74, the C_{xx} and C_{yy} predictions show the opposite trend in Fig. 76. The experimental results for C_{yy} are closely approximated by the predicted results contrary to Fig. 74, where C_{yy} is over-predicted by a factor of ~3-4.

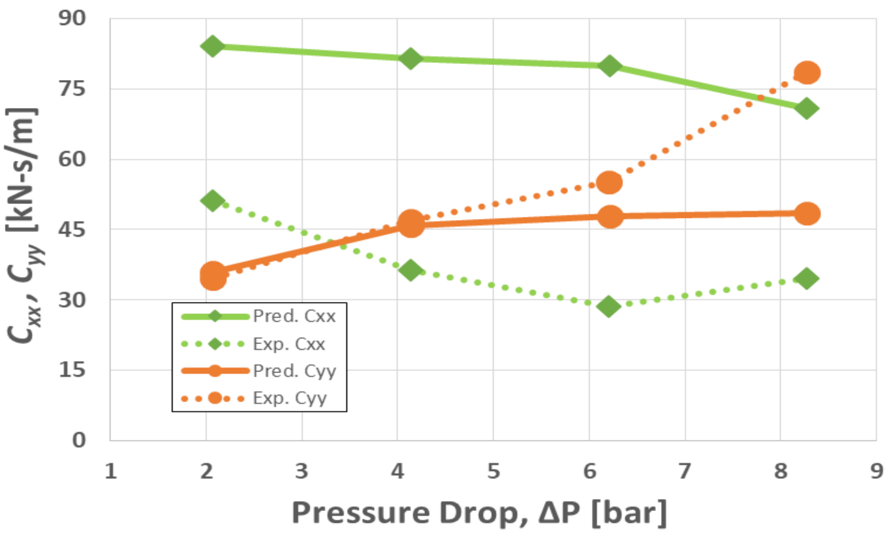

Figure 76. C_{xx} **and** C_{yy} **vs** ΔP **for** $\epsilon_0 = 0.80$ **and ω = 2 krpm for the high pre-swirl insert.**

6.2b Cross-coupled Damping Coefficients

For the zero pre-swirl insert at ω = 2 krpm and ΔP = 8.27 bar, Fig. 77 shows representative relationships for the predicted and experimental results of C_{yx} and C_{xy} versus ϵ_0. Note that for $\epsilon_0 < 0.53$, C_{yx} and C_{xy} have opposite signs and are gyroscopic (do not dissipate energy). When $\epsilon_0 > 0.53$ C_{yx} and C_{xy} decrease significantly and have the same sign (do dissipate energy). At low values of ϵ_0, the C_{yx} and C_{xy} predictions over-predict the experimental data by ~15%, and when $\epsilon_0 < 0.53$ the predictions are off by ~10% and for $\epsilon_0 > 0.53$, the predictions over-predict by a factor of ~1.75.

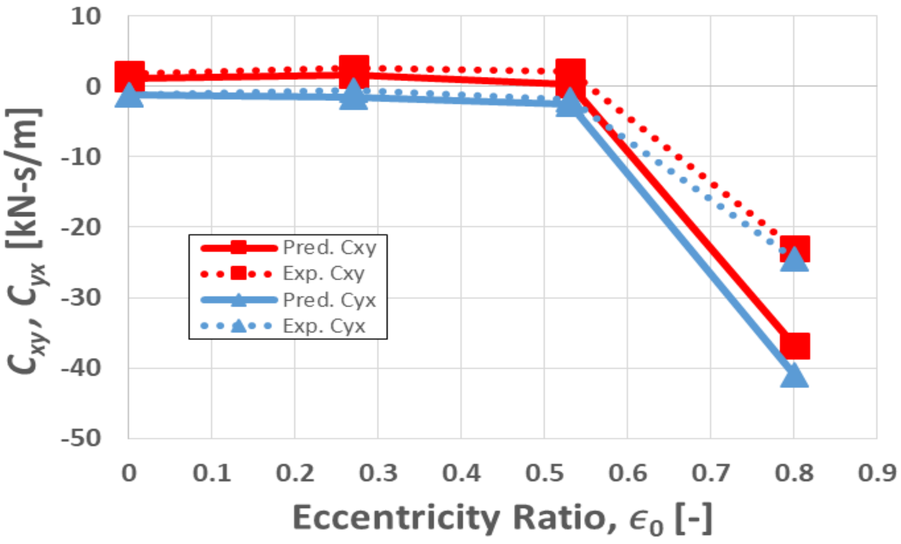

Figure 77. C_{xy} **and** C_{yx} **vs** ϵ_0 **for** ΔP **= 8.27 bar and ω = 2 krpm for the zero pre-swirl insert.**

For the zero pre-swirl insert at ω = 6 krpm and ΔP = 8.27 bar, Fig. 78 shows representative relationships for the predicted and experimental results of C_{yx} and C_{xy} versus ϵ_0. For $\epsilon_0 < 0.53$, the predictions are ~10% under the experimental values. When $\epsilon_0 > 0.53$, the predictions under-predict the experimental values by 30% for C_{yx}, and ~75% for C_{xy}. The relationships shown in Fig. 78 were also true for the medium and high pre-swirl inserts.

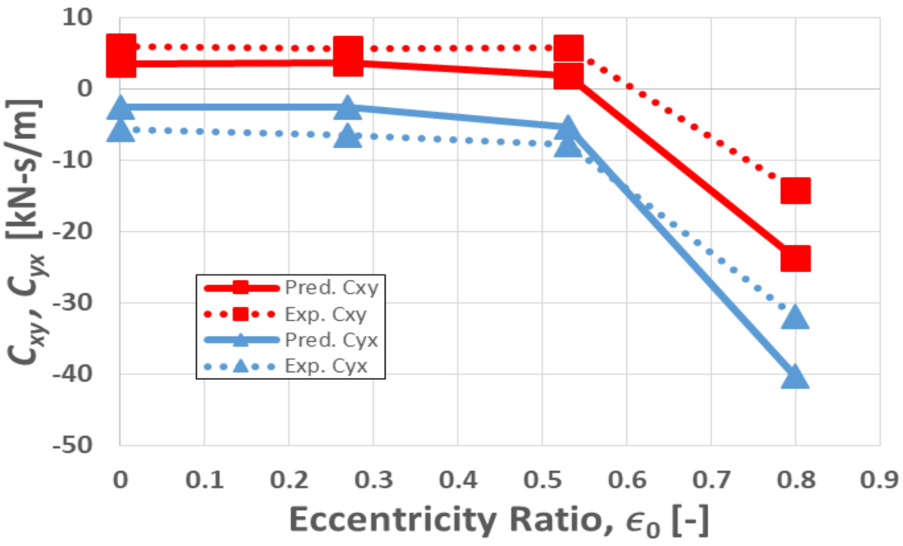

Figure 78. C_{xy} **and** C_{yx} **vs** ϵ_0 **for** ΔP **= 8.27 bar and ω = 6 krpm for the zero pre-swirl insert.**

For the zero pre-swirl insert at ω = 2 krpm and $\epsilon_0 = 0.00$, Fig. 79 shows representative relationships for the predicted and experimental results of C_{yx} and C_{xy} versus ΔP. The C_{yx} and C_{xy} predictions closely approximate the experimental values. For higher values of ω, and $\epsilon_0 =$ 0.00, the same general trend holds.

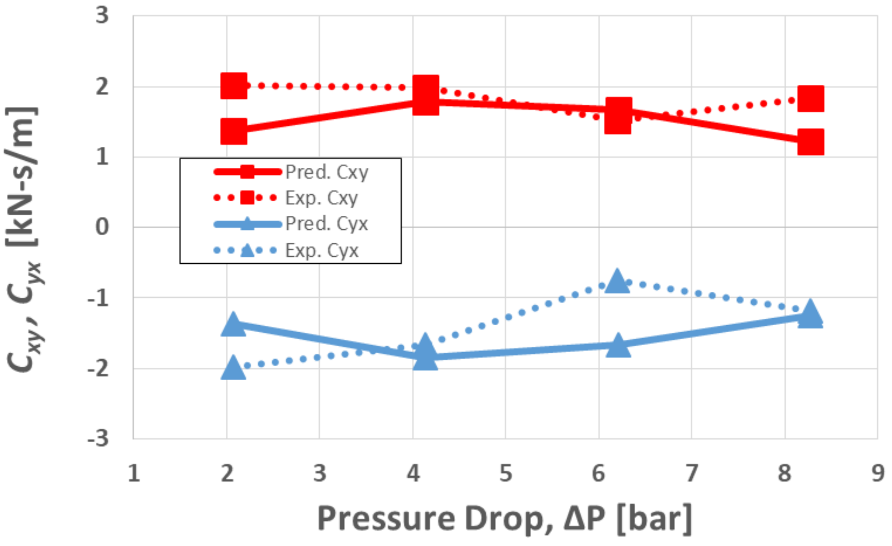

Figure 79. C_{xy} **and** C_{yx} **vs** ΔP **for** $\epsilon_0 = 0.00$ **and ω = 2 krpm for the zero pre-swirl insert.**

For the zero pre-swirl insert at ω = 2 krpm and ϵ_0 = 0.80, Fig. 80 shows representative relationships for the predicted and experimental results between C_{yx} and C_{xy} versus ΔP. The C_{yx} and C_{xy} predictions under-predict the experimental values by ~100%. Comparing Fig. 79 and Fig. 80 note that as ϵ_0 increases to 0.80, the predictions and the experimental results diverge. This trend was true for the medium and high pre-swirl inserts. Note that in Fig. 79 C_{yx} and C_{xy} have opposite signs (gyroscopic damping), whereas C_{yx} and C_{xy} are both negative (dissipative damping) in Fig. 80.

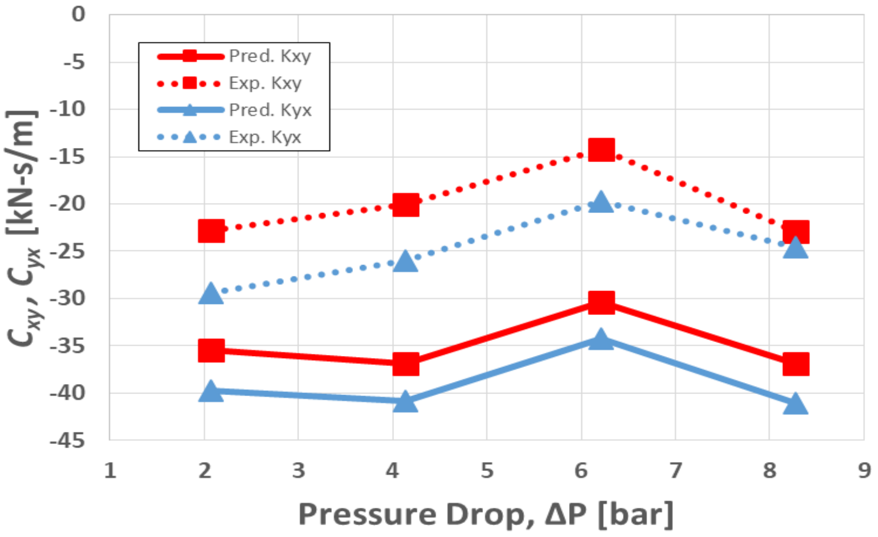

Figure 80. C_{xy} **and** C_{yx} **vs** ΔP **for** ϵ_0 **= 0.80 and ω = 2 krpm for the zero pre-swirl insert.**

6.3 Virtual Mass Coefficients

6.3a Direct Virtual Mass Coefficients

For the zero pre-swirl insert at ω = 2 krpm and ΔP = 8.27 bar, Fig. 81 shows representative relationships for the predicted and experimental results of M_{xx} and M_{yy} versus ϵ_0. The relative difference between the M_{xx} and M_{yy} predictions and the experimental results is

~50% until ϵ_0 > 0.80. At ϵ_0 = 0.80, the difference between the predictions and the experimental results for M_{xx} remains ~50%, but M_{yy} is under-predicted by a factor of ~3.5. This large difference is also seen for both the medium and high pre-swirl inserts for low speeds. At the time of writing, the author is unsure of the reason for the large difference between the predicted and experimental results at ϵ_0 = 0.8 for M_{yy}.

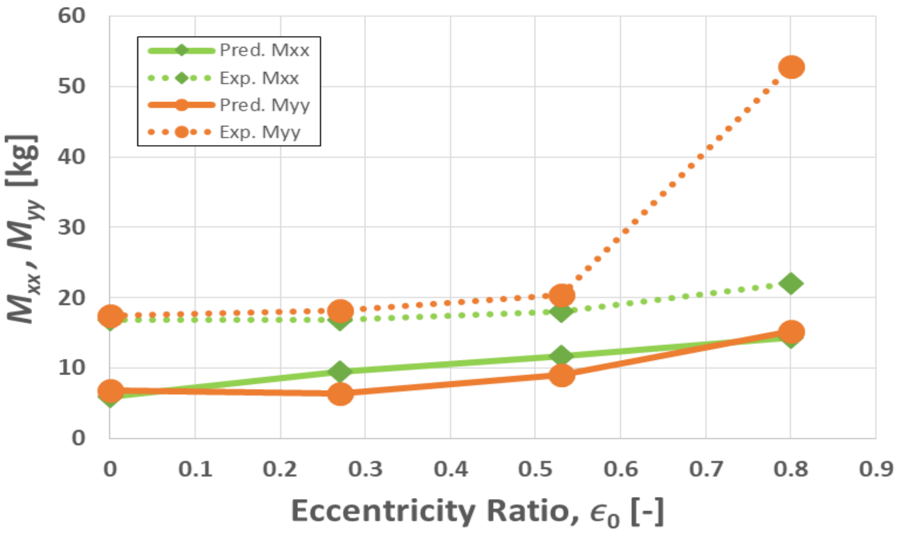

Figure 81. M_{xx} **and** M_{yy} **vs** ϵ_0 **for** ΔP **= 8.27 bar and ω = 2 krpm for the zero pre-swirl insert.**

For the high pre-swirl insert at ω = 6 krpm and ϵ_0= 0.00, Fig. 82 shows representative relationships for the predicted and experimental results of M_{xx} and M_{yy} versus ΔP. The predicted values of M_{xx} and M_{yy} under-predict the experimental values by by a factor of ~2-3.

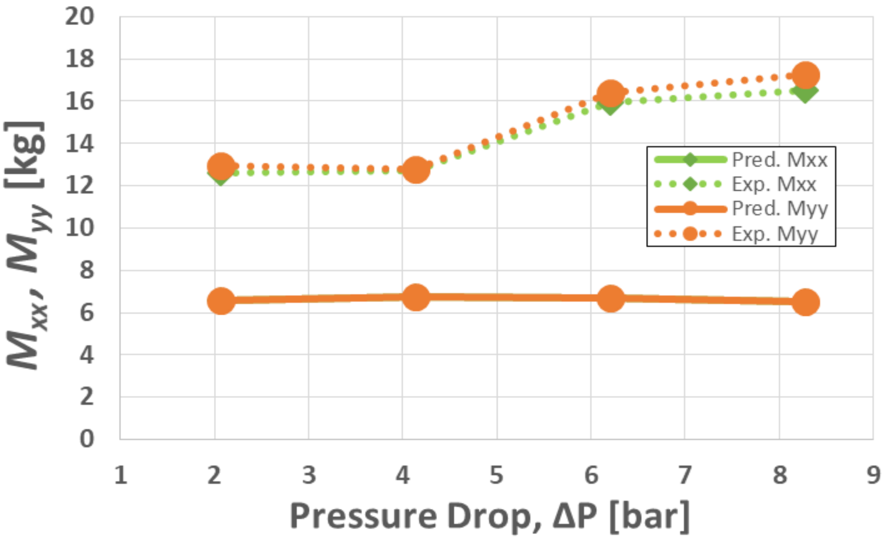

Figure 82. M_{xx} **and** M_{yy} **vs** ΔP **for** ϵ_0 **= 0.00 and ω = 6 krpm for the high pre-swirl insert.**

6.3b Cross-coupled Virtual Mass Coefficients

For the high pre-swirl insert at ω = 2 krpm and ΔP = 8.27 bar, Fig. 83 shows representative relationships for the predicted and experimental results of M_{xy} and M_{yx} versus ϵ_0. Similar to Fig. 81, up until ϵ_0 = 0.8, the predicted results were ~10% off of the experimental results. At ϵ_0 = 0.8, the difference between the predictions and the experimental results for M_{xy} is relatively small but M_{yx} is under-predicted by a factor of ~3.5. This large difference is seen for both the zero, medium and high pre-swirl inserts for all measured speeds. At the time of writing, the author is unsure of the reason for the large difference between the predicted and experimental results at ϵ_0 = 0.8 for M_{yy}.

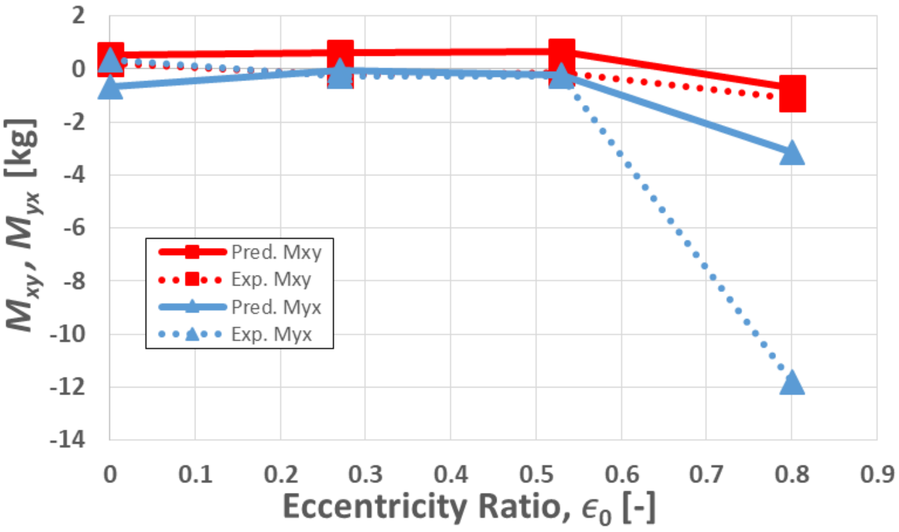

Figure 83. M_{xy} **and** M_{yx} **vs** ϵ_0 **for** ΔP **= 8.27 bar and ω = 2 krpm for the high pre-swirl insert.**

For the zero pre-swirl insert at ω = 2 krpm and ϵ_0= 0.00, Fig. 84 shows representative relationships for the predicted and experimental results of M_{xy} and M_{yx} versus ΔP. The magnitude of the experimental values for M_{xy} are under-predicted by ~50%, while the magnitude of the experimental values for M_{yx} are over-predicted by ~100%. However, the signs of the predictions and the experimental results for M_{xy} and M_{yx} are opposite, i.e. the predicted values indicated that the seal should have been destabilizing, but the experimental results showed that the seal was actually stabilizing.

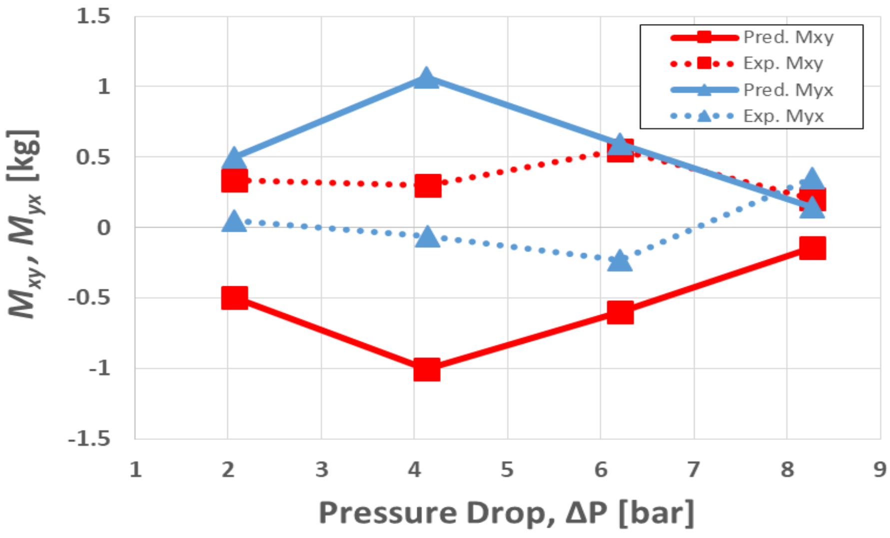

Figure 84. M_{xy} **and** M_{yx} **vs** ΔP **for** ϵ_0 **= 0.00 and ω = 2 krpm for the zero pre-swirl insert.**

6.4 Whirl Frequency Ratio

For the zero pre-swirl insert at ΔP = 4.13 bar, Fig. 85 shows representative relationships for the predicted and experimental results of f_w versus ϵ_0. Recall when comparing liquid annular seals, a lower f_w indicates a more stable seal. For the zero pre-swirl insert, as ϵ_0 increases both the experimental and predicted values of whirl frequency converge to ~0.4–0.5. The f_w predictions under-predict the experimental values by ~50-100%. Hence the seal is less stable than predicted. In general for the zero pre-swirl insert, the operating conditions where the seal is most stable are ϵ_0= 0.00 and ω = 2 krpm.

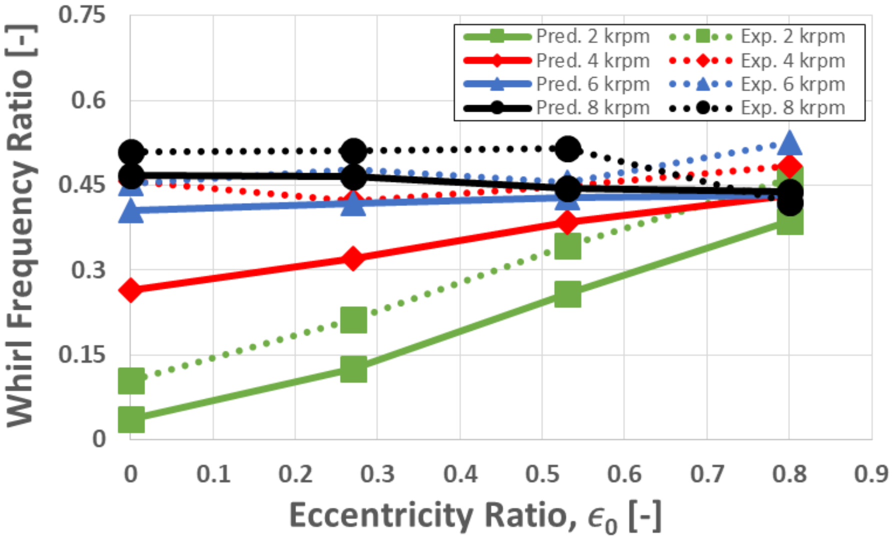

Figure 85. f_w vs. ϵ_0 for the zero pre-swirl insert at ΔP = 4.13 bar.

For the high pre-swirl insert at ΔP = 4.13 bar, Fig. 86 shows representative relationships for the predicted and experimental results of f_w versus ϵ_0. Note that for the high pre-swirl insert, the most stable operating conditions for the seal are when ω = 8 krpm, because of the dominating effect on pre-swirl the insert has at low speeds. Unlike the data presented for the zero pre-swirl insert in Fig. 85 there is no clear trend between f_w and ϵ_0. In general for the high pre-swirl insert, the f_w predictions under-predict the experimental values by ~50-100%. Hence the seal is less stable than predicted.

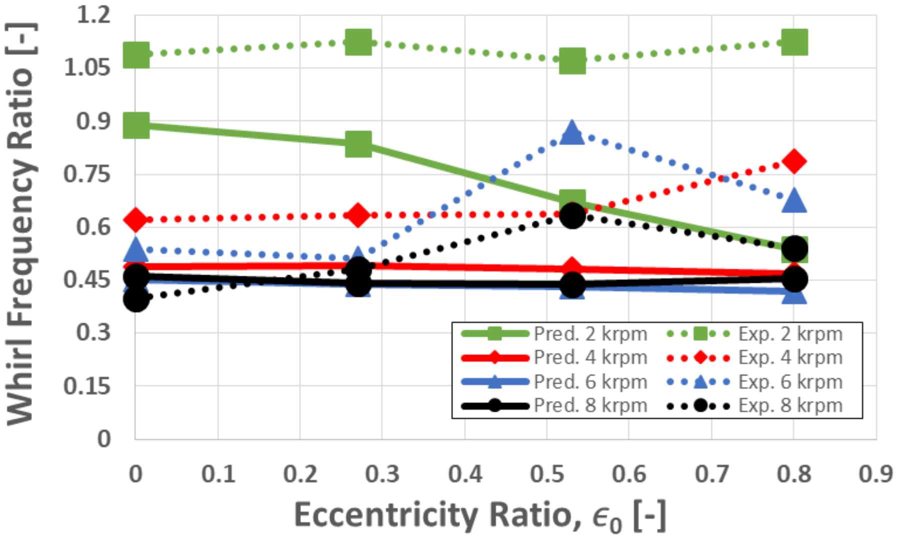

Figure 86. f_w **vs.** ϵ_0 **for the high pre-swirl insert at** ΔP **= 4.13 bar.**

For the zero pre-swirl insert at ΔP = 8.27 bar, Fig. 87 shows representative relationships for the predicted and experimental results of f_w versus ϵ_0. Comparing the data presented in Fig. 85 for ΔP = 4.13 bar and the data presented in Fig. 87, we can see that in general lower values of ϵ_0 and ω are the most stable operating conditions. Note that for ΔP = 8.27 bar, the f_w predictions over-predict the experimental values by ~10-100%. For the zero pre-swirl insert, the operating conditions where the seal is most stable are ϵ_0= 0.27 and ω = 2 krpm. Hence the seal is generally more stable than predicted.

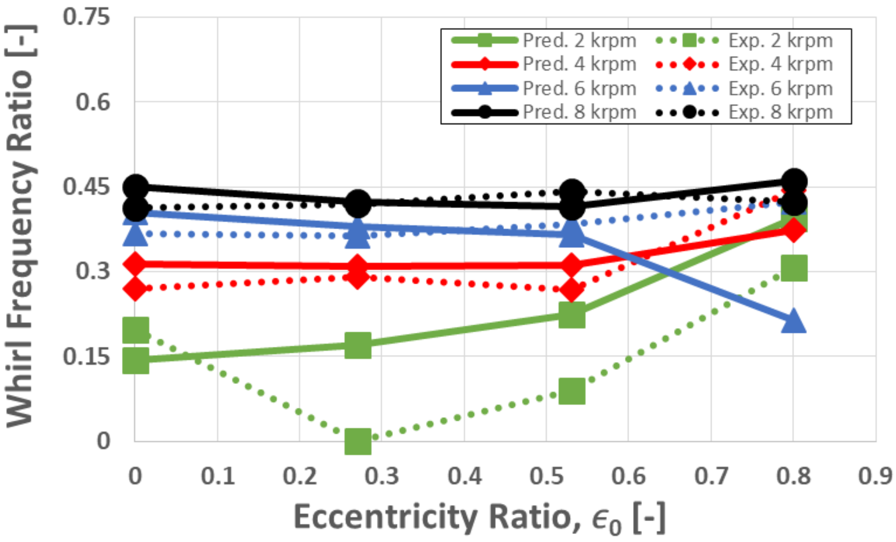

Figure 87. f_w **vs.** ϵ_0 **for the zero pre-swirl insert at** ΔP **= 8.27 bar.**

For the zero pre-swirl insert at ϵ_0= 0.00, Fig. 88 shows representative relationships for the predicted and experimental results of f_w versus ΔP. In general, the f_w predictions under-predict the experimental values by ~10-100%. As ω increases, f_w increases and is therefore less stable. Relative to the effect of ω on f_w, ΔP has relatively little effect on f_w for the zero, medium, and high pre-swirl inserts. Hence the seal is less stable than predicted.

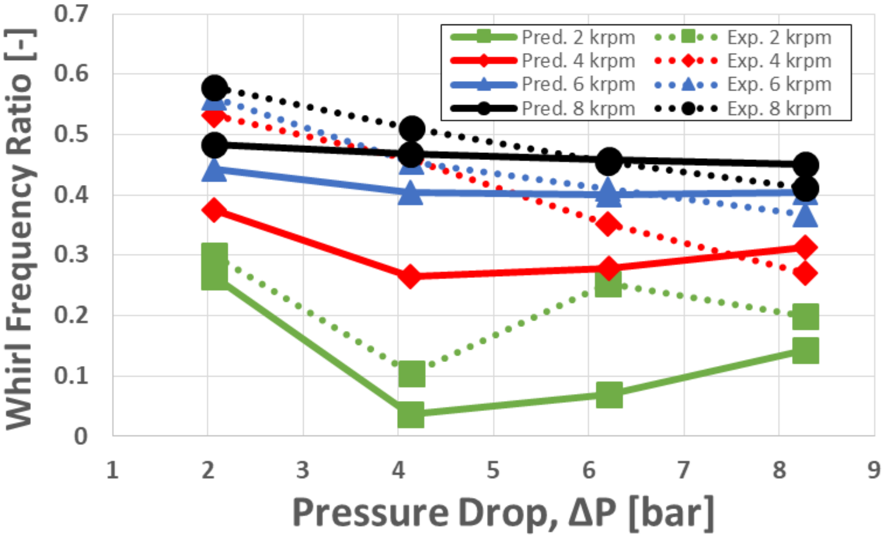

Figure 88. f_w vs. ΔP for the zero pre-swirl insert at ϵ_0 = 0.00.

For the zero pre-swirl insert at ϵ_0= 0.80, Fig. 89 shows representative relationships for the predicted and experimental results of f_w versus ΔP. When ϵ_0 = 0.80, the relationships between f_w and ΔP seen in Fig. 88 are no longer discernable. Note: for clarity, the experimental results for 6 krpm are hidden behind the trends, but it matches the predicted results within 5% when ΔP = [2.07, 4.13] bar and larger by a factor of ~2 when ΔP = [6.21, 8.27] bar.

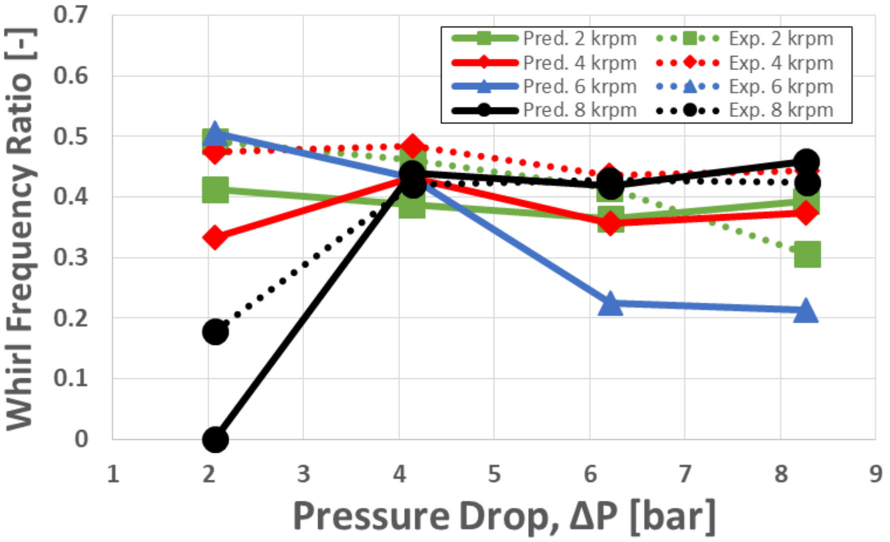

Figure 89. f_w vs. ΔP for the zero pre-swirl insert at $\epsilon_0 = 0.80$.

6.5 Effective Damping

Recalling the discussion from Section 5.6, Fig. 90 shows the experimental and predicted C_{eff} values vs. ΔP for the zero and high pre-swirl insert. The experimental data shown in Fig. 90 is from the same set of data shown in Fig. 56. The predictions consistently over-predict the stability of the seals by as much as a factor of 2. In general, the predictions are more accurate at low ω, and low ΔP. There is not a significant difference in the accuracy of the predicted values of C_{eff} between the zero, medium, and high pre-swirl insert.

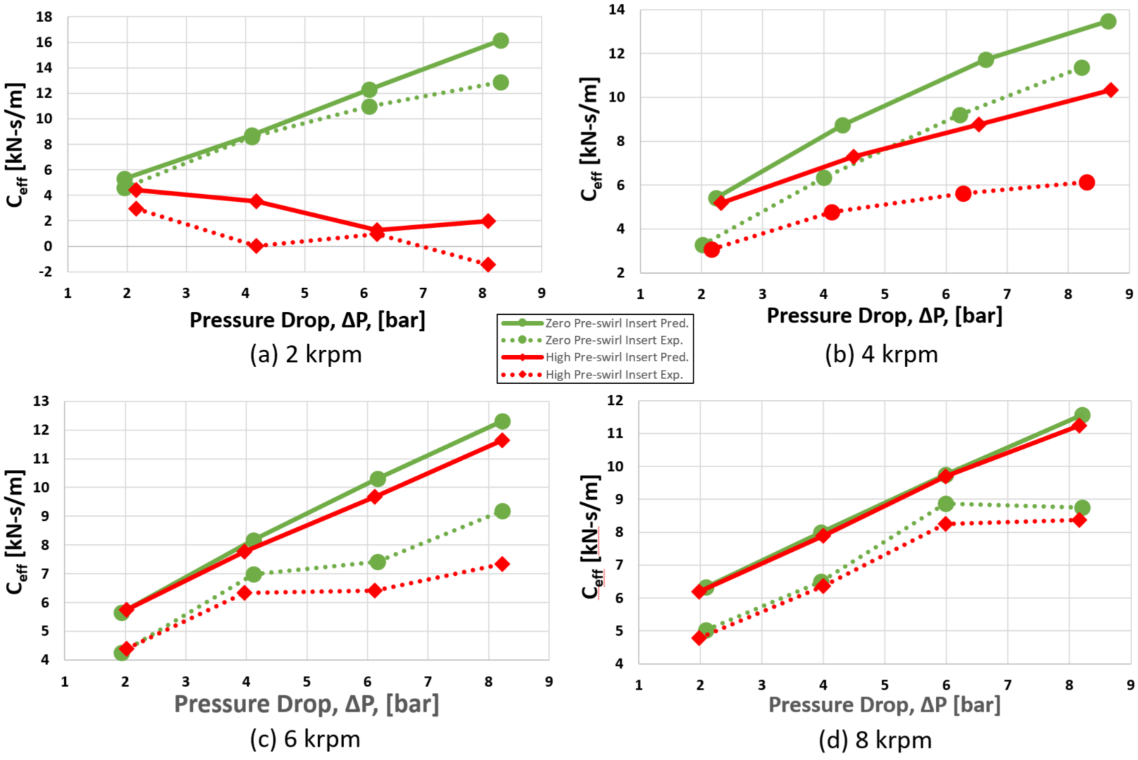

(a) 2 krpm

(b) 4 krpm

(c) 6 krpm

(d) 8 krpm

Figure 90. Measured and predicted C_{eff} vs. ΔP for (a) 2, (b) 4, (c) 6, and (d) 8 krpm.

Figure 91 shows the experimental and predicted C_{eff} values vs. ω for the zero and high pre-swirl insert. The predictions over-predict the experimental values by up to a factor of 2, hence the seal is less stable than predicted. There is not a significant difference in the accuracy of the predicted values of C_{eff} between the zero, medium, and high pre-swirl insert. Note that the predictions follow the same trends as the experimental values.

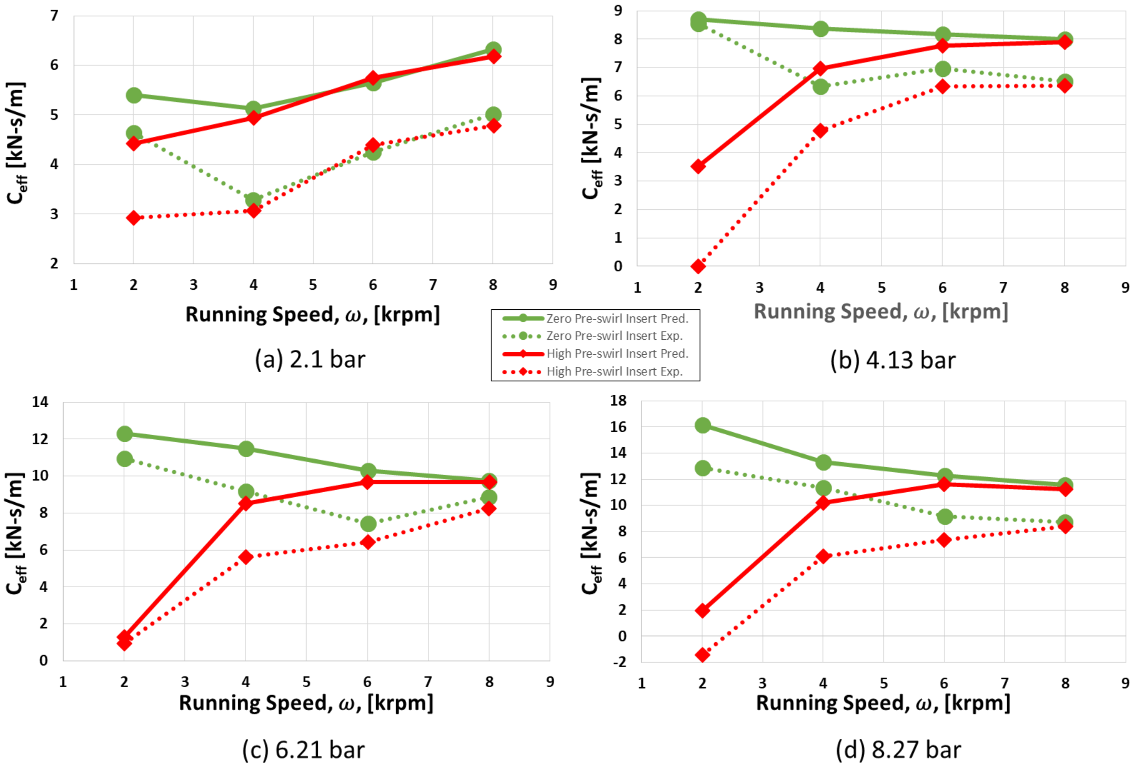

(a) 2.1 bar

(b) 4.13 bar

(c) 6.21 bar

(d) 8.27 bar

Figure 91. Measured and predicted C_{eff} vs. ω for Δ*P* = (a) 2.1, (b) 4.13, (c) 6.21, and (d) 8.27 bar.

Figure 92 shows the experimental and predicted C_{eff} values vs. PSR for the zero and high pre-swirl insert. The predictions over-predict the seal by up to a factor of 2, hence the seal is less stable than predicted. There is not a significant difference in the accuracy of the predicted values of C_{eff} between the zero, medium, and high pre-swirl insert. Note that the predictions follow the same trends as the experimental values.

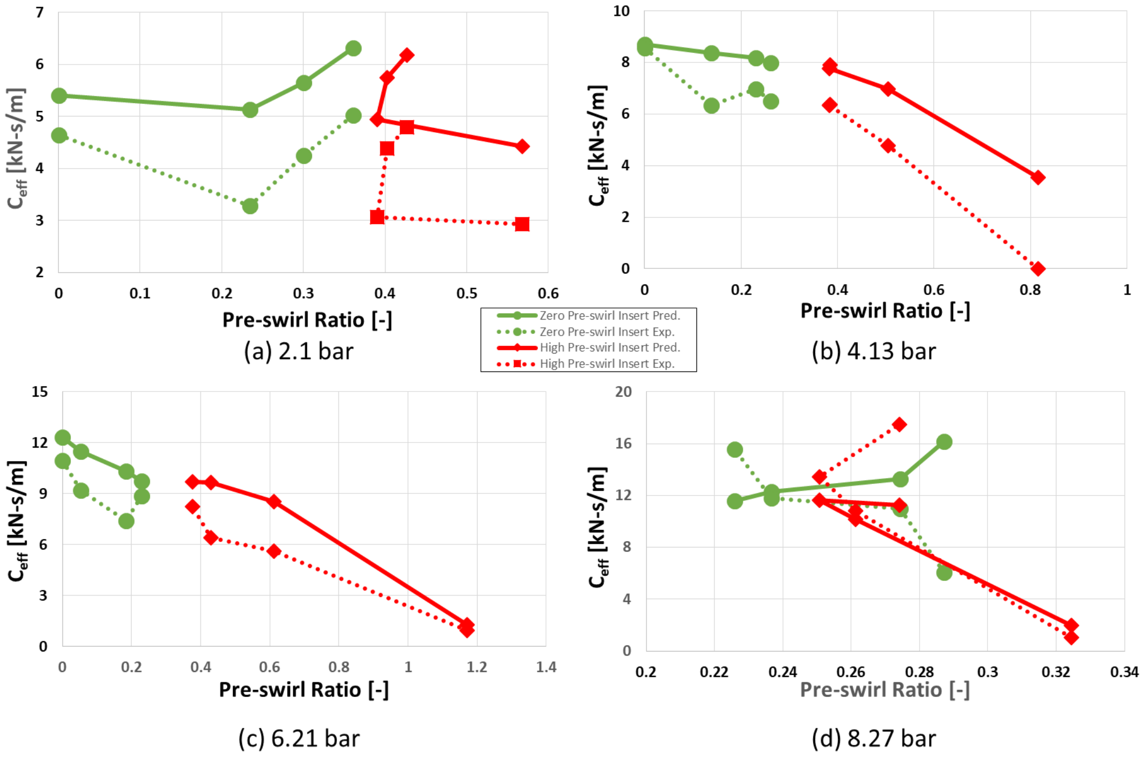

Figure 92. Measured and predicted C_{eff} vs. PSR for ΔP = (a) 2.1, (b) 4.13, (c) 6.21, and (d) 8.27 bar.

7. SUMMARY AND CONCLUSIONS

Tests were conducted for the static and rotordynamic characteristics of plain annular seals. The set of plain annular seals tested had: length of 50.800 mm (2.00 inches), diameter of 102.0064 mm (4.016 inches), and radial clearance of 0.2032 mm (0.008 inches). The tests were conducted by varying the following parameters: running speeds, ω = 2, 4, 6, 8 kprm, axial pressure drops, $\varDelta P$ = 2.1, 4.13, 6.21, and 8.27 bar (30, 60, 90, and 120 psi), eccentricity ratios, $\epsilon_0 =$ 0.00, 0.27, 0.53, and 0.80, and three pre-swirl inserts to target zero, medium, and high (0.0, 0.4, and 0.8) pre-swirl ratios, PSRs, for a set of specified operating conditions. The lubricant used was ISO VG 2 oil at 46.1°C (115°F).

7.1 Static Results

The static performance measurements included volumetric flow rate, $\dot{Q}$, PSR, and outlet swirl ratio, OSR. $\dot{Q}$ is a strong function of ΔP and is relatively immune to changes in ω or ϵ_0. It was reduced on average 10% or 6.5 LPM with the high pre-swirl insert as compared to the zero pre-swirl insert. (Note: ΔP is based on a pressure measurement upstream of the pre-swirl insert and downstream of the seal. Hence ΔP includes the pressure drop of the pre-swirl insert.) The representative plots for $\dot{Q}$ show that the XLAnSeal leakage predictions [16] match the measured $\dot{Q}$ results for low ω and radial injection. At low ω, the measured leakage is within 5% of the predicted values. As ω and imposed pre-swirl were increased, the predicted leakage values were greater than the measured leakage values on average by a factor of ~1.5, particularly for low ϵ_0.

The vector average Reynolds number, *Re*, was predicted to range over the transitional and turbulent regimes, while the experimental results showed the flow was mostly transitional with occasional test points in the laminar and turbulent regimes. *Re* was relatively unaffected by increases in ϵ_0 or imposed pre-swirl. When ΔP is increased from 2.13 bar to 8.27 bar for low ω, the vector Reynolds number increased by a factor of 3 from ~1250 to 3100. When ω increased from 2 krpm to 8 krpm, the total Reynolds number increased from ~1400-3500 or a factor of 2.5. At low ϵ_0, the predictions are smaller than the experimental results by a factor of ~2. As ϵ_0 increases, the predictions are smaller than the experimental results by as little as 5%.

Regarding PSR, as ω increased, PSR at the inlet to the seal tended to converge to a value of ~0.4-0.5 for all pre-swirl inserts. This result implies that, for lower ω, the inlet swirl velocity will be more important; i.e., since most ESPs run between 1.2-3.6 krpm, the seals will be heavily impacted by the inlet pre-swirl. An unexpected result was the lack of correlation between PSR and OSR. This was most probably due to the sudden radial expansion of the fluid at the outlet of the seal and the axial distance between the seal exit and the pitot tube measurement. The measured OSR values could be useful in validating CFD studies of annular liquid seals.

When “in the centered position", for low ΔP, and high ω, the seals experienced strong decentering forces, forcing the rotor to $\epsilon_0 =$ ~0.05-0.10. As ω increased, the seal decentering reaction force decreased, and the seal operated closer to $\epsilon_0 = 0.00$.

7.2 Rotordynamic Measurements

The seals direct stiffness coefficients, K_{xx} and K_{yy} were relatively unaffected by changes in the pre-swirl insert, and changes in ϵ_0 over the range [0.00, 0.53]. For all tested ΔP, ω, and imposed PSR, the measured values of K_{yy} for ϵ_0 = 0.80 were larger than measured K_{yy} by a factor of ~1.5-2 for ϵ_0 = 0.00. When ΔP increased from 2.13 bar to 8.27 bar for the zero pre-swirl insert, the direct stiffness increases by a factor of ~2.5 for ω $\geq$ 6 krpm, and $\epsilon_0 \leq 0.53$. At low values of ΔP and ω > 2 krpm, K_{xx} and K_{yy} were generally negative; i.e., a pump supported by these seals would have both a reduced natural frequency and a lowered onset speed of instability at these operating points. Additionally, for operating conditions where the Reynolds number traverses ~2000-2300 or the mid-transitional regime, the direct stiffness experienced a marked decrease in magnitude.

Regarding the cross-coupled stiffness coefficients for $\epsilon_0 \in [0.00, 0.53]$, $K_{xy} \cong -K_{yx}$. For $\epsilon_0 = 0.80$, K_{yx} increased 1.25 times in magnitude when compared to the measured values at $\epsilon_0 = 0.00$, and K_{xy} is relatively constant for any changes in ϵ_0, and ΔP. Therefore an increase in $|K_{yx}|$ increases $|K_{xy} - K_{yx}|$, indicating that the seal will be more destabilizing at $\epsilon_0 > 0.5$. In general, as the PSR increased from ~0.1 to ~0.45 with the different pre-swirl inserts, $|K_{xy} - K_{yx}|$ increased by a factor of 2.5, indicating that when higher PSRs are experienced by the seal, the seal will be more destabilizing.

The seals direct damping coefficients, C_{xx} and C_{yy}, increased with increasing ΔP and ω, but were relatively unaffected by changes in $\epsilon_0 \in [0.00, 0.53]$. For $\epsilon_0 < 0.53$, $C_{xx} \cong C_{yy}$. When $\epsilon_0 = 0.80$, C_{xx} and C_{yy} experience a large increase in magnitude. Interestingly, C_{xx} increases with increasing ω, while C_{yy} decreases with increasing ω. For the zero pre-swirl insert, for all ϵ_0 and ω, when ΔP is increased from 2.13 bar to 8.27 bar, C_{yy} increases by a factor of ~2. When the high pre-swirl insert was used for $\epsilon_0 \leq 0.53$, C_{xx}, C_{yy} measured values closely approximated those of the zero pre-swirl insert for all conditions. However, for $\epsilon_0 = 0.80$, C_{xx} and C_{yy} increased in magnitude by a factor of 3, and 2, respectively, as compared to the values measured at $\epsilon_0 \leq 0.53$.

As for the cross-coupled damping coefficients, C_{xy} and C_{yx} were largely unaffected by ΔP and $\epsilon_0 \in [0.00, 0.53]$. Over the range $\epsilon_0 = [0.00, 0.53]$, and for all ΔP, C_{xy} and C_{yx} are approximately equal in magnitude and opposite in sign; i.e., gyroscopic damping. In moving from ϵ_0 = 0.53 to ϵ_0 = 0.80, C_{xy} and C_{yx} decreased by a factor of 5, making both cross-coupled damping coefficients negative causing them to be dissipative damping. When ω is increased from 2 krpm to 8 krpm, the cross-coupled damping coefficient magnitudes increase by a factor of ~4 independent of the remaining variables. When the high pre-swirl insert was used in place of the zero pre-swirl insert for $\epsilon_0 \leq$0.53, C_{xy} and C_{yx} experience a ~40-50% increase in magnitude.

The seals direct virtual mass coefficients, M_{xx} and M_{yy}, were generally unaffected by ω and $\epsilon_0 \in$ [0.00, 0.53] while they increased with increasing *ΔP* for all of the pre-swirl inserts. M_{xx} and M_{yy} are above 12 kg for all of the measured data points. In general, $M_{xx} \cong M_{yy}$ for $\epsilon_0 \leq$ 0.53. For the zero pre-swirl insert, when moving from ϵ_0 = 0.53 to ϵ_0 = 0.80, the magnitude of the direct virtual mass increased by 50% for M_{xx} and by a factor of ~2.5 for M_{yy}. For the high pre-swirl insert when moving from ϵ_0 = 0.53 to ϵ_0 = 0.80, M_{xx} increased by a factor of 1.5, while M_{yy} increased by a factor of 2. At ϵ_0 = 0.53, *ΔP* = 8.27 bar, and ω = 6 krpm, when PSR increased from 0.1 to 0.45, M_{xx} was unaffected, but M_{yy} increased by factor of 1.5.

Regarding the cross-coupled virtual mass coefficients, M_{xy} and M_{yx} were unaffected by changing: (a) $\epsilon_0 \in$ [0.00, 0.53], (b) ω over the full range, (c) *ΔP* over the full range, and (d) increasing pre-swirl. $M_{xy} \cong -M_{yx}$ for $\epsilon_0 \leq$ 0.53. In moving from ϵ_0 = 0.53 to ϵ_0 = 0.80, M_{yx} increased in magnitude by a factor of 10 for the zero pre-swirl insert and by a factor of 3 for the high pre-swirl insert, but generally maintain $M_{xy} \cong -M_{yx}$, implying a stabilizing seal over the range of tested values. At ϵ_0 = 0.53, *ΔP* = 8.27 bar, and ω = 6 krpm, when PSR increased from 0.1 to 0.45, M_{xy} was unaffected, while M_{yx} increased in magnitude by a factor of ~5 .

For all pre-swirl inserts, whirl frequency ratio, WFR, was largely unaffected with changing ϵ_0 or ΔP except when the rotor was operating at ω = 2 krpm. At ω = 2 krpm, for the high pre-swirl insert, WFR decreased by ~20% with increasing ϵ_0 and increased by a factor of 2 with increasing ΔP. For the zero pre-swirl insert, WFR increased with increasing ω for all given conditions; for the high pre-swirl insert WFR decreased with increasing ω for all given conditions. This result highlights the destabilizing effect that higher pre-swirls have on the seal, particularly at low ω. For the zero pre-swirl insert, and $\epsilon_0 \leq 0.80$, the seals were generally the most stable when ω = 2 krpm.

The effective damping coefficients, C_{eff}, generally increased with increasing ΔP, and were highest and thus the most stable when ΔP = 8.27 bar, and ω = 2 krpm. At lower values of ΔP, and higher values of ω, C_{eff} converged to a similar value independent of the imposed pre-swirl. The effects of the imposed pre-swirl velocity are most prominent at ω = 2 krpm, and diminish as speed increases. At ω = 8 krpm, the imposed pre-swirl velocity did not affect C_{eff}. Overall the data showed that for increased PSR, (e.g. using the medium and high pre-swirl inserts), there is a marked decrease in effective damping and hence worse rotordynamic stability performance, indicating that inhibiting the inlet swirl velocity produces more favorable rotordynamic characteristics. For centered operation, the seal C_{eff} values were the most stable for ω > 2 krpm, and ΔP = 8.27 bar.

7.3 Measurements vs. Predictions

7.3.1 Direct Stiffness

The magnitude and sign of the predicted values of the direct stiffness coefficients, K_{yy} and K_{xx} were generally larger than the experimental results for the tested cases except when ΔP

= 8.27 bar, ϵ_0 = 0.80 for K_{yy}, and ϵ_0 > 0.27 for K_{xx}. In these exception cases, the predicted K_{yy} and K_{xx} values are smaller than the experimental results by a factor of 2. The sign of the predicted values of K_{xx} were often opposite that of the measured values for $\Delta P \geq$ 6.21 bar and ϵ_0 = 0.80.

Recall Fig. 59 and Fig. 60, which show the predicted and experimental results between K_{yy} and K_{xx} versus ϵ_0 for ΔP = 8.27 bar for ω = 2 krpm and ω = 6 krpm, respectively. For ω = 6 krpm, the predicted values of K_{yy} and K_{xx} are within 5% of the experimental values, contrasted with ω = 2 krpm, where the predicted values are within 1.8 times the experimental values on average. Indicating that at higher speeds, the predicted values more closely match the experimental values. This same trend is evident in Fig. 62 and Fig. 64.

As shown in Fig. 62, for ω = 2 krpm and $\epsilon_0 \in$ [0.00, 0.80] there was a large drop in the experimental values of K_{yy} and K_{xx} when the total Reynolds number traversed ~2000-2300 or the mid-transitional regime that was not predicted.

Recall Fig. 62 and Fig. 63 which show the predicted and experimental results between K_{yy} and K_{xx} versus ΔP for ω = 2 krpm for ϵ_0 = 0.00 for and ϵ_0 = 0.80, respectively. When ϵ_0 = 0.00, the predicted values are consistently greater than the experimental values by an average factor of 2.25, and a factor of 4.5 at its peak. Contrasted with ϵ_0 = 0.80 where the magnitude of the predicted values is generally smaller than the experimental values by an approximate factor of 1.5.

7.3.2 Cross-coupled Stiffness

Regarding the cross-coupled stiffness predictions, there was no clear pattern for when the predicted values of K_{xy} and K_{yx} would be larger or smaller than the experimental values. In general, XLAnSeal did an adequate job of predicting the trends of the cross-coupled stiffness experimental values for all tested parameters; i.e., changed due to changing ϵ_0, ω, $\mathit{\Delta P}$, and imposed PSR. With a few exceptions, the predictions were generally within 10-50% of the experimental values. The predicted values of K_{xy} and K_{xy} often did not match the sign of the corresponding experimental data.

7.3.3 Direct Damping

The predicted values of the seals direct damping coefficients, C_{xx} and C_{yy}, are generally larger than the experimental values by 10-50% for ω $\geq$ 4 krpm. When ω = 2 krpm with the zero pre-swirl insert, the experimental values were generally greater than the predicted values by 10-30%. When ω = 2 krpm with the high pre-swirl insert, at ϵ_0 =0.8 the experimental values of C_{yy} were larger than the predicted values by a factor of 2 at *ΔP* = 8.27 bar. The accuracy of the predicted values of C_{xx} and C_{yy} are generally unaffected by increasing *ΔP*. The predicted signs consistently match that of the experimental values.

7.3.4 Cross-coupled Damping

As for the predicted values of C_{xy} and C_{yx}, for $\epsilon_0 \in$ [0.00, 0.53] the magnitude of C_{xy} is generally 10- 25% smaller than the experimental values, and the magnitude of C_{yx} are both larger and smaller than the experimental values, but generally within 10-40%. However, when ω = 2 krpm, and ϵ_0 = 0.80, the predicted magnitudes of C_{xy}, and C_{yx} are up to ~2 times larger than the experimental values. When ϵ_0 = 0.8, all the predicted values of C_{xy}, and C_{yx} were larger in magnitude than the experimental results. The sign of the predicted values consistently matched those of the experimental values. The accuracy of the predicted values of C_{xy} and C_{yx} are generally unaffected by increasing *ΔP*, and imposed inlet swirl velocity.

7.3.5 Direct Virtual Mass

The experimental values of the seal's direct virtual mass coefficients, M_{xx} and M_{yy}, were generally larger than the predicted values by a factor of 2 for $\epsilon_0 \in [0.00, 0.53]$. The predictions are the least accurate for M_{yy} at $\epsilon_0 = 0.80$, where the predictions are smaller than the experimental values by a factor of 6. The accuracy of the predicted values of M_{xx} and M_{yy} were relatively unaffected by changing *ΔP*, ω, and imposed inlet swirl velocity.

7.3.6 Cross-coupled Virtual Mass

As for M_{xy} and M_{yx}, the predicted values of M_{xy} are generally larger than the experimental results by 10% for $0.27 < \epsilon_0 < 0.53$. When $\epsilon_0 = 0.00$, and $\epsilon_0 = 0.80$, the predicted values for M_{yx} are larger than the predicted magnitudes by a factor of ~3.5-5. The prediction accuracy of M_{xy} and M_{yx} were relatively unaffected by changing *ΔP*, ω, and PSR. The signs of the predictions and the experimental results for M_{xy} and M_{yx} were often opposite, i.e. the predicted values indicated that the seal would be destabilizing, but the experimental results showed that the seal was actually stabilizing.

7.3.7 Whirl Frequency Ratio

For the zero pre-swirl insert, the calculated experimental values of WFR were generally larger than the values calculated from the predicted values by a factor of 1.5 to 2 for $\Delta P < 8.27$ bar; i.e., the seals were less stable than predicted. An exception occurred when $\Delta P = 8.27$ bar, ω

$\geq$ 4 krpm, and $\epsilon_0 < 0.4$ where XLAnSeal generally over-predicts WFR; i.e., the seals were more stable than predicted by XLAnSeal.

When the high pre-swirl insert was used, the predicted values no longer followed the same trends as the experimental values. Specifically for the high pre-swirl insert, and ω = 2 krpm, XLAnSeal predicted that the WFR would converge towards ~0.45-0.5. For the high pre-swirl insert and ω $\geq$ 4 krpm, XLAnSeal predicted that the WFR would be relatively constant at ~0.45-0.50 over the range of tested ϵ_0. For ω = [2, 4] krpm, the experimental data for the high pre-swirl insert showed that WFR was relatively unaffected by increasing ϵ_0.

7.3.8 Effective Damping

For seals operating in the centered position, C_{eff} provides a good comparison of the seal's stabilizing capacity. Predicted C_{eff} values were typically larger than the experimental values by a factor of 1.2-1.5, but could be as much as 2 times larger. Overall, the seal was less stabilizing than predicted. In general, the predictions were more accurate at low ω, and low ΔP. There is not a significant difference in the accuracy of the predicted C_{eff} values between the zero, medium, and high pre-swirl insert.

7.4 Future Recommendations

Overall, increases in inlet swirl velocity negatively affects seal rotordynamic performance by increasing the magnitude of the cross-coupled stiffness values. As expected, the results presented show that reducing the inlet pre-swirl increases the overall stability of the seal. The results also show that the effect of changing the inlet swirl velocity diminished at 8 krpm. Overall, inlet swirl could be reduced by using swirl brakes or negative-swirl inlet geometries. Swirl brakes and negative-swirl inlet geometries have been used to reduce inlet pre-swirl velocities and eliminate rotordynamic instabilities in pump and compressor seals, respectively. Additionally, a study dedicated to testing at ϵ_0 > 0.6 should be conducted to investigate the large increases in the rotordynamic stiffness, damping, and virtual mass coefficients magnitude at large eccentricities. The information gathered from investigating high eccentricity operating points could be used to better predict and diagnose abnormal operating conditions and misalignment from poor dimensional assemblies.

XLAnSeal does an adequate job at predicting rotordynamic damping coefficients, but does a poor job predicting the direct stiffness and virtual mass coefficients when the Lomakin Effect dominates the centering forces; e.g., combinations of low $\dot{Q}$, low ϵ_0, low ω, or high ΔP. An examination of the applicability of the Zirkelback and San Andrés [16] model for transitional test data should be conducted. From the data in this thesis, a friction factor vs Reynolds number graph could be extracted to examine the discrepancy with the direct stiffness predictions.

A computational fluid dynamic (CFD) analysis should be developed to determine the best location for the OSR pitot tube, allowing a more thorough analysis on the effects of outlet swirl velocity on rotordynamic coefficients. With this CFD analysis, different pre-swirl inserts and swirl-brake designs can be investigated, giving additional insight for measured test programs including testing inlet swirl that opposes rotational motion of the rotor. Additional tests should be conducted to measure the effects of swirl-brakes on liquid annular seals with imposed pre-swirl to determine the extent to which rotordynamic characteristics can be improved by decreasing the inlet swirl velocity.

REFERENCES

[1] Childs, D.W., Norrbin, C.S., and Phillips, S., 2014, “A Lateral Rotordynamics Primer on Electrical Submersible Pumps for Deep Subsea Applications” *Proceedings of the 30th Pump User's Symposia*, 2014.

[2] Black, H.F., 1979, "Effects of Fluid-Filled Clearance Spaces on Centrifugal Pump and Submerged Motor Vibrations," in *Eighth Turbomachinery Symposium*, College Station, Texas, Texas A&M University, pp. 29-34.

[3] Nelson, C., and Nguyen, D., 1988, "Analysis of Eccentric Annular Incompressible Seals: Part 1 - A New Solution Using Fast Fourier Transforms for Determining Hydrodynamic Force," *Journal of Tribology,* **110**, pp. 354-359.

[4] Nelson, C., and Nguyen, D., 1988, "Analysis of Eccentric Annular Incompressible Seals: Part 2 – Effects of Eccentricity on Rotordynamic Coefficients," *Journal of Tribology,* **110**, pp. 361-366.

[5] San Andrés, L., "Notes 6 - Dynamics of a Rigid Rotor-Fluid Film Bearing System," 2009. [Online]. Available: http://rotorlab.tamu.edu/tribgroup/default.htm. [Last Accessed May 2016]

[6] Childs, D.W., 2013, *Turbomachinery Rotordynamics with Case Studies*, Wellborn, Texas: Minter Spring Publishing.

[7] Lomakin, A., 1958, "Calculation of Critical Number of Revolutions and the Conditions Necessary for Dynamic Stability of Rotors in High-Pressure Hydraulic Machines When Taking Into Account Forces Originating in Sealings," *Journal for Power and Mechanical Engineering (In Russian),* **14**.

[8] Moreland, A., 2016, “Influence of Pre-swirl and Eccentricity in Smooth Stator/Grooved Rotor Liquid Annular Seals, Measured Static and Rotordynamic Characteristics,” M.S. Thesis, Texas A&M University, College Station, Texas.

[9] Lund, J., 1966, *Self-excited, Stationary Whirl Orbits of a Journal in a Sleeve Bearing*, Rensselaer Polytechnic Institute.

[10] Black, H.F., Allaire, P., and Barret, L., 1981, "Inlet Flow Swirl in Short Turbulent Annular Seal Dynamics," in *Ninth International Conference on Fluid Sealing*, Noordwijkerhout, Netherlands, pp. 141-152.

[11] Iwatsubo, T., Sheng, B., and Matsumoto, T., 1989, “An Experimental Study on the Static and Dynamic Characteristics of Pump Annular Seals,” in *Rotordynamic Instability Problems in High Performance Turbomachinery,* NASA, Lewis Research Center, pp. 229-251.

[12] Torres, J. M., 2016, “Static and Rotordynamic Characteristics of Liquid Annular Seals with a Circumfrentially-Grooved Stator and Smooth Rotor Using Three Levels of Circumfrential Inlet-Fluid Rotation,” M.S. Thesis, Texas A&M University, College Station, Texas.

[13] Jenssen, D.N., 1970, “Dynamics of Rotor Systems Emboyding High Pressure Ring Seals,” Ph.D. Dissertation, Heriot-Watt University, July 1970, Edinburgh, Scotland.

[14] Childs, D.W., 1983, “Dynamic Analysis of Turbulent Annular Seals Bassed on Hirs’ Lubrication Equation,” *ASME Journal of Lubrcation Technology*, **105**: pp. 429-436.

[15] Falco, M., Mimmi, G., and Marenco, G., 1986, “Effects of Seals on Rotor Dynamics,” in *Proceedings of the International Conference on Rotordynamics,* Tokyo, Japan.

[16] Zirkelback, N. and San Andrés, L., 1996, “Bullk-Flow Model for the Transition to Turbulence Regime in Annular Seals,” *STLE Tribology Transactions*. **39**: pp. 835-842.

[17] Kanki, H. and Kawakam, T., 1984, “Experimental Study on the Dynamic Characteristics of Pump Annular Seals,” in *Proceedings of the Third IMechE International Conference on Vibrations in Rotating Machinery,* York, England, pp. 159-166.

[18] Marquette, O.R., Childs, D.W., and San Andrés, L., 1997, “Eccentricity effects on the rotordynamic coefficients of plain annular seals: Theory versus experiment,” *ASME Journal of Tribology,* **119**: pp. 443-447.

[19] Salas, J. 2015, “Influence of Pressure Dams in Liquid Annular Seals for ESP Applications, Measured Results for Leakage and Rotordynamic Characteristics,” M.S. Thesis, Texas A&M University, College Station, Texas.

[20] Kaul, A., 1999, “Design and Development of a Test Setup for the Experimental Determination of the Rotordynamic and Leakage Characteristics of Annular Bushing Oil Seals,” M.E. Report, Texas A&M University, College Station, Texas.

[21] Glienicke, J., 1966, "Experimental Investigation of the Stiffness and Damping Coefficients of Turbine Bearings and Their Application to Instability Prediction," in *Proceedings of the Institution of Mechanical Engineers*, **181**, pp. 116-129.

[22] Kulhanek, C. 2010, “Dynamic and Static Characteristics of a Rocker-Pivot, Tilting-Pad Bearing with 50% and 60% Offsets”, M.S. Thesis, Texas A&M University, College Station, Texas.

[23] Najeeb, O. 2017, “Static and Rotordynamic Analysis of a Plain Annular (Liquid) Seal in the Laminar Regime with a Swirl Brake for Three Clearances ,” M.S. Thesis, Texas A&M University, College Station, Texas.

[24] Kluitenberg, M. 2015, “Experimentally Determine the Impact of Jacking-oil Pockers on the Rotordynamic Characteristics of a Four-pad, LBP, Titing-pad Journal Bearing,” M.S. Thesis, Texas A&M University, College Station, Texas.

[25] Childs, D.W., and Hale, K., 1994, “A Test Apparatus and Facility to Identify the Rotordynamic Coefficients of High-Speed Hydrostatic Bearings,” *Journal of Tribology,* **116**, pp. 337-343.

[26] Beckwith, T., Marangoni, R., and Lienhard V, J., 2007, *Mechanical Measurements*, Upper Saddle River, NJ: Pearson Education, Inc.

[27] San Andrés, L., 1991, “Effect of Eccentricity on the Force Response of a Hybrid Bearing,” *Tribology Transactions,* **34**, pp. 537–544.

APPENDIX A TABULATED RESULTS

A.1 Zero Pre-swirl Insert Assembly

Table A. 1. Static results for the zero pre-swirl insert.

Test Point	Target			Measured					
	ω [rpm]	ΔP [bar]	ϵ_0 [-]	ω [rpm]	ΔP [bar]	ϵ_0 [-]	$\dot{Q}$ [LPM]	ϕ [rad]	F_r [N]
1	2000	2.07	0.00	2002.9	1.952	0.026	20.98	-1.285	18.65
2	2000	2.07	0.27	2003.7	2.003	0.275	19.79	0.262	87.06
3	2000	2.07	0.53	2004.7	2.006	0.529	22.13	0.523	143.99
4	2000	2.07	0.8	2004.4	2.040	0.799	26.68	0.956	264.30
5	2000	4.14	0.00	2004.2	4.102	0.033	39.48	0.220	21.92
6	2000	4.14	0.27	2004.2	3.988	0.294	39.61	0.188	123.04
7	2000	4.14	0.53	2004.8	4.107	0.531	40.40	0.331	207.91
8	2000	4.14	0.8	2004.7	4.044	0.800	42.63	0.706	326.66
9	2000	6.21	0.00	2004.8	6.090	0.061	53.98	-3.001	3.13
10	2000	6.21	0.27	2004.9	6.146	0.273	52.91	0.234	89.09
11	2000	6.21	0.53	2004.5	6.120	0.527	52.93	0.228	253.36
12	2000	6.21	0.8	2004.3	6.084	0.797	57.00	0.496	409.34
13	2000	8.27	0.00	2004.3	8.304	0.029	64.23	-0.914	4.81
14	2000	8.27	0.27	2004.3	8.222	0.274	63.96	0.572	89.19
15	2000	8.27	0.53	2004.3	8.276	0.526	65.30	0.234	331.63
16	2000	8.27	0.8	2003.7	8.649	0.816	69.27	0.478	530.13
17	4000	2.07	0.00	3999.7	2.016	0.024	15.37	0.984	6.05
18	4000	2.07	0.27	3999.8	1.914	0.269	15.41	1.179	72.98
19	4000	2.07	0.53	3999.9	2.007	0.537	18.94	1.220	201.57
20	4000	2.07	0.8	3999.4	1.928	0.807	18.87	1.328	450.50
21	4000	4.14	0.00	3999.6	4.002	0.084	35.41	2.417	22.63
22	4000	4.14	0.27	3999.7	4.069	0.277	35.34	1.164	123.14
23	4000	4.14	0.53	3999.5	4.054	0.523	35.39	0.961	254.08
24	4000	4.14	0.8	4003.8	4.576	0.796	38.85	1.172	423.32
25	4000	6.21	0.00	3999.7	6.220	0.097	48.90	-1.060	-0.03
26	4000	6.21	0.27	4000.1	6.219	0.270	48.93	1.087	124.93
27	4000	6.21	0.53	3999.7	6.133	0.529	49.10	0.773	301.42
28	4000	6.21	0.8	4003.6	6.508	0.812	53.86	1.022	560.34
29	4000	8.27	0.00	4001.3	8.213	0.016	58.38	-0.803	2.33
30	4000	8.27	0.27	3999.4	8.069	0.282	58.68	0.864	136.54
31	4000	8.27	0.53	3999.5	8.142	0.532	60.90	0.621	354.53
32	4000	8.27	0.8	4003.5	8.654	0.794	65.65	0.841	620.30

Table A. 1. Static results for the zero pre-swirl insert. (Continued)

Test Point	Target			Measured					
	ω [rpm]	ΔP [bar]	ϵ_0 [-]	ω [rpm]	ΔP [bar]	ϵ_0 [-]	$\dot{Q}$ [LPM]	ϕ [rad]	F_r [N]
33	6000	2.07	0.00	6003.8	1.933	0.029	11.45	-2.007	2.66
34	6000	2.07	0.27	6004.3	1.909	0.278	11.85	1.504	186.71
35	6000	2.07	0.53	6003.9	1.978	0.532	14.62	1.553	380.65
36	6000	2.07	0.8	6004.9	2.467	0.806	15.83	1.369	693.40
37	6000	4.14	0.00	6006.3	4.114	0.027	26.45	-1.922	3.22
38	6000	4.14	0.27	6005.5	4.059	0.267	26.52	1.426	194.85
39	6000	4.14	0.53	6005.5	4.046	0.527	28.82	1.371	388.25
40	6000	4.14	0.8	6004.0	4.435	0.786	32.44	1.382	679.95
41	6000	6.21	0.00	6005.8	6.162	0.019	39.18	2.077	5.52
42	6000	6.21	0.27	6005.4	6.064	0.273	39.32	0.985	203.32
43	6000	6.21	0.53	6004.5	6.043	0.528	42.89	1.070	397.76
44	6000	6.21	0.8	6005.2	6.600	0.817	49.72	1.249	933.53
45	6000	8.27	0.00	6005.0	8.223	0.034	50.72	1.727	0.93
46	6000	8.27	0.27	6005.2	8.108	0.279	51.09	0.919	226.41
47	6000	8.27	0.53	6004.6	8.237	0.523	55.50	1.087	455.03
48	6000	8.27	0.8	6004.5	8.738	0.812	61.10	1.155	1002.88
49	8000	2.07	0.00	8004.2	2.094	0.043	10.69	0.707	3.69
50	8000	2.07	0.27	8004.8	1.930	0.275	10.72	1.474	230.77
51	8000	2.07	0.53	7998.1	2.380	0.535	12.58	1.609	392.60
52	8000	2.07	0.8	7999.4	2.312	0.816	14.91	1.237	1290.62
53	8000	4.14	0.00	7998.3	3.957	0.028	22.07	-1.928	0.63
54	8000	4.14	0.27	8005.2	3.779	0.272	22.22	1.446	266.70
55	8000	4.14	0.53	7996.9	4.279	0.517	26.16	1.533	436.78
56	8000	4.14	0.8	7998.5	4.492	0.809	31.86	1.386	1300.26
57	8000	6.21	0.00	7997.7	5.983	0.031	33.88	-2.446	-0.92
58	8000	6.21	0.27	7997.7	6.038	0.272	34.63	1.267	266.64
59	8000	6.21	0.53	7995.8	6.526	0.550	38.84	1.389	533.75
60	8000	6.21	0.8	7996.8	6.468	0.801	44.12	1.374	1312.89
61	8000	8.27	0.00	7998.5	8.208	0.021	45.25	1.954	0.83
62	8000	8.27	0.27	7998.0	8.108	0.265	45.52	1.094	271.85
63	8000	8.27	0.53	7998.6	8.350	0.575	48.99	1.269	634.44
64	8000	8.27	0.8	7996.4	8.611	0.812	55.89	1.309	1454.18

Table A. 2. Flow results for the zero pre-swirl insert.

Test Point	Pre-swirl Ratio [-]	Post-swirl Ratio [-]	Inlet Temp. [°C]	Outlet Temp. [°C]	Re_z [-]	Re_θ [-]	Re_t [-]
1	0.000	0.264	47.455	49.796	967.6	871.8	1302.4
2	0.000	0.295	45.612	44.381	883.1	843.9	1221.5
3	0.000	0.330	45.398	44.812	983.7	841.2	1294.3
4	0.000	0.317	47.008	49.308	1220.8	865.4	1496.5
5	0.000	0.311	45.902	45.687	1771.0	848.4	1963.7
6	0.000	0.311	46.083	48.123	1782.6	851.2	1975.4
7	0.000	0.340	45.516	46.027	1800.0	843.0	1987.6
8	0.000	0.362	46.971	46.454	1949.0	865.0	2132.3
9	0.000	0.283	47.049	49.035	2471.6	866.2	2619.0
10	0.000	0.305	46.623	46.538	2403.8	859.7	2552.9
11	0.000	0.331	45.391	45.568	2352.9	841.0	2498.7
12	0.000	0.391	45.336	46.863	2531.7	840.1	2667.4
13	0.000	0.287	47.981	49.643	2991.1	880.9	3118.1
14	0.000	0.346	46.364	46.413	2892.7	855.5	3016.5
15	0.000	0.387	47.661	49.261	3023.3	875.7	3147.6
16	0.182	0.411	46.926	46.974	3164.8	854.3	3278.0
17	0.234	0.255	45.383	45.993	683.4	1677.8	1811.7
18	0.237	0.237	45.611	47.056	687.6	1684.6	1819.5
19	0.206	0.251	47.332	49.616	871.4	1737.2	1943.5
20	0.200	0.260	47.666	48.022	873.9	1747.6	1953.9
21	0.138	0.251	45.709	46.131	1583.1	1687.4	2313.8
22	0.126	0.267	46.166	46.526	1592.5	1701.1	2330.2
23	0.108	0.273	46.442	46.914	1602.7	1709.4	2343.2
24	0.087	0.296	45.785	45.040	1739.3	1672.8	2413.2
25	0.054	0.269	47.798	49.704	2269.6	1751.9	2867.1
26	0.060	0.273	47.560	47.481	2261.1	1744.5	2855.8
27	0.040	0.274	46.278	46.741	2217.3	1704.5	2796.7
28	0.015	0.286	45.387	47.089	2394.4	1661.1	2914.2
29	0.092	0.274	45.331	45.935	2592.4	1677.0	3087.5
30	0.069	0.278	47.609	47.778	2714.1	1745.8	3227.1
31	0.000	0.325	46.915	48.939	2781.7	1724.0	3272.6
32	0.000	0.347	46.906	48.411	2997.9	1706.4	3449.5

Table A. 2. Flow results for the zero pre-swirl insert. (Continued)

Test Point	Pre-swirl Ratio [-]	Post-swirl Ratio [-]	Inlet Temp. [°C]	Outlet Temp. [°C]	Re_z [-]	Re_θ [-]	Re_t [-]
33	0.300	0.172	45.638	47.442	511.1	2529.8	2580.9
34	0.289	0.321	45.304	47.292	526.2	2515.2	2569.7
35	0.268	0.228	46.169	49.247	658.9	2553.7	2637.3
36	0.265	0.192	47.285	47.106	728.0	2577.0	2677.9
37	0.230	0.232	45.953	47.199	1187.4	2544.9	2808.3
38	0.223	0.258	46.479	47.368	1201.9	2568.5	2835.8
39	0.204	0.260	47.270	48.157	1324.9	2605.3	2922.8
40	0.187	0.270	45.144	44.131	1436.0	2480.5	2866.2
41	0.185	0.229	45.757	46.825	1753.0	2535.9	3082.8
42	0.171	0.253	45.723	46.707	1758.4	2534.2	3084.5
43	0.152	0.263	45.812	47.982	1920.8	2537.8	3182.8
44	0.122	0.265	46.981	49.193	2273.5	2563.0	3426.1
45	0.158	0.237	45.682	46.607	2266.3	2532.2	3398.3
46	0.141	0.277	46.076	46.862	2298.6	2550.0	3433.1
47	0.119	0.275	47.179	47.647	2546.8	2600.6	3640.0
48	0.118	0.305	47.500	47.267	2820.6	2587.0	3827.3
49	0.361	0.112	47.572	50.955	493.9	3491.5	3526.2
50	0.346	0.170	46.417	50.479	485.5	3419.8	3454.0
51	0.314	0.290	45.362	49.653	559.0	3316.9	3363.7
52	0.303	0.211	45.453	49.564	663.4	3322.7	3388.3
53	0.261	0.295	47.656	49.893	1021.6	3494.2	3640.5
54	0.253	0.305	47.662	52.118	1028.9	3497.7	3645.9
55	0.234	0.266	46.408	50.109	1184.2	3378.2	3579.8
56	0.214	0.248	47.073	50.659	1459.3	3419.5	3717.9
57	0.230	0.236	47.017	49.214	1550.1	3453.7	3785.6
58	0.218	0.239	46.621	48.599	1573.3	3429.2	3772.9
59	0.199	0.248	48.274	50.807	1818.4	3494.1	3939.0
60	0.180	0.263	48.437	51.194	2072.0	3505.2	4071.8
61	0.201	0.226	45.992	47.724	2032.9	3391.4	3954.0
62	0.190	0.253	46.248	48.063	2054.4	3406.6	3978.2
63	0.180	0.266	46.053	46.263	2203.6	3357.7	4016.2
64	0.158	0.261	47.188	47.035	2565.5	3425.7	4279.9

Table A. 3. Stiffness coefficients and uncertainties for the zero pre-swirl insert.

Test Point	K_{xx} [MN/m]	$U_{K_{xx}}$ [MN/m]	K_{xy} [MN/m]	$U_{K_{xy}}$ [MN/m]	K_{yx} [MN/m]	$U_{K_{yx}}$ [MN/m]	K_{yy} [MN/m]	$U_{K_{yy}}$ [MN/m]
1	0.79	0.12	0.37	0.06	-0.46	0.06	0.80	0.12
2	0.60	0.10	0.68	0.05	-0.54	0.06	0.49	0.14
3	0.16	0.14	1.47	0.11	-0.72	0.17	0.32	0.32
4	-1.97	1.00	3.41	0.61	-4.70	0.70	2.19	0.88
5	2.57	0.15	0.12	0.11	-0.39	0.07	2.49	0.11
6	1.51	0.21	0.71	0.07	-0.37	0.07	1.21	0.17
7	1.16	0.16	1.40	0.08	-0.71	0.13	1.20	0.32
8	-1.19	0.90	4.51	0.79	-3.21	0.91	2.57	1.45
9	0.26	0.22	0.53	0.13	-1.20	0.08	0.07	0.26
10	1.40	0.18	-0.06	0.08	-1.02	0.08	3.07	0.18
11	2.13	0.12	1.10	0.10	-0.74	0.08	2.54	0.33
12	0.19	0.53	5.28	0.72	-2.12	0.68	2.69	2.00
13	1.01	0.21	0.56	0.11	-0.84	0.08	1.32	0.19
14	2.17	0.19	-1.19	0.08	-2.14	0.07	3.36	0.15
15	3.21	0.11	0.66	0.10	-0.86	0.06	4.56	0.34
16	0.26	0.54	8.12	0.90	-3.17	2.04	8.53	5.12
17	-0.19	0.11	1.44	0.13	-1.44	0.05	-0.11	0.08
18	-0.25	0.13	1.57	0.10	-1.55	0.06	-0.10	0.08
19	-0.11	0.32	2.13	0.19	-2.58	0.11	0.36	0.10
20	0.68	2.34	3.64	0.61	-10.46	0.44	1.22	0.35
21	-0.61	0.07	2.19	0.10	-2.24	0.12	0.00	0.19
22	1.19	0.14	1.64	0.05	-2.33	0.14	0.32	0.07
23	0.89	0.16	2.09	0.14	-2.85	0.18	1.32	0.16
24	-2.42	2.87	5.98	0.85	-12.34	3.55	5.13	5.49
25	0.00	0.15	2.03	0.22	-2.07	0.20	-0.27	0.10
26	1.95	0.15	1.37	0.13	-2.74	0.07	0.51	0.09
27	1.91	0.12	1.82	0.18	-2.86	0.15	2.63	0.19
28	-3.91	2.15	8.28	1.07	-12.13	4.76	6.54	5.88
29	0.75	0.11	1.77	0.19	-1.71	0.17	0.84	0.12
30	1.43	0.10	1.53	0.07	-2.38	0.12	1.56	0.13
31	2.98	0.09	1.40	0.17	-2.89	0.14	4.13	0.17
32	-2.74	1.40	9.13	1.02	-11.31	3.15	9.57	3.82

Table A. 3. Stiffness coefficients and uncertainties for the zero pre-swirl insert. (Continued)

Test Point	K_{xx} [MN/m]	$U_{K_{xx}}$ [MN/m]	K_{xy} [MN/m]	$U_{K_{xy}}$ [MN/m]	K_{yx} [MN/m]	$U_{K_{yx}}$ [MN/m]	K_{yy} [MN/m]	$U_{K_{yy}}$ [MN/m]
33	-0.42	0.05	2.92	0.06	-2.95	0.05	-0.31	0.07
34	-0.44	0.13	3.02	0.11	-3.35	0.08	-0.46	0.07
35	-0.39	0.37	3.74	0.26	-5.17	0.15	-0.49	0.08
36	10.25	1.82	5.01	0.50	-20.76	1.82	3.22	0.81
37	0.28	0.22	3.39	0.22	-3.31	0.12	0.23	0.29
38	0.32	0.14	3.47	0.18	-3.55	0.12	0.36	0.18
39	-0.43	0.31	3.90	0.24	-5.02	0.19	0.35	0.25
40	2.01	2.45	6.62	0.52	-19.85	1.09	3.16	0.98
41	1.80	0.12	3.07	0.10	-3.08	0.10	1.96	0.09
42	1.51	0.08	3.23	0.10	-3.23	0.11	1.80	0.13
43	0.42	0.27	4.32	0.21	-4.13	0.17	1.66	0.26
44	1.12	1.57	7.43	0.69	-26.31	3.37	7.48	2.21
45	2.93	0.10	3.22	0.22	-3.20	0.20	3.15	0.10
46	1.58	0.16	3.88	0.22	-2.80	0.11	2.56	0.23
47	3.00	0.14	3.41	0.14	-4.92	0.14	2.34	0.14
48	-3.20	2.95	9.02	0.97	-23.67	3.18	9.64	2.91
49	-0.87	0.08	4.44	0.10	-4.48	0.05	-0.88	0.07
50	-1.02	0.16	4.74	0.14	-5.07	0.10	-0.97	0.09
51	-0.52	0.39	6.32	0.38	-9.06	0.50	-0.82	0.73
52	25.03	1.23	1.94	0.61	-33.85	2.61	9.72	1.69
53	-0.16	0.16	4.60	0.12	-4.72	0.10	-0.01	0.14
54	-0.22	0.17	4.90	0.19	-5.35	0.08	-0.14	0.16
55	-0.79	0.35	6.40	0.24	-9.95	1.14	-0.34	1.06
56	17.01	1.44	8.83	0.53	-29.78	1.05	4.37	1.24
57	0.64	0.23	5.37	0.27	-5.26	0.21	0.86	0.18
58	0.57	0.24	5.62	0.30	-5.78	0.24	0.82	0.21
59	-0.79	0.46	6.60	0.26	-10.44	1.40	0.55	1.64
60	7.26	1.69	8.90	0.71	-29.69	2.09	4.99	1.42
61	2.33	0.10	4.86	0.11	-4.94	0.20	2.47	0.11
62	1.92	0.11	5.11	0.14	-5.27	0.17	2.38	0.12
63	-0.53	0.44	7.38	0.36	-8.83	0.81	2.57	0.60
64	4.94	1.64	9.20	0.56	-33.55	3.25	8.17	2.03

Table A. 4. Damping coefficients and uncertainties for the zero pre-swirl insert.

Test Point	C_{xx} [kN-s/m]	$U_{C_{xx}}$ [kN-s/m]	C_{xy} [kN-s/m]	$U_{C_{xy}}$ [kN-s/m]	C_{yx} [kN-s/m]	$U_{C_{yx}}$ [kN-s/m]	C_{yy} [kN-s/m]	$U_{C_{yy}}$ [kN-s/m]
1	6.48	0.60	2.02	0.13	-1.98	0.11	6.67	0.53
2	6.80	0.61	1.92	0.10	-2.23	0.13	7.84	0.79
3	9.62	0.83	-0.01	0.25	-4.72	0.23	13.19	1.19
4	51.21	3.17	-22.80	1.63	-29.36	1.71	34.64	2.23
5	9.58	0.54	1.99	0.16	-1.67	0.16	9.89	0.40
6	10.83	0.40	1.82	0.16	-1.59	0.11	11.35	0.49
7	12.14	0.46	1.28	0.15	-2.60	0.22	16.08	0.81
8	36.27	2.19	-20.01	1.82	-25.94	1.72	47.07	2.92
9	14.87	0.77	1.51	0.23	-0.75	0.21	15.17	0.38
10	14.09	0.37	2.29	0.16	-0.94	0.12	13.08	0.21
11	14.40	0.30	2.10	0.20	-1.86	0.23	17.55	0.69
12	28.72	1.38	-14.23	1.76	-19.74	1.70	55.20	4.11
13	16.13	0.50	1.84	0.26	-1.18	0.20	16.17	0.30
14	16.29	0.48	2.62	0.19	-0.49	0.19	15.64	0.20
15	16.26	0.41	2.15	0.13	-1.83	0.14	18.45	0.58
16	34.55	1.32	-22.93	2.00	-24.56	4.60	78.59	11.99
17	6.38	0.84	4.03	0.24	-4.10	0.12	6.58	0.67
18	7.23	0.87	3.89	0.20	-4.39	0.13	7.00	0.69
19	12.41	1.13	2.39	0.25	-6.50	0.30	9.58	0.96
20	55.27	3.80	-3.47	1.13	-15.63	1.11	18.41	1.08
21	11.66	0.75	3.93	0.17	-3.62	0.24	11.35	0.57
22	10.31	0.64	3.85	0.18	-3.89	0.22	11.47	0.58
23	12.69	0.76	2.84	0.14	-5.96	0.20	13.20	0.75
24	61.56	5.88	-13.75	1.79	-35.98	8.53	32.54	4.32
25	13.95	0.55	3.75	0.39	-3.25	0.33	13.86	0.32
26	13.60	0.43	3.76	0.26	-3.50	0.28	13.98	0.30
27	14.49	0.51	3.21	0.28	-5.34	0.26	16.38	0.63
28	63.90	4.82	-21.68	2.20	-46.04	11.97	50.97	8.04
29	15.40	0.23	3.47	0.56	-3.25	0.53	15.46	0.21
30	15.90	0.49	3.38	0.22	-3.99	0.27	15.53	0.32
31	16.06	0.57	3.71	0.25	-4.95	0.25	18.32	0.50
32	50.57	3.88	-19.22	2.62	-31.38	3.64	49.72	4.74

Table A. 4. Damping coefficients and uncertainties for the zero pre-swirl insert. (Continued)

Test Point	C_{xx} [kN-s/m]	$U_{C_{xx}}$ [kN-s/m]	C_{xy} [kN-s/m]	$U_{C_{xy}}$ [kN-s/m]	C_{yx} [kN-s/m]	$U_{C_{yx}}$ [kN-s/m]	C_{yy} [kN-s/m]	$U_{C_{yy}}$ [kN-s/m]
33	8.15	0.71	6.09	0.17	-6.34	0.11	8.49	0.73
34	9.54	0.92	6.48	0.16	-6.50	0.16	8.92	0.76
35	15.82	1.45	6.88	0.37	-7.54	0.42	10.78	0.83
36	58.67	4.09	-6.09	1.68	-21.90	4.69	21.62	2.62
37	11.38	0.56	5.32	0.38	-5.63	0.19	12.11	0.57
38	11.84	0.83	5.31	0.28	-5.94	0.18	11.55	0.90
39	17.11	0.70	5.73	0.32	-8.09	0.33	14.00	0.50
40	62.53	5.89	-1.24	1.61	-18.86	4.99	19.92	3.33
41	11.80	0.44	6.34	0.15	-6.22	0.20	12.11	0.38
42	12.02	0.54	6.21	0.13	-6.46	0.23	12.46	0.47
43	15.13	1.11	5.50	0.33	-8.67	0.30	14.38	0.56
44	74.37	4.82	-11.34	1.65	-30.20	3.50	37.06	7.23
45	13.72	0.43	5.97	0.31	-5.71	0.40	14.02	0.29
46	14.15	0.80	5.66	0.35	-6.44	0.37	14.52	0.37
47	17.18	0.78	5.84	0.27	-7.78	0.26	16.62	0.44
48	67.80	3.99	-14.15	2.26	-31.92	6.73	42.76	7.91
49	9.05	0.76	8.31	0.19	-8.33	0.17	9.38	0.82
50	10.67	0.95	8.56	0.23	-8.64	0.26	9.87	0.90
51	19.70	2.01	8.44	0.67	-11.65	1.76	12.54	2.18
52	53.46	4.22	-14.25	1.18	-35.48	2.71	40.32	9.89
53	10.75	0.78	8.03	0.30	-8.07	0.25	11.08	0.84
54	12.33	0.89	8.08	0.31	-8.30	0.37	11.53	0.88
55	21.48	1.51	8.01	0.63	-12.55	4.32	15.87	1.58
56	67.89	3.74	-6.22	1.25	-25.33	4.32	29.38	3.55
57	13.80	0.49	7.07	0.39	-7.36	0.40	14.16	0.50
58	15.08	0.47	6.96	0.49	-7.97	0.30	14.76	0.55
59	24.40	1.52	7.89	0.67	-17.68	7.59	21.71	5.00
60	65.06	4.90	-1.09	1.55	-25.24	2.31	32.20	6.22
61	14.14	0.35	8.64	0.34	-8.45	0.32	14.25	0.46
62	14.83	0.49	8.36	0.23	-8.98	0.32	14.79	0.51
63	23.44	2.01	7.11	0.43	-14.99	0.94	20.15	1.92
64	70.33	4.97	-4.40	1.77	-28.59	3.49	36.59	6.48

Table A. 5. Virtual mass coefficients and uncertainties for the zero pre-swirl insert.

Test Point	M_{xx} [kg]	$U_{M_{xx}}$ [kg]	M_{xy} [kg]	$U_{M_{xy}}$ [kg]	M_{yx} [kg]	$U_{M_{yx}}$ [kg]	M_{yy} [kg]	$U_{M_{yy}}$ [kg]
1	14.47	0.16	0.34	0.08	0.05	0.08	14.72	0.16
2	14.60	0.13	0.39	0.07	-0.07	0.09	15.00	0.20
3	16.21	0.20	-0.17	0.15	-1.00	0.23	16.87	0.43
4	27.48	1.36	-4.74	0.83	-5.61	0.95	21.81	1.20
5	15.97	0.20	0.30	0.15	-0.06	0.09	16.26	0.15
6	15.72	0.29	0.28	0.09	-0.08	0.10	16.41	0.23
7	16.75	0.22	-0.36	0.11	-0.90	0.18	18.64	0.44
8	25.16	1.22	-5.21	1.08	-6.48	1.24	25.62	1.98
9	15.89	0.30	0.55	0.17	-0.23	0.11	16.09	0.35
10	16.22	0.25	0.01	0.12	-0.23	0.11	17.76	0.25
11	17.50	0.16	-0.08	0.14	-0.31	0.10	19.64	0.45
12	22.67	0.72	-3.79	0.98	-5.00	0.93	27.94	2.72
13	16.84	0.28	0.21	0.15	0.35	0.11	17.42	0.26
14	16.89	0.26	-0.23	0.11	-0.25	0.10	18.18	0.20
15	18.02	0.15	-0.13	0.14	-0.27	0.08	20.45	0.47
16	22.09	1.31	-1.13	2.20	-11.82	4.96	52.89	12.46
17	12.71	0.14	0.83	0.17	-0.35	0.07	13.10	0.11
18	13.11	0.17	0.66	0.14	-0.40	0.08	13.08	0.11
19	15.41	0.43	0.62	0.26	-0.91	0.16	13.59	0.14
20	29.35	3.19	-2.01	0.84	-2.73	0.60	15.42	0.48
21	14.72	0.10	0.42	0.14	-0.25	0.16	15.63	0.25
22	15.85	0.20	0.53	0.07	-0.57	0.19	15.48	0.10
23	17.83	0.22	-0.16	0.19	-1.46	0.25	16.62	0.22
24	34.58	4.02	-3.13	1.19	-9.64	4.96	29.67	7.67
25	16.17	0.20	0.53	0.29	-0.35	0.27	16.49	0.14
26	16.39	0.20	0.47	0.17	-0.09	0.10	16.49	0.13
27	18.17	0.17	-0.55	0.25	-1.14	0.21	18.17	0.26
28	32.07	3.00	-4.11	1.50	-13.48	6.66	33.88	8.22
29	17.09	0.16	0.09	0.26	0.33	0.23	17.49	0.16
30	17.00	0.13	0.30	0.10	0.09	0.17	17.60	0.17
31	18.46	0.12	-0.70	0.23	-0.97	0.19	19.37	0.24
32	28.91	3.41	-5.14	2.49	-20.78	7.66	48.68	9.30

Table A. 5. Virtual mass coefficients and uncertainties for the zero pre-swirl insert. (Continued)

Test Point	M_{xx} [kg]	$U_{M_{xx}}$ [kg]	M_{xy} [kg]	$U_{M_{xy}}$ [kg]	M_{yx} [kg]	$U_{M_{yx}}$ [kg]	M_{yy} [kg]	$U_{M_{yy}}$ [kg]
33	12.62	0.07	1.07	0.08	-0.84	0.07	12.95	0.10
34	13.26	0.18	1.18	0.15	-0.59	0.10	12.99	0.09
35	16.19	0.51	1.82	0.35	-0.24	0.21	13.68	0.11
36	32.67	4.44	-4.87	1.23	-16.10	4.43	19.52	1.98
37	12.74	0.30	1.11	0.30	-0.66	0.16	12.80	0.39
38	13.02	0.19	1.46	0.25	-0.83	0.16	12.61	0.25
39	17.82	0.42	0.43	0.33	-0.18	0.26	15.68	0.34
40	32.98	5.96	-1.32	1.26	-5.28	2.66	20.81	2.38
41	15.95	0.17	0.67	0.13	-0.45	0.13	16.41	0.12
42	16.19	0.11	0.54	0.14	-0.54	0.15	16.38	0.17
43	18.39	0.36	0.04	0.29	-1.50	0.24	17.72	0.35
44	35.57	3.83	-3.12	1.68	-23.40	8.20	41.32	5.39
45	16.52	0.14	0.84	0.30	-0.49	0.28	17.27	0.14
46	16.67	0.21	0.49	0.30	-0.02	0.15	17.17	0.31
47	18.35	0.19	-0.57	0.19	-1.52	0.19	17.67	0.20
48	29.00	7.18	-1.34	2.36	-23.84	7.75	47.00	7.09
49	12.65	0.11	1.46	0.14	-1.23	0.07	12.80	0.10
50	13.21	0.22	1.65	0.20	-1.12	0.13	12.95	0.13
51	16.38	0.92	3.48	0.90	-1.09	1.19	15.91	1.74
52	29.88	2.95	-7.43	1.47	-28.12	6.25	36.65	4.04
53	12.68	0.21	1.41	0.17	-1.34	0.14	13.02	0.20
54	13.34	0.23	1.74	0.26	-1.30	0.11	13.04	0.22
55	16.02	0.83	2.27	0.58	-6.01	2.72	16.06	2.53
56	31.25	3.45	-2.80	1.26	-14.42	2.51	27.07	2.97
57	12.89	0.31	1.59	0.36	-1.33	0.29	13.36	0.24
58	14.05	0.33	1.39	0.40	-1.13	0.32	13.88	0.28
59	19.65	1.09	-0.03	0.61	-5.95	3.34	21.08	3.91
60	32.86	4.12	-1.64	1.74	-16.39	5.08	35.67	3.46
61	16.55	0.13	0.39	0.15	-0.57	0.28	17.11	0.15
62	16.78	0.15	0.32	0.19	-0.44	0.23	17.04	0.17
63	20.80	0.73	0.54	0.60	-1.54	1.35	27.07	1.00
64	34.19	3.99	-2.62	1.36	-23.42	7.92	39.81	4.95

Table A. 6. Whirl frequency ratio, effective damping, and uncertainties for the zero pre-swirl insert.

Test Point	Target			Measured			
	ω [rpm]	ΔP [bar]	ϵ_0 ϵ_0	WFR [-]	U_{WFR} [-]	C_{eff} [kN-s/m]	$U_{C_{eff}}$ [kN-s/m]
1	2000	2.07	0.00	0.30	0.03	4.64	0.29
2	2000	2.07	0.27	0.40	0.04	4.47	0.42
3	2000	2.07	0.53	0.45	0.06	6.32	0.34
4	2000	2.07	0.8	0.49	0.10	24.70	-0.42
5	2000	4.14	0.00	0.10	0.05	8.56	0.04
6	2000	4.14	0.27	0.21	0.03	8.54	0.12
7	2000	4.14	0.53	0.34	0.03	9.20	0.14
8	2000	4.14	0.8	0.46	0.12	24.52	-1.51
9	2000	6.21	0.00	0.25	0.03	10.97	0.07
10	2000	6.21	0.27	0.00	0.00	11.02	-0.11
11	2000	6.21	0.53	0.26	0.02	11.65	0.07
12	2000	6.21	0.8	0.41	0.10	25.26	-0.60
13	2000	8.27	0.00	0.20	0.02	12.87	-0.05
14	2000	8.27	0.27	0.00	0.00	8.07	-0.02
15	2000	8.27	0.53	0.09	0.11	13.79	0.12
16	2000	8.27	0.8	0.31	0.46	31.01	-0.35
17	4000	2.07	0.00	0.53	0.05	3.29	0.55
18	4000	2.07	0.27	0.52	0.05	3.62	0.58
19	4000	2.07	0.53	0.52	0.05	5.69	0.68
20	4000	2.07	0.8	0.48	0.05	21.01	1.18
21	4000	4.14	0.00	0.46	0.02	6.34	0.40
22	4000	4.14	0.27	0.42	0.02	6.37	0.38
23	4000	4.14	0.53	0.45	0.03	7.39	0.38
24	4000	4.14	0.8	0.48	0.13	27.87	-0.15
25	4000	6.21	0.00	0.35	0.03	9.19	-0.06
26	4000	6.21	0.27	0.32	0.02	9.00	0.13
27	4000	6.21	0.53	0.35	0.02	10.21	0.17
28	4000	6.21	0.8	0.44	0.16	36.79	-0.53
29	4000	8.27	0.00	0.27	0.02	11.36	-0.21
30	4000	8.27	0.27	0.29	0.01	11.13	0.17
31	4000	8.27	0.53	0.27	0.02	12.42	0.17
32	4000	8.27	0.8	0.44	0.14	31.20	-0.66

Table A. 6. Whirl frequency ratio, effective damping, and uncertainties for the zero pre-swirl insert. (Continued)

Test Point	Target			Measured			
	ω [rpm]	ΔP [bar]	ε ϵ_0 [ ]	WFR [-]	U_{WFR} [-]	C_{eff} [kN-s/m]	$U_{C_{eff}}$ [kN-s/m]
33	6000	2.07	0.00	0.56	0.03	4.26	0.63
34	6000	2.07	0.27	0.55	0.04	4.72	0.70
35	6000	2.07	0.53	0.53	0.04	6.86	0.81
36	6000	2.07	0.8	0.46	0.05	26.25	1.51
37	6000	4.14	0.00	0.45	0.02	6.98	0.30
38	6000	4.14	0.27	0.48	0.03	6.84	0.62
39	6000	4.14	0.53	0.45	0.02	8.66	0.26
40	6000	4.14	0.8	0.53	0.06	22.25	3.33
41	6000	6.21	0.00	0.41	0.01	7.42	0.26
42	6000	6.21	0.27	0.42	0.02	7.45	0.34
43	6000	6.21	0.53	0.45	0.02	8.52	0.53
44	6000	6.21	0.8	0.44	0.06	37.23	2.80
45	6000	8.27	0.00	0.37	0.02	9.19	0.02
46	6000	8.27	0.27	0.36	0.02	9.18	0.32
47	6000	8.27	0.53	0.38	0.01	10.94	0.38
48	6000	8.27	0.8	0.42	0.07	37.20	2.65
49	8000	2.07	0.00	0.58	0.04	5.02	0.70
50	8000	2.07	0.27	0.57	0.04	5.57	0.79
51	8000	2.07	0.53	0.57	0.06	8.85	1.57
52	8000	2.07	0.8	0.18	0.09	40.42	5.13
53	8000	4.14	0.00	0.51	0.03	6.51	0.67
54	8000	4.14	0.27	0.51	0.03	7.10	0.72
55	8000	4.14	0.53	0.52	0.04	12.38	0.72
56	8000	4.14	0.8	0.42	0.04	32.80	2.71
57	8000	6.21	0.00	0.45	0.02	8.86	0.21
58	8000	6.21	0.27	0.46	0.02	9.18	0.19
59	8000	6.21	0.53	0.43	0.06	15.38	2.27
60	8000	6.21	0.8	0.43	0.05	33.14	3.89
61	8000	8.27	0.00	0.41	0.01	8.74	0.22
62	8000	8.27	0.27	0.42	0.01	8.93	0.31
63	8000	8.27	0.53	0.44	0.04	13.00	1.27
64	8000	8.27	0.8	0.42	0.05	38.84	3.45

A.2 Medium Pre-swirl Insert Assembly

Table A. 7. Static results for the medium pre-swirl insert.

Test Point	Target			Measured					
	ω [rpm]	ΔP [bar]	ϵ_0 [-]	ω [rpm]	ΔP [bar]	ϵ_0 [-]	$\dot{Q}$ [LPM]	ϕ [rad]	F_r [N]
1	2000	2.07	0.00	1991.0	2.067	0.042	19.22	1.810	6.45
2	2000	2.07	0.27	2002.4	2.024	0.276	21.22	0.622	81.79
3	2000	2.07	0.53	2002.7	2.071	0.538	21.26	0.782	145.23
4	2000	2.07	0.8	2003.2	2.031	0.800	26.12	1.111	293.18
5	2000	4.14	0.00	2004.4	4.095	0.026	39.06	1.632	1.32
6	2000	4.14	0.27	2004.1	4.114	0.269	37.61	0.531	152.04
7	2000	4.14	0.53	2004.1	4.105	0.541	40.54	0.751	253.46
8	2000	4.14	0.8	2003.3	3.893	0.798	40.85	1.017	409.38
9	2000	6.21	0.00	2004.4	6.022	0.027	52.45	2.801	5.22
10	2000	6.21	0.27	2004.7	6.112	0.261	50.84	0.789	144.64
11	2000	6.21	0.53	2002.9	6.056	0.525	50.93	0.788	305.40
12	2000	6.21	0.8	2004.4	6.267	0.797	55.04	1.009	610.80
13	2000	8.27	0.00	2003.6	8.045	0.086	61.49	-2.556	30.13
14	2000	8.27	0.27	2004.3	8.222	0.271	61.32	1.468	194.74
15	2000	8.27	0.53	2004.4	8.079	0.531	61.47	0.957	439.56
16	2000	8.27	0.8	2004.5	8.158	0.784	65.20	0.969	749.59
17	4000	2.07	0.00	3998.7	1.969	0.022	13.92	1.277	27.61
18	4000	2.07	0.27	3999.4	1.884	0.269	13.95	1.262	96.80
19	4000	2.07	0.53	4000.0	1.979	0.533	15.42	1.320	211.69
20	4000	2.07	0.8	3999.6	1.887	0.794	17.04	1.389	476.97
21	4000	4.14	0.00	4004.7	4.053	0.042	35.88	-1.742	13.39
22	4000	4.14	0.27	4000.2	4.106	0.277	34.34	1.425	139.68
23	4000	4.14	0.53	3999.5	3.999	0.536	34.46	1.164	283.52
24	4000	4.14	0.8	4003.4	3.914	0.786	36.28	1.301	647.70
25	4000	6.21	0.00	4009.6	6.040	0.087	47.31	-2.243	43.81
26	4000	6.21	0.27	4000.3	6.050	0.278	47.00	1.257	185.03
27	4000	6.21	0.53	4000.0	6.022	0.539	47.07	1.006	377.88
28	4000	6.21	0.8	4009.6	6.125	0.815	51.54	1.225	782.45
29	4000	8.27	0.00	4001.5	8.148	0.057	57.49	2.143	2.61
30	4000	8.27	0.27	4002.0	8.019	0.280	57.84	1.600	163.58
31	4000	8.27	0.53	4001.7	8.333	0.534	59.61	1.129	406.03
32	4000	8.27	0.8	4009.9	8.006	0.827	62.18	1.188	970.04

Table A. 7. Static results for the medium pre-swirl insert. (Continued)

Test Point	Target			Measured					
	ω [rpm]	ΔP [bar]	ϵ_0 [-]	ω [rpm]	ΔP [bar]	ϵ_0 [-]	$\dot{Q}$ [LPM]	ϕ [rad]	F_r [N]
33	6000	2.07	0.00	6016.9	2.108	0.031	12.41	-2.275	47.25
34	6000	2.07	0.27	6016.0	1.947	0.286	11.07	1.596	226.78
35	6000	2.07	0.53	6016.5	1.950	0.530	12.55	1.632	415.44
36	6000	2.07	0.8	5999.3	1.897	0.794	15.02	1.424	883.90
37	6000	4.14	0.00	6016.2	3.912	0.045	23.89	-0.127	43.11
38	6000	4.14	0.27	6016.3	4.061	0.279	25.52	1.340	214.90
39	6000	4.14	0.53	6014.0	4.194	0.544	28.37	1.364	424.79
40	6000	4.14	0.8	5999.2	4.181	0.784	32.66	1.383	924.15
41	6000	6.21	0.00	6007.6	6.009	0.029	36.76	-0.045	4.45
42	6000	6.21	0.27	6010.4	6.151	0.282	38.45	1.312	262.07
43	6000	6.21	0.53	6015.9	6.072	0.524	41.04	1.289	466.18
44	6000	6.21	0.8	5998.9	6.270	0.820	47.15	1.307	1161.84
45	6000	8.27	0.00	6005.5	8.296	0.042	49.86	-0.141	2.39
46	6000	8.27	0.27	6004.8	8.228	0.274	50.01	1.272	210.04
47	6000	8.27	0.53	5999.2	8.294	0.446	53.42	1.201	506.53
48	6000	8.27	0.8	5998.2	8.203	0.785	57.39	1.238	1136.70
49	8000	2.07	0.00	8001.7	1.954	0.042	9.73	-1.610	3.96
50	8000	2.07	0.27	8002.6	1.864	0.277	9.76	1.667	298.49
51	8000	2.07	0.53	8005.6	1.988	0.536	11.83	1.598	724.65
52	8000	2.07	0.8	8002.7	1.892	0.799	13.55	1.373	1287.88
53	8000	4.14	0.00	8003.8	3.892	0.062	20.27	1.030	19.39
54	8000	4.14	0.27	8002.4	3.776	0.276	20.34	1.415	223.15
55	8000	4.14	0.53	8008.7	3.974	0.521	24.82	1.515	747.84
56	8000	4.14	0.8	8002.9	4.081	0.793	28.09	1.479	1386.71
57	8000	6.21	0.00	8001.5	5.988	0.027	33.35	1.923	5.14
58	8000	6.21	0.27	8001.5	6.002	0.276	33.24	1.372	258.00
59	8000	6.21	0.53	8012.0	5.930	0.545	35.41	1.434	791.79
60	8000	6.21	0.8	8002.7	6.071	0.792	41.14	1.440	1413.38
61	8000	8.27	0.00	8001.9	7.966	0.046	42.30	1.593	4.23
62	8000	8.27	0.27	8000.8	8.194	0.270	44.13	1.208	253.43
63	8000	8.27	0.53	8002.0	8.142	0.540	47.20	1.271	830.94
64	8000	8.27	0.8	8002.3	8.196	0.811	54.14	1.352	1604.90

Table A. 8. Flow results for the medium pre-swirl insert.

Test Point	Pre-swirl Ratio [-]	Post-swirl Ratio [-]	Inlet Temp. [°C]	Outlet Temp. [°C]	Re_z [-]	Re_θ [-]	Re_t [-]
1	0.328	0.251	44.709	44.648	844.2	826.6	1181.5
2	0.325	0.291	47.484	49.804	979.2	873.2	1312.0
3	0.291	0.302	46.481	45.189	963.7	857.6	1290.1
4	0.337	0.296	46.620	49.095	1186.6	860.0	1465.5
5	0.616	0.268	45.698	47.660	1745.8	846.6	1940.2
6	0.546	0.343	46.729	45.337	1712.2	862.1	1917.0
7	0.558	0.370	45.985	48.139	1821.0	850.7	2010.0
8	0.544	0.399	44.411	43.934	1785.6	827.4	1968.0
9	0.938	0.318	46.397	48.288	2373.3	857.1	2523.4
10	0.879	0.326	46.638	45.825	2310.7	860.9	2465.9
11	1.012	0.373	45.498	45.240	2268.4	843.0	2420.0
12	0.767	0.332	47.101	46.737	2522.5	863.4	2666.2
13	1.053	0.309	45.668	47.295	2746.9	845.8	2874.2
14	1.050	0.310	47.135	46.892	2812.1	868.5	2943.1
15	1.022	0.369	45.533	46.982	2739.5	844.1	2866.6
16	0.920	0.404	46.697	48.452	2966.3	857.2	3087.7
17	0.279	0.303	44.992	45.455	614.7	1668.2	1777.8
18	0.270	0.268	46.314	48.210	630.1	1707.7	1820.2
19	0.268	0.249	47.237	47.021	708.2	1736.4	1875.3
20	0.259	0.262	45.594	45.644	760.3	1686.2	1849.7
21	0.344	0.266	45.884	47.636	1609.1	1687.9	2332.0
22	0.326	0.242	46.928	46.922	1568.9	1726.9	2333.2
23	0.309	0.246	45.362	46.762	1531.0	1679.3	2272.4
24	0.311	0.238	45.499	46.151	1616.1	1676.0	2328.2
25	0.421	0.271	47.555	49.602	2186.3	1741.4	2795.0
26	0.395	0.255	46.733	46.775	2139.6	1720.9	2745.8
27	0.376	0.294	45.751	45.987	2105.9	1691.0	2700.8
28	0.381	0.298	47.508	47.384	2379.6	1739.9	2947.8
29	0.497	0.255	47.333	47.187	2645.6	1740.2	3166.6
30	0.484	0.262	45.835	46.406	2591.5	1694.3	3096.2
31	0.461	0.257	47.845	48.187	2768.8	1756.6	3279.0
32	0.454	0.236	47.190	46.942	2854.2	1730.0	3337.6

Table A. 8. Flow results for the medium pre-swirl insert. (Continued)

Test Point	Pre-swirl Ratio [-]	Post-swirl Ratio [-]	Inlet Temp. [°C]	Outlet Temp. [°C]	Re_z [-]	Re_θ [-]	Re_t [-]
33	0.328	0.178	46.796	49.910	565.5	2591.3	2652.3
34	0.328	0.280	47.110	48.717	507.4	2605.7	2654.6
35	0.311	0.325	46.020	47.496	564.1	2555.6	2617.1
36	0.292	0.255	46.185	47.890	677.0	2542.1	2630.7
37	0.275	0.289	45.509	46.869	1064.1	2532.6	2747.0
38	0.265	0.280	45.686	47.011	1140.3	2540.5	2784.7
39	0.264	0.253	49.121	49.039	1349.5	2703.2	3021.4
40	0.264	0.260	47.568	48.015	1509.4	2606.1	3011.7
41	0.295	0.255	45.995	46.739	1651.8	2550.7	3038.8
42	0.291	0.257	46.677	47.251	1748.5	2583.0	3119.2
43	0.288	0.262	45.536	47.095	1828.9	2533.6	3124.8
44	0.291	0.242	47.673	48.266	2183.4	2611.0	3403.6
45	0.332	0.252	46.915	49.083	2277.5	2592.0	3450.4
46	0.322	0.244	45.193	45.894	2215.6	2513.8	3350.9
47	0.323	0.258	47.497	49.898	2465.6	2602.7	3585.2
48	0.322	0.244	46.332	46.697	2593.9	2548.2	3636.2
49	0.379	0.113	46.360	50.710	440.2	3419.4	3447.6
50	0.366	0.078	45.920	50.114	437.9	3393.2	3421.3
51	0.356	0.321	46.294	49.955	534.5	3398.8	3440.6
52	0.323	0.280	46.398	50.235	613.2	3403.9	3458.7
53	0.304	0.346	47.225	48.990	931.0	3473.8	3596.4
54	0.298	0.398	46.062	48.327	915.2	3401.6	3522.6
55	0.278	0.319	45.744	49.570	1110.2	3367.2	3545.5
56	0.268	0.236	47.374	48.697	1293.6	3464.3	3697.9
57	0.271	0.283	47.430	51.324	1537.6	3485.8	3809.8
58	0.267	0.274	45.331	47.467	1476.2	3357.8	3668.0
59	0.261	0.242	47.297	48.790	1628.5	3463.4	3827.1
60	0.262	0.237	46.129	47.628	1852.8	3387.7	3861.2
61	0.278	0.274	47.131	48.211	1939.7	3467.1	3972.8
62	0.277	0.263	45.775	47.166	1975.1	3383.8	3918.0
63	0.273	0.268	46.066	47.687	2123.3	3383.6	3994.6
64	0.274	0.255	47.680	51.131	2507.2	3483.4	4291.9

Table A. 9. Stiffness coefficients and uncertainties for the medium pre-swirl insert.

Test Point	K_{xx} [MN/m]	$U_{K_{xx}}$ [MN/m]	K_{xy} [MN/m]	$U_{K_{xy}}$ [MN/m]	K_{yx} [MN/m]	$U_{K_{yx}}$ [MN/m]	K_{yy} [MN/m]	$U_{K_{yy}}$ [MN/m]
1	0.67	0.09	0.67	0.08	-0.71	0.05	0.74	0.11
2	0.61	0.12	0.84	0.05	-0.71	0.08	0.70	0.16
3	-0.04	0.29	1.48	0.13	-1.04	0.14	0.61	0.20
4	-1.98	2.86	3.31	1.08	-6.12	0.90	2.21	0.63
5	2.76	0.17	1.34	0.13	-1.42	0.12	2.82	0.18
6	2.03	0.15	1.61	0.08	-1.11	0.12	1.93	0.24
7	0.80	0.30	2.33	0.15	-1.48	0.20	1.25	0.25
8	-1.75	2.14	4.27	0.86	-5.56	0.72	2.77	0.76
9	0.33	0.18	2.42	0.21	-2.82	0.24	-0.15	0.20
10	2.04	0.17	2.06	0.19	-2.41	0.13	2.05	0.22
11	1.74	0.24	2.44	0.15	-2.32	0.18	2.18	0.25
12	-0.50	4.17	5.31	1.23	-8.53	2.64	5.53	2.87
13	-0.09	0.40	2.26	0.23	-3.85	0.21	0.47	0.31
14	4.24	0.18	2.71	0.11	-3.23	0.15	1.13	0.13
15	3.02	0.22	2.65	0.18	-3.52	0.12	3.15	0.17
16	-0.27	2.72	6.38	0.63	-6.95	2.00	4.80	2.61
17	-0.20	0.07	1.44	0.11	-1.51	0.05	-0.04	0.07
18	-0.28	0.16	1.55	0.11	-1.64	0.05	0.00	0.06
19	-0.14	0.52	1.94	0.15	-2.69	0.12	0.32	0.07
20	0.76	3.08	3.30	0.47	-10.27	0.54	1.15	0.26
21	-1.44	0.41	2.61	0.26	-3.30	0.64	-3.02	0.90
22	1.18	0.11	2.46	0.07	-2.47	0.18	0.11	0.10
23	0.74	0.48	2.57	0.17	-3.48	0.21	1.07	0.18
24	-0.94	3.91	4.65	0.64	-13.20	2.03	4.30	2.73
25	-1.37	0.17	2.78	0.19	-3.52	0.88	-1.04	0.62
26	2.22	0.17	2.59	0.12	-3.45	0.17	-0.04	0.10
27	1.64	0.36	2.83	0.15	-3.86	0.14	1.97	0.12
28	-1.70	3.77	7.01	0.74	-17.25	1.72	5.84	1.95
29	-0.31	0.23	3.62	0.16	-3.49	0.25	-0.33	0.20
30	2.97	0.32	4.23	0.20	-3.10	0.20	0.32	0.17
31	3.36	0.27	3.18	0.17	-4.76	0.15	2.67	0.16
32	-2.01	3.71	8.29	0.94	-17.61	2.14	6.18	0.63

Table A. 9. Stiffness coefficients and uncertainties for the medium pre-swirl insert. (Continued)

Test Point	K_{xx} [MN/m]	$U_{K_{xx}}$ [MN/m]	K_{xy} [MN/m]	$U_{K_{xy}}$ [MN/m]	K_{yx} [MN/m]	$U_{K_{yx}}$ [MN/m]	K_{yy} [MN/m]	$U_{K_{yy}}$ [MN/m]
33	-0.31	0.08	2.96	0.07	-2.95	0.05	-0.21	0.06
34	-0.37	0.17	3.06	0.11	-3.37	0.06	-0.42	0.05
35	-0.15	0.55	3.72	0.25	-5.24	0.19	-0.57	0.08
36	5.60	5.16	5.75	0.71	-18.25	2.86	2.14	3.73
37	0.32	0.21	3.34	0.12	-3.25	0.14	0.42	0.11
38	0.20	0.17	3.65	0.19	-3.80	0.12	0.41	0.15
39	-0.65	0.57	4.18	0.23	-5.33	0.17	0.36	0.27
40	1.77	5.34	7.60	0.97	-22.66	3.89	3.20	4.44
41	1.60	0.10	3.33	0.07	-3.44	0.14	1.76	0.13
42	1.33	0.08	3.57	0.10	-3.77	0.12	1.76	0.11
43	-0.15	0.57	4.48	0.26	-5.00	0.16	1.52	0.17
44	-0.34	6.14	8.37	1.02	-25.57	3.86	6.11	2.28
45	2.97	0.08	4.05	0.30	-4.11	0.26	3.17	0.04
46	0.78	0.29	4.28	0.18	-4.25	0.19	2.75	0.10
47	1.69	0.42	5.24	0.18	-6.58	0.96	2.31	2.21
48	-1.36	4.29	8.76	1.01	-20.74	3.03	5.99	2.04
49	-1.02	0.13	4.56	0.11	-4.60	0.05	-0.88	0.07
50	-0.96	0.21	4.84	0.14	-5.20	0.10	-1.04	0.05
51	-0.38	0.56	6.14	0.42	-10.50	1.53	0.67	4.26
52	17.49	3.84	5.54	0.73	-25.26	2.87	5.13	1.22
53	-0.22	0.14	4.56	0.16	-4.72	0.09	-0.16	0.12
54	-0.44	0.24	5.01	0.17	-5.39	0.08	-0.17	0.13
55	-0.47	0.52	6.36	0.35	-9.89	1.13	0.43	2.56
56	9.14	3.79	9.17	0.74	-24.84	2.76	1.04	0.94
57	0.58	0.27	5.46	0.34	-5.49	0.30	0.63	0.32
58	0.34	0.25	5.92	0.40	-6.17	0.25	0.55	0.32
59	-0.55	0.42	6.66	0.50	-10.62	1.25	1.36	2.11
60	5.06	4.32	9.77	0.80	-28.61	3.40	2.84	1.08
61	1.90	0.09	5.25	0.14	-5.36	0.16	2.05	0.06
62	1.68	0.16	5.60	0.13	-5.77	0.08	2.23	0.12
63	0.03	0.43	7.02	0.39	-10.22	1.23	3.33	1.99
64	2.39	4.31	10.71	0.76	-31.47	2.66	5.49	1.78

Table A. 10. Damping coefficients and uncertainties for the medium pre-swirl insert.

Test Point	C_{xx} [kN-s/m]	$U_{C_{xx}}$ [kN-s/m]	C_{xy} [kN-s/m]	$U_{C_{xy}}$ [kN-s/m]	C_{yx} [kN-s/m]	$U_{C_{yx}}$ [kN-s/m]	C_{yy} [kN-s/m]	$U_{C_{yy}}$ [kN-s/m]
1	6.60	0.59	2.41	0.13	-2.27	0.15	6.87	0.55
2	6.97	0.58	2.13	0.06	-2.64	0.21	7.72	0.62
3	11.41	0.97	-0.50	0.23	-5.86	0.36	12.45	0.72
4	61.52	8.02	-20.74	2.82	-27.36	2.37	28.44	1.79
5	9.28	0.39	3.18	0.30	-2.81	0.20	9.55	0.39
6	9.79	0.36	2.61	0.10	-2.98	0.26	10.78	0.45
7	13.76	0.70	0.77	0.20	-5.15	0.46	15.43	0.62
8	57.20	6.47	-21.39	2.84	-28.55	2.64	35.04	1.90
9	14.81	0.56	3.28	0.46	-2.55	0.65	15.38	0.66
10	12.98	0.35	3.67	0.45	-2.80	0.44	13.64	0.28
11	15.18	0.77	2.20	0.22	-4.78	0.51	16.39	0.61
12	69.34	10.95	-23.95	4.67	-32.19	4.18	40.82	2.52
13	16.81	1.07	4.31	0.57	-3.06	0.83	17.02	0.57
14	14.33	0.33	4.32	0.27	-3.58	0.49	16.38	0.43
15	16.99	0.87	3.11	0.22	-5.03	0.43	17.61	0.47
16	53.84	8.18	-16.03	3.41	-24.53	5.52	36.97	6.23
17	6.53	0.71	4.32	0.18	-4.11	0.10	6.57	0.63
18	7.51	0.71	4.21	0.16	-4.38	0.20	7.12	0.63
19	12.56	1.35	3.26	0.20	-6.07	0.38	8.71	0.72
20	54.43	5.89	-1.71	0.90	-13.01	1.84	17.36	0.69
21	12.89	1.25	4.49	0.74	-1.78	2.76	13.01	4.24
22	10.13	0.65	4.17	0.15	-4.62	0.27	11.42	0.71
23	13.76	1.27	3.28	0.22	-6.65	0.37	13.11	0.68
24	54.70	11.73	-5.61	2.38	-18.33	3.16	22.80	1.72
25	15.25	0.41	4.49	0.67	-4.14	1.53	14.67	2.86
26	12.83	0.40	5.05	0.19	-4.32	0.45	14.30	0.46
27	15.37	0.59	3.86	0.19	-6.90	0.36	16.30	0.37
28	75.13	12.43	-13.86	2.67	-26.90	3.86	31.38	3.41
29	15.75	0.41	5.18	0.49	-4.67	0.59	16.21	0.43
30	15.49	0.66	5.47	0.42	-4.75	0.61	16.48	0.44
31	16.77	1.02	4.87	0.33	-6.86	0.38	17.43	0.43
32	74.97	11.89	-15.48	3.04	-29.01	4.90	35.42	3.49

Table A. 10. Damping coefficients and uncertainties for the medium pre-swirl insert. (Continued)

Test Point	C_{xx} [kN-s/m]	$U_{C_{xx}}$ [kN-s/m]	C_{xy} [kN-s/m]	$U_{C_{xy}}$ [kN-s/m]	C_{yx} [kN-s/m]	$U_{C_{yx}}$ [kN-s/m]	C_{yy} [kN-s/m]	$U_{C_{yy}}$ [kN-s/m]
33	8.39	0.70	6.34	0.18	-6.37	0.10	8.64	0.74
34	9.52	0.96	6.76	0.17	-6.33	0.21	8.93	0.69
35	15.49	1.58	7.24	0.30	-7.13	0.59	10.68	0.76
36	48.72	8.83	0.58	2.00	-14.17	5.57	17.70	4.25
37	10.44	0.95	5.94	0.35	-5.93	0.29	10.55	0.82
38	11.85	0.96	5.61	0.30	-6.25	0.21	11.47	0.96
39	17.85	0.60	5.59	0.36	-8.25	0.55	14.38	0.40
40	58.50	11.80	1.07	2.28	-17.21	7.53	20.63	3.66
41	11.81	0.37	7.02	0.17	-6.63	0.24	11.83	0.46
42	12.20	0.77	7.03	0.16	-6.94	0.23	12.21	0.50
43	16.21	1.20	7.01	0.35	-8.54	0.57	13.87	0.53
44	62.24	14.35	-4.20	3.10	-25.00	9.89	30.15	6.14
45	13.66	0.53	7.00	0.42	-6.45	0.46	13.74	0.48
46	14.99	1.42	7.02	0.40	-6.74	0.45	14.24	0.47
47	17.77	1.86	7.44	0.48	-8.42	1.01	16.15	1.96
48	50.79	11.88	-2.70	2.86	-24.42	8.22	32.42	7.39
49	9.60	0.66	8.71	0.23	-8.53	0.11	9.63	0.76
50	10.89	1.06	9.17	0.22	-8.43	0.40	10.26	0.77
51	19.78	2.32	9.15	0.73	-9.88	1.27	13.02	2.81
52	46.81	5.22	-4.79	2.08	-26.59	3.40	24.84	1.53
53	10.71	0.73	8.44	0.37	-8.19	0.23	11.00	0.73
54	12.44	0.75	8.28	0.36	-8.51	0.44	11.83	0.71
55	20.28	2.09	8.54	0.67	-9.10	1.61	14.50	4.20
56	51.41	6.92	3.80	2.08	-17.51	3.74	21.80	2.37
57	14.33	0.22	7.68	0.60	-7.52	0.59	14.81	0.34
58	15.54	0.40	7.37	0.66	-7.77	0.40	15.24	0.49
59	23.25	1.96	8.33	1.02	-10.54	2.24	16.45	4.88
60	56.16	9.01	5.22	2.42	-21.21	6.13	24.66	2.26
61	14.06	0.28	9.50	0.23	-8.85	0.37	14.29	0.32
62	15.14	0.43	9.21	0.28	-9.46	0.40	15.01	0.29
63	22.09	1.81	8.29	0.67	-12.49	1.88	17.17	4.66
64	61.98	10.55	1.32	2.53	-28.34	10.02	32.94	8.26

Table A. 11. Virtual mass coefficients and uncertainties for the medium pre-swirl insert.

Test Point	M_{xx} [kg]	$U_{M_{xx}}$ [kg]	M_{xy} [kg]	$U_{M_{xy}}$ [kg]	M_{yx} [kg]	$U_{M_{yx}}$ [kg]	M_{yy} [kg]	$U_{M_{yy}}$ [kg]
1	14.56	0.13	0.37	0.11	0.14	0.07	14.49	0.15
2	15.00	0.16	0.17	0.07	-0.09	0.11	14.89	0.22
3	16.99	0.43	-0.59	0.20	-0.96	0.21	16.66	0.30
4	31.60	3.90	-4.72	1.47	-5.30	1.23	20.75	0.86
5	16.47	0.23	0.43	0.18	-0.06	0.16	16.31	0.24
6	16.34	0.21	0.26	0.12	-0.03	0.17	16.36	0.33
7	17.96	0.41	-0.77	0.21	-1.20	0.27	17.83	0.34
8	29.36	2.91	-5.02	1.18	-5.24	0.99	22.47	1.03
9	15.14	0.24	0.29	0.28	0.03	0.33	14.77	0.27
10	16.78	0.23	-0.28	0.26	-0.03	0.17	16.59	0.29
11	18.79	0.32	-0.89	0.21	-1.02	0.25	18.20	0.34
12	39.29	8.98	-7.58	2.65	-14.37	5.67	35.50	6.17
13	16.27	0.54	-0.45	0.31	0.55	0.29	16.40	0.42
14	18.24	0.25	-0.07	0.14	0.24	0.20	16.61	0.17
15	19.77	0.31	-0.70	0.25	-0.90	0.16	18.54	0.24
16	31.96	5.86	-4.69	1.35	-10.73	4.31	30.95	5.61
17	12.82	0.10	0.55	0.15	-0.28	0.07	12.89	0.10
18	13.23	0.24	0.49	0.16	-0.25	0.07	12.91	0.09
19	15.40	0.77	0.51	0.23	-0.59	0.17	13.73	0.11
20	26.36	4.62	-1.37	0.71	-1.56	0.81	15.56	0.40
21	14.40	0.86	0.26	0.54	-0.56	1.35	10.75	1.88
22	16.11	0.15	0.90	0.09	-0.48	0.25	14.88	0.13
23	18.50	0.65	0.09	0.22	-1.33	0.29	16.28	0.25
24	34.00	8.42	-1.15	1.37	-10.83	4.37	29.60	5.87
25	15.61	0.35	-0.04	0.39	-0.94	1.84	14.84	1.30
26	16.69	0.24	0.44	0.17	-0.36	0.24	15.74	0.13
27	18.77	0.54	-0.48	0.22	-0.79	0.21	17.54	0.19
28	35.43	7.96	-2.35	1.55	-10.58	3.63	24.46	4.11
29	16.88	0.31	0.03	0.22	0.42	0.34	16.60	0.27
30	17.55	0.44	0.53	0.27	-0.15	0.28	16.16	0.23
31	19.60	0.37	-0.25	0.23	-0.95	0.21	17.88	0.22
32	35.21	7.83	-2.37	1.99	-12.75	4.53	24.31	1.33

Table A. 11. Virtual mass coefficients and uncertainties for the medium pre-swirl insert. (Continued)

Test Point	M_{xx} [kg]	$U_{M_{xx}}$ [kg]	M_{xy} [kg]	$U_{M_{xy}}$ [kg]	M_{yx} [kg]	$U_{M_{yx}}$ [kg]	M_{yy} [kg]	$U_{M_{yy}}$ [kg]
33	13.13	0.11	0.94	0.10	-0.66	0.07	12.85	0.08
34	13.63	0.25	1.19	0.17	-0.59	0.09	13.07	0.07
35	16.54	0.83	1.81	0.38	-0.21	0.29	13.80	0.12
36	28.58	10.90	-0.38	1.50	-14.49	6.04	21.24	7.88
37	12.68	0.28	1.29	0.16	-0.72	0.18	12.53	0.14
38	13.42	0.23	1.46	0.27	-1.06	0.17	12.64	0.21
39	17.53	0.86	0.21	0.35	-0.39	0.25	15.05	0.41
40	32.13	11.28	0.98	2.05	-20.13	8.22	29.66	9.38
41	16.17	0.13	0.43	0.10	-0.52	0.19	16.18	0.18
42	16.71	0.11	0.52	0.13	-0.70	0.17	16.42	0.15
43	19.40	0.85	0.03	0.39	-1.28	0.23	17.33	0.25
44	30.40	12.96	1.31	2.15	-23.01	8.14	32.85	4.81
45	16.93	0.11	0.96	0.41	-0.78	0.36	16.94	0.05
46	16.39	0.44	0.55	0.27	-0.36	0.28	17.11	0.16
47	19.11	0.89	0.26	0.37	-7.53	2.04	24.01	4.67
48	26.71	9.06	0.63	2.13	-18.42	6.40	31.33	4.31
49	13.32	0.17	1.19	0.15	-0.97	0.07	13.05	0.09
50	13.85	0.32	1.67	0.21	-0.91	0.15	13.26	0.08
51	17.94	1.20	2.83	0.91	-8.01	3.30	25.37	9.17
52	32.51	8.26	-4.73	1.56	-18.05	6.18	18.43	2.62
53	13.17	0.19	1.07	0.22	-1.09	0.12	13.09	0.17
54	13.59	0.36	1.44	0.26	-1.09	0.12	13.35	0.19
55	17.34	1.13	2.19	0.74	-6.15	2.42	18.52	5.51
56	31.94	8.01	1.07	1.56	-13.95	5.82	14.44	1.98
57	14.14	0.37	0.77	0.47	-0.64	0.42	13.89	0.44
58	13.86	0.38	1.63	0.60	-1.25	0.37	13.20	0.48
59	19.34	0.90	-0.08	1.07	-4.87	2.69	21.49	4.55
60	33.73	9.12	1.42	1.69	-15.92	7.18	22.30	2.29
61	16.92	0.12	0.18	0.19	-0.15	0.22	16.91	0.09
62	17.27	0.24	0.22	0.20	-0.06	0.12	17.22	0.17
63	20.41	0.92	0.00	0.84	-5.76	2.65	23.73	4.27
64	31.46	9.10	1.38	1.61	-17.21	5.62	24.81	3.77

Table A. 12. Whirl frequency ratio, effective damping, and uncertainties for the medium pre-swirl insert.

Test Point	Target			Measured			
	ω [rpm]	ΔP [bar]	ε ϵ_0	WFR [-]	U_{WFR} [-]	C_{eff} [kN-s/m]	$U_{C_{eff}}$ [kN-s/m]
1	2000	2.07	0.00	0.49	0.04	3.49	0.26
2	2000	2.07	0.27	0.50	0.04	3.70	0.27
3	2000	2.07	0.53	0.50	0.05	6.08	0.20
4	2000	2.07	0.8	0.55	0.17	23.54	0.17
5	2000	4.14	0.00	0.70	0.05	2.87	-0.21
6	2000	4.14	0.27	0.62	0.04	3.84	-0.09
7	2000	4.14	0.53	0.61	0.05	5.72	-0.17
8	2000	4.14	0.8	0.56	0.12	23.77	0.41
9	2000	6.21	0.00	0.82	0.06	2.65	-0.45
10	2000	6.21	0.27	0.80	0.04	2.68	-0.45
11	2000	6.21	0.53	0.72	0.04	4.64	-0.11
12	2000	6.21	0.8	0.63	0.21	24.40	-2.47
13	2000	8.27	0.00	0.83	0.06	2.45	-0.22
14	2000	8.27	0.27	0.80	0.04	1.25	-0.23
15	2000	8.27	0.53	0.84	0.04	2.75	-0.05
16	2000	8.27	0.8	0.74	0.19	15.27	0.93
17	4000	2.07	0.00	0.54	0.05	3.20	0.47
18	4000	2.07	0.27	0.52	0.04	3.67	0.49
19	4000	2.07	0.53	0.52	0.04	5.34	0.71
20	4000	2.07	0.8	0.46	0.04	20.31	2.08
21	4000	4.14	0.00	0.53	0.11	6.07	1.67
22	4000	4.14	0.27	0.54	0.03	5.18	0.38
23	4000	4.14	0.53	0.53	0.04	6.51	0.52
24	4000	4.14	0.8	0.53	0.10	19.97	3.55
25	4000	6.21	0.00	0.50	0.08	7.66	0.37
26	4000	6.21	0.27	0.50	0.02	6.51	0.07
27	4000	6.21	0.53	0.50	0.02	8.12	0.14
28	4000	6.21	0.8	0.55	0.09	27.09	5.00
29	4000	8.27	0.00	0.53	0.02	7.59	-0.07
30	4000	8.27	0.27	0.51	0.03	7.39	0.07
31	4000	8.27	0.53	0.54	0.02	7.88	0.34
32	4000	8.27	0.8	0.58	0.09	27.53	4.02

Table A. 12. Whirl frequency ratio, effective damping, and uncertainties for the medium pre-swirl insert. (Continued)

Test Point	Target			Measured			
	ω [rpm]	ΔP [bar]	ε ϵ_0 [ ]	WFR [-]	U_{WFR} [-]	C_{eff} [kN-s/m]	$U_{C_{eff}}$ [kN-s/m]
33	6000	2.07	0.00	0.55	0.03	4.33	0.62
34	6000	2.07	0.27	0.55	0.04	4.69	0.69
35	6000	2.07	0.53	0.54	0.04	6.61	0.81
36	6000	2.07	0.8	0.55	0.10	18.78	3.70
37	6000	4.14	0.00	0.50	0.03	5.90	0.68
38	6000	4.14	0.27	0.51	0.03	6.54	0.71
39	6000	4.14	0.53	0.47	0.02	8.75	0.19
40	6000	4.14	0.8	0.60	0.10	22.11	3.86
41	6000	6.21	0.00	0.46	0.02	6.73	0.24
42	6000	6.21	0.27	0.48	0.02	6.76	0.46
43	6000	6.21	0.53	0.50	0.03	7.93	0.53
44	6000	6.21	0.8	0.55	0.11	26.82	6.36
45	6000	8.27	0.00	0.47	0.03	7.76	0.06
46	6000	8.27	0.27	0.46	0.03	8.12	0.65
47	6000	8.27	0.53	0.55	0.06	9.99	1.00
48	6000	8.27	0.8	0.53	0.11	24.10	6.42
49	8000	2.07	0.00	0.57	0.03	5.05	0.61
50	8000	2.07	0.27	0.57	0.04	5.66	0.77
51	8000	2.07	0.53	0.60	0.09	11.02	1.39
52	8000	2.07	0.8	0.38	0.07	27.00	1.23
53	8000	4.14	0.00	0.51	0.03	6.22	0.58
54	8000	4.14	0.27	0.51	0.02	6.99	0.58
55	8000	4.14	0.53	0.55	0.09	11.20	2.27
56	8000	4.14	0.8	0.51	0.06	22.60	2.55
57	8000	6.21	0.00	0.45	0.02	8.62	-0.11
58	8000	6.21	0.27	0.47	0.02	9.39	0.06
59	8000	6.21	0.53	0.51	0.09	11.63	2.38
60	8000	6.21	0.8	0.53	0.06	24.78	3.13
61	8000	8.27	0.00	0.45	0.01	7.97	0.12
62	8000	8.27	0.27	0.45	0.01	8.41	0.23
63	8000	8.27	0.53	0.52	0.08	11.76	2.27
64	8000	8.27	0.8	0.49	0.08	30.09	7.36

A.3 High Pre-swirl Insert Assembly

Table A. 13. Static results for the high pre-swirl insert.

Test Point	Target			Measured					
	ω [rpm]	ΔP [bar]	ϵ_0 [-]	ω [rpm]	ΔP [bar]	ϵ_0 [-]	$\dot{Q}$ [LPM]	ϕ [rad]	F_r [N]
1	2000	2.07	0.00	2001.6	2.155	0.029	23.09	-0.018	11.95
2	2000	2.07	0.27	2002.4	1.925	0.287	23.25	0.468	101.61
3	2000	2.07	0.53	2003.4	2.257	0.522	26.89	0.680	190.70
4	2000	2.07	0.8	2003.7	1.852	0.802	27.25	1.064	320.44
5	2000	4.14	0.00	2004.3	4.185	0.020	39.17	0.459	7.47
6	2000	4.14	0.27	2004.5	4.101	0.285	38.85	0.664	156.18
7	2000	4.14	0.53	2003.9	4.048	0.532	39.63	0.828	265.61
8	2000	4.14	0.8	2004.3	4.168	0.795	41.83	1.055	457.77
9	2000	6.21	0.00	2004.4	6.221	0.024	50.48	0.441	-0.04
10	2000	6.21	0.27	2004.4	6.120	0.281	49.49	0.985	163.69
11	2000	6.21	0.53	2004.5	6.430	0.520	50.55	0.893	361.09
12	2000	6.21	0.8	2001.6	6.053	0.820	50.32	1.049	829.82
13	2000	8.27	0.00	2004.6	8.093	0.026	57.47	0.989	5.00
14	2000	8.27	0.27	2005.1	8.201	0.277	58.01	1.097	193.29
15	2000	8.27	0.53	2005.2	8.156	0.524	59.12	0.920	458.10
16	2000	8.27	0.8	2002.7	8.196	0.801	59.78	1.020	995.21
17	4000	2.07	0.00	4006.5	2.166	0.013	15.13	-1.766	3.72
18	4000	2.07	0.27	4005.8	2.112	0.269	15.20	1.269	86.43
19	4000	2.07	0.53	4005.3	1.936	0.527	16.79	1.292	205.77
20	4000	2.07	0.8	4004.3	2.180	0.789	19.25	1.364	453.36
21	4000	4.14	0.00	4004.7	4.133	0.024	35.02	1.139	86.64
22	4000	4.14	0.27	4005.0	4.045	0.274	32.51	1.663	250.28
23	4000	4.14	0.53	4004.8	4.122	0.529	34.26	1.313	394.75
24	4000	4.14	0.8	4002.7	4.089	0.779	36.22	1.192	714.12
25	4000	6.21	0.00	4004.4	6.282	0.029	46.40	-2.218	9.94
26	4000	6.21	0.27	4004.0	6.247	0.276	46.40	1.762	180.21
27	4000	6.21	0.53	4003.8	6.081	0.546	45.20	1.288	387.17
28	4000	6.21	0.8	4001.9	6.219	0.821	49.33	1.201	946.86
29	4000	8.27	0.00	4003.9	8.300	0.025	54.88	1.427	7.91
30	4000	8.27	0.27	4003.7	8.277	0.275	55.23	1.712	210.84
31	4000	8.27	0.53	4003.6	8.179	0.531	55.50	1.249	465.08
32	4000	8.27	0.8	4001.3	8.238	0.754	58.76	1.117	1007.98

Table A. 13. Static results for the high pre-swirl insert. (Continued)

Test Point	Target			Measured					
	ω [rpm]	ΔP [bar]	ϵ_0 [-]	ω [rpm]	ΔP [bar]	ϵ_0 [-]	$\dot{Q}$ [LPM]	ϕ [rad]	F_r [N]
33	6000	2.07	0.00	5999.5	2.019	0.038	11.26	3.109	5.39
34	6000	2.07	0.27	5999.2	1.965	0.268	12.06	1.600	166.78
35	6000	2.07	0.53	5998.5	2.057	0.532	12.76	1.628	366.90
36	6000	2.07	0.8	6000.5	2.009	0.784	14.74	1.411	849.99
37	6000	4.14	0.00	5998.7	3.965	0.027	24.06	2.200	8.18
38	6000	4.14	0.27	5998.0	4.128	0.278	25.08	1.351	169.63
39	6000	4.14	0.53	5999.4	4.108	0.525	27.05	1.371	367.87
40	6000	4.14	0.8	6000.9	3.929	0.812	30.99	1.370	1050.17
41	6000	6.21	0.00	6000.5	6.116	0.046	37.07	0.697	4.78
42	6000	6.21	0.27	5999.5	6.177	0.276	37.00	0.969	192.54
43	6000	6.21	0.53	5999.4	6.190	0.531	40.45	1.104	415.17
44	6000	6.21	0.8	6001.6	6.130	0.812	44.04	1.318	1171.60
45	6000	8.27	0.00	6000.1	8.229	0.026	46.85	-1.109	5.63
46	6000	8.27	0.27	6000.1	8.335	0.275	48.04	0.914	297.69
47	6000	8.27	0.53	6002.8	8.181	0.549	51.42	1.198	645.41
48	6000	8.27	0.8	6001.7	8.116	0.800	54.57	1.270	1267.13
49	8000	2.07	0.00	8014.7	1.977	0.034	9.92	1.983	2.53
50	8000	2.07	0.27	8006.8	2.100	0.274	10.40	1.305	248.99
51	8000	2.07	0.53	8008.6	2.077	0.495	11.00	1.629	485.49
52	8000	2.07	0.8	8010.7	2.091	0.807	13.31	1.374	1219.55
53	8000	4.14	0.00	8009.6	3.998	0.034	20.47	-2.661	2.41
54	8000	4.14	0.27	8006.4	3.940	0.281	21.32	1.530	279.20
55	8000	4.14	0.53	8007.4	4.118	0.521	23.48	1.556	501.73
56	8000	4.14	0.8	8011.8	4.028	0.789	26.86	1.464	1246.67
57	8000	6.21	0.00	8009.1	5.983	0.036	30.84	2.262	-0.53
58	8000	6.21	0.27	8004.1	6.092	0.277	32.49	1.379	239.32
59	8000	6.21	0.53	8006.4	6.298	0.519	35.58	1.442	537.08
60	8000	6.21	0.8	8007.1	6.209	0.797	39.74	1.435	1357.32
61	8000	8.27	0.00	8006.1	8.164	0.036	42.65	-1.842	1.85
62	8000	8.27	0.27	8006.2	8.215	0.267	42.57	1.251	238.38
63	8000	8.27	0.53	8006.2	8.383	0.541	45.81	1.321	653.22
64	8000	8.27	0.8	8006.4	8.458	0.813	52.23	1.362	1542.39

Table A. 14. Static flow results for the high pre-swirl insert.

Test Point	Pre-swirl Ratio [-]	Post-swirl Ratio [-]	Inlet Temp. [°C]	Outlet Temp. [°C]	Re_z [-]	Re_θ [-]	Re_t [-]
1	0.568	0.254	46.837	46.247	1053.0	872.4	1367.4
2	0.544	0.293	45.879	47.155	1042.3	858.0	1350.1
3	0.578	0.348	47.235	46.637	1235.2	879.5	1516.3
4	0.574	0.308	48.421	50.395	1279.2	899.0	1563.5
5	0.816	0.299	46.997	46.425	1791.7	876.1	1994.5
6	0.760	0.345	45.880	45.947	1741.9	858.9	1942.1
7	0.730	0.385	47.233	48.815	1820.5	879.7	2021.9
8	0.721	0.422	46.128	45.604	1883.8	862.6	2071.9
9	1.170	0.317	45.974	47.244	2267.3	860.3	2425.1
10	1.136	0.334	45.329	46.414	2197.8	850.6	2356.6
11	1.132	0.404	46.563	45.898	2294.4	869.4	2453.6
12	0.838	0.408	45.112	45.634	2226.3	844.5	2381.1
13	1.405	0.324	46.306	47.634	2596.2	865.5	2736.7
14	1.333	0.355	45.846	45.468	2599.7	858.7	2737.8
15	1.287	0.415	45.958	47.236	2654.6	860.4	2790.5
16	1.034	0.419	47.026	46.616	2735.7	874.1	2872.0
17	0.391	0.275	47.813	48.543	702.3	1786.1	1919.2
18	0.382	0.257	46.417	46.164	687.8	1741.3	1872.3
19	0.372	0.241	45.049	46.771	741.8	1699.7	1854.5
20	0.367	0.228	47.523	47.129	888.8	1775.7	1985.8
21	0.505	0.249	46.212	48.274	1579.7	1734.5	2346.0
22	0.476	0.259	47.199	46.693	1492.6	1765.6	2312.0
23	0.463	0.240	47.975	49.972	1595.4	1790.7	2398.3
24	0.460	0.249	48.056	49.704	1689.2	1780.2	2454.1
25	0.613	0.266	47.168	46.711	2129.0	1764.3	2765.1
26	0.608	0.245	47.275	48.636	2132.9	1767.6	2770.1
27	0.572	0.264	46.460	46.017	2047.5	1741.8	2688.1
28	0.583	0.337	46.866	47.355	2251.1	1741.7	2846.2
29	0.664	0.261	46.501	47.798	2487.8	1743.1	3037.7
30	0.661	0.252	45.553	45.223	2462.1	1714.0	2999.9
31	0.640	0.303	47.328	48.178	2553.6	1769.1	3106.6
32	0.632	0.289	46.578	48.567	2667.6	1732.5	3180.8

Table A. 14. Static flow results for the high pre-swirl insert. (Continued)

Test Point	Pre-swirl Ratio [-]	Post-swirl Ratio [-]	Inlet Temp. [°C]	Outlet Temp. [°C]	Re_z [-]	Re_θ [-]	Re_t [-]
33	0.403	0.162	45.627	47.957	502.7	2571.8	2620.5
34	0.393	0.311	46.898	50.352	550.4	2630.4	2687.4
35	0.377	0.320	47.626	48.626	590.3	2665.1	2729.7
36	0.359	0.244	46.233	47.441	665.2	2582.2	2666.5
37	0.384	0.275	46.817	48.721	1096.8	2626.4	2846.2
38	0.380	0.247	47.523	48.171	1158.0	2659.8	2901.0
39	0.374	0.239	46.377	47.336	1223.7	2606.1	2879.1
40	0.375	0.254	45.812	47.927	1387.9	2563.2	2914.8
41	0.431	0.244	47.945	50.802	1725.3	2681.5	3188.6
42	0.423	0.253	47.046	47.490	1693.9	2637.6	3134.7
43	0.423	0.260	47.339	49.610	1861.7	2651.6	3239.9
44	0.418	0.251	46.157	46.572	1984.2	2579.2	3254.1
45	0.467	0.251	47.158	47.310	2148.9	2643.2	3406.5
46	0.455	0.250	45.326	45.989	2133.3	2558.5	3331.3
47	0.463	0.250	47.753	49.823	2384.3	2655.0	3568.4
48	0.468	0.250	45.173	46.052	2416.6	2535.0	3502.3
49	0.427	0.118	49.009	54.472	471.0	3653.2	3683.5
50	0.422	0.168	47.672	50.727	481.7	3560.3	3592.7
51	0.399	0.284	46.921	50.290	502.4	3489.0	3525.0
52	0.382	0.253	45.742	48.388	595.5	3417.4	3468.9
53	0.385	0.288	46.704	48.467	931.4	3499.7	3621.5
54	0.374	0.403	47.088	50.846	976.8	3522.6	3655.5
55	0.359	0.266	46.726	48.413	1068.8	3476.3	3636.9
56	0.341	0.224	44.919	47.382	1184.2	3369.1	3571.2
57	0.377	0.288	47.683	49.277	1428.5	3562.1	3837.8
58	0.375	0.277	46.490	48.240	1472.4	3483.9	3782.3
59	0.370	0.226	45.126	48.152	1574.2	3379.0	3727.7
60	0.366	0.215	47.051	48.292	1819.5	3496.5	3941.6
61	0.384	0.274	48.029	51.402	1987.7	3583.4	4097.8
62	0.390	0.252	45.798	47.953	1906.1	3442.3	3934.8
63	0.393	0.261	46.119	47.368	2062.6	3438.4	4009.6
64	0.392	0.257	48.380	50.489	2450.2	3582.3	4340.0

Table A. 15. Stiffness coefficients and uncertainties for the high pre-swirl insert.

Test Point	K_{xx} [MN/m]	$U_{K_{xx}}$ [MN/m]	K_{xy} [MN/m]	$U_{K_{xy}}$ [MN/m]	K_{yx} [MN/m]	$U_{K_{yx}}$ [MN/m]	K_{yy} [MN/m]	$U_{K_{yy}}$ [MN/m]
1	1.07	0.15	0.87	0.09	-1.07	0.16	1.13	0.16
2	0.95	0.11	1.03	0.09	-1.09	0.21	0.88	0.09
3	0.29	0.25	1.95	0.16	-1.24	0.25	0.50	0.24
4	-2.02	1.02	3.36	0.61	-5.73	0.64	2.38	0.68
5	2.72	0.18	1.92	0.17	-2.31	0.20	2.81	0.13
6	1.53	0.12	2.46	0.09	-1.88	0.23	1.20	0.11
7	0.95	0.14	2.37	0.11	-2.25	0.27	1.35	0.19
8	-1.32	1.54	4.29	0.71	-6.07	0.78	2.68	0.77
9	-0.94	0.09	2.91	0.17	-3.23	0.41	-0.86	0.12
10	2.45	0.09	1.99	0.08	-3.95	0.25	2.00	0.11
11	1.97	0.11	3.00	0.11	-3.25	0.19	2.16	0.13
12	-0.81	1.71	5.75	0.72	-8.65	3.90	5.41	4.72
13	1.34	0.13	3.27	0.22	-3.72	0.33	1.57	0.18
14	3.33	0.13	2.57	0.12	-4.96	0.19	2.17	0.11
15	2.96	0.12	3.66	0.11	-4.29	0.10	3.05	0.15
16	0.07	1.31	6.15	0.66	-7.86	3.50	4.58	2.30
17	0.05	0.23	1.51	0.14	-1.83	0.32	0.14	0.27
18	-0.18	0.11	1.58	0.13	-1.83	0.19	0.03	0.16
19	0.01	0.19	2.11	0.18	-2.81	0.21	0.38	0.16
20	-0.02	2.02	3.51	0.54	-9.76	0.56	1.23	0.33
21	-1.13	0.49	2.63	0.33	-4.13	0.26	-0.98	0.38
22	1.11	0.17	2.89	0.09	-2.36	0.26	0.35	0.11
23	1.16	0.23	2.74	0.17	-3.54	0.29	0.84	0.08
24	-0.60	1.88	4.55	0.60	-12.57	3.80	4.68	2.90
25	-0.99	0.50	2.59	0.33	-5.17	0.66	-0.82	0.38
26	2.15	0.10	4.49	0.13	-2.64	0.24	0.49	0.12
27	1.84	0.32	3.43	0.22	-4.32	0.26	1.42	0.11
28	-1.65	2.78	6.97	0.80	-16.53	2.47	5.62	1.52
29	0.58	0.35	3.84	0.39	-4.24	0.62	0.77	0.42
30	2.81	0.21	5.23	0.13	-3.45	0.19	0.31	0.08
31	3.17	0.21	3.95	0.18	-5.03	0.20	2.16	0.13
32	-0.83	1.17	6.91	0.54	-12.25	1.59	6.17	0.87

Table A. 15. Stiffness coefficients and uncertainties for the high pre-swirl insert. (Continued)

Test Point	K_{xx} [MN/m]	$U_{K_{xx}}$ [MN/m]	K_{xy} [MN/m]	$U_{K_{xy}}$ [MN/m]	K_{yx} [MN/m]	$U_{K_{yx}}$ [MN/m]	K_{yy} [MN/m]	$U_{K_{yy}}$ [MN/m]
33	-0.37	0.12	3.04	0.06	-3.21	0.19	-0.26	0.12
34	-0.37	0.07	2.99	0.11	-3.36	0.12	-0.35	0.05
35	-0.27	0.18	3.84	0.21	-5.17	0.13	-0.64	0.10
36	5.63	2.33	5.42	0.59	-18.72	2.59	1.45	2.25
37	0.25	0.15	3.44	0.19	-3.59	0.25	0.29	0.15
38	0.11	0.14	3.61	0.20	-3.87	0.18	0.27	0.17
39	-0.63	0.19	4.27	0.27	-5.38	0.26	0.30	0.19
40	7.71	2.96	6.07	0.60	-25.13	2.60	3.64	0.74
41	1.63	0.11	3.53	0.12	-3.96	0.32	1.77	0.09
42	1.50	0.22	3.76	0.15	-4.07	0.49	1.70	0.27
43	-0.30	0.16	5.08	0.25	-4.54	0.26	1.37	0.21
44	0.15	2.84	7.77	0.73	-21.78	2.71	3.68	0.93
45	2.82	0.44	4.15	0.33	-5.07	0.76	3.25	0.68
46	1.75	0.22	4.75	0.13	-4.35	0.29	2.45	0.16
47	1.47	0.22	5.46	0.19	-7.44	1.87	3.28	3.41
48	-0.86	2.69	8.91	0.89	-23.22	2.47	4.76	1.07
49	-0.88	0.22	4.56	0.20	-4.69	0.26	-0.88	0.18
50	-0.97	0.30	4.83	0.12	-5.20	0.27	-0.82	0.16
51	-0.45	0.34	5.98	0.41	-10.37	1.57	-0.23	2.95
52	14.73	2.56	6.65	0.55	-23.26	1.46	2.43	1.24
53	-0.17	0.25	4.97	0.18	-5.15	0.27	-0.13	0.16
54	-0.23	0.15	5.16	0.17	-5.58	0.15	-0.21	0.14
55	-0.43	0.40	6.34	0.39	-10.66	1.26	-0.98	1.82
56	11.32	2.27	9.31	0.78	-24.72	0.94	-0.17	1.50
57	0.52	0.22	5.65	0.36	-5.73	0.27	0.74	0.23
58	0.25	0.18	6.14	0.40	-6.34	0.39	0.44	0.25
59	-0.35	0.33	6.42	0.37	-10.75	1.50	0.62	2.15
60	5.28	2.57	9.48	0.81	-26.33	1.46	1.47	1.01
61	2.04	0.21	5.43	0.14	-5.80	0.43	1.97	0.12
62	1.55	0.18	5.88	0.16	-6.11	0.26	1.86	0.16
63	-0.34	0.40	7.30	0.38	-11.28	1.53	2.86	2.42
64	3.72	2.45	10.42	0.83	-31.59	3.55	5.36	1.40

Table A. 16. Damping coefficients and uncertainties for the high pre-swirl insert.

Test Point	C_{xx} [kN-s/m]	$U_{C_{xx}}$ [kN-s/m]	C_{xy} [kN-s/m]	$U_{C_{xy}}$ [kN-s/m]	C_{yx} [kN-s/m]	$U_{C_{yx}}$ [kN-s/m]	C_{yy} [kN-s/m]	$U_{C_{yy}}$ [kN-s/m]
1	7.40	0.60	2.81	0.20	-2.62	0.20	7.57	0.54
2	7.42	0.89	2.69	0.33	-2.92	0.25	8.31	0.99
3	11.28	1.05	0.48	0.48	-5.89	0.30	13.42	1.25
4	59.04	3.34	-21.43	1.51	-29.69	1.47	31.15	1.51
5	9.88	0.55	3.92	0.47	-3.51	0.16	9.97	0.53
6	11.05	0.71	3.33	0.30	-3.66	0.40	11.69	0.89
7	13.96	0.86	1.91	0.42	-5.65	0.42	14.76	0.99
8	57.56	5.03	-18.68	2.12	-28.10	1.74	33.40	1.70
9	15.46	0.41	4.14	0.27	-4.12	0.45	15.43	0.40
10	13.07	0.41	4.92	0.26	-3.65	0.26	13.53	0.73
11	15.98	0.64	2.98	0.30	-5.96	0.38	16.44	0.79
12	57.32	5.57	-16.52	2.31	-27.67	5.32	36.10	3.70
13	14.98	0.20	4.88	0.20	-4.83	0.27	15.11	0.26
14	14.83	0.50	5.49	0.27	-4.36	0.22	15.28	0.59
15	17.38	0.71	3.67	0.30	-6.50	0.35	17.75	0.64
16	51.41	3.73	-14.28	1.49	-25.65	4.94	36.44	4.20
17	6.82	0.96	4.91	0.57	-4.35	0.29	6.61	1.03
18	7.53	0.75	4.83	0.32	-4.61	0.30	6.91	0.92
19	12.12	1.15	3.65	0.54	-6.53	0.27	8.71	1.19
20	48.93	3.74	-1.49	0.95	-14.35	1.07	16.51	1.19
21	12.21	1.48	5.37	0.72	-3.63	0.55	12.24	1.41
22	10.34	0.93	4.57	0.50	-5.31	0.35	10.46	1.02
23	13.35	1.41	4.49	0.36	-6.54	0.36	12.02	0.95
24	43.96	6.27	-6.54	1.59	-19.78	6.68	20.92	9.26
25	14.35	1.47	6.05	0.80	-4.58	0.59	14.41	1.29
26	12.99	0.64	5.60	0.47	-5.80	0.45	13.79	0.90
27	15.96	1.34	4.85	0.39	-7.46	0.46	14.83	0.80
28	69.02	10.08	-11.91	2.58	-27.70	7.28	28.58	10.87
29	15.29	0.30	6.47	0.26	-6.28	0.49	15.10	0.71
30	15.08	0.52	6.27	0.36	-6.18	0.58	16.11	0.76
31	16.80	0.88	5.81	0.37	-7.82	0.33	16.45	0.64
32	48.85	3.23	-8.37	1.21	-22.52	7.13	28.19	11.17

Table A. 16. Damping coefficients and uncertainties for the high pre-swirl insert. (Continued)

Test Point	C_{xx} [kN-s/m]	$U_{C_{xx}}$ [kN-s/m]	C_{xy} [kN-s/m]	$U_{C_{xy}}$ [kN-s/m]	C_{yx} [kN-s/m]	$U_{C_{yx}}$ [kN-s/m]	C_{yy} [kN-s/m]	$U_{C_{yy}}$ [kN-s/m]
33	8.61	0.83	6.50	0.32	-6.62	0.14	8.70	0.96
34	9.67	0.84	6.77	0.22	-6.61	0.22	8.92	0.76
35	15.60	1.25	7.27	0.31	-7.40	0.36	10.55	0.89
36	51.91	4.36	-0.16	1.39	-17.26	5.46	17.22	5.57
37	11.30	0.58	6.22	0.36	-6.28	0.24	11.31	0.72
38	12.50	0.41	6.12	0.35	-6.65	0.25	11.96	0.60
39	16.94	0.69	6.28	0.40	-8.64	0.38	13.68	0.56
40	67.96	5.25	-4.70	1.61	-23.20	5.95	24.07	7.36
41	11.87	0.52	7.71	0.41	-7.24	0.31	11.79	0.70
42	12.06	0.63	7.67	0.51	-7.52	0.36	12.02	1.18
43	15.51	0.89	7.20	0.41	-9.81	0.30	14.41	0.64
44	60.10	7.44	-1.59	1.87	-22.85	6.10	24.14	7.72
45	13.80	0.45	7.89	0.91	-8.02	1.03	13.34	0.74
46	14.11	0.76	7.79	0.50	-7.90	0.46	14.10	0.77
47	18.04	1.66	7.78	0.74	-10.17	1.86	16.05	2.07
48	63.95	9.49	-3.87	2.11	-25.56	5.90	28.43	8.33
49	9.08	0.84	9.02	0.48	-8.76	0.22	8.96	1.15
50	10.67	0.98	9.07	0.59	-9.24	0.24	9.63	1.22
51	19.38	1.78	9.33	0.64	-10.12	1.18	11.92	4.47
52	49.88	4.13	-3.23	1.62	-23.03	4.33	22.04	7.06
53	11.09	0.88	8.79	0.70	-8.54	0.21	10.95	1.25
54	12.47	0.97	8.78	0.48	-8.72	0.36	11.59	0.95
55	21.19	1.91	9.71	0.61	-9.99	1.29	14.91	2.52
56	56.75	3.61	2.55	1.56	-18.75	2.93	22.66	7.77
57	13.40	0.83	8.14	0.84	-8.10	0.54	13.11	1.18
58	15.45	0.68	7.92	0.79	-8.26	0.50	14.73	0.84
59	22.37	1.47	9.88	0.92	-11.98	1.61	16.61	2.46
60	58.29	5.47	5.94	1.78	-19.76	4.39	22.90	8.48
61	14.44	0.33	10.24	0.43	-9.76	0.56	14.05	0.85
62	15.06	0.61	9.94	0.37	-9.92	0.50	14.59	0.79
63	23.27	2.00	8.86	0.75	-13.56	1.79	17.52	3.29
64	66.39	5.28	2.59	1.53	-23.48	5.12	24.45	8.72

Table A. 17. Virtual mass coefficients and uncertainties for the high pre-swirl insert.

Test Point	M_{xx} [kg]	$U_{M_{xx}}$ [kg]	M_{xy} [kg]	$U_{M_{xy}}$ [kg]	M_{yx} [kg]	$U_{M_{yx}}$ [kg]	M_{yy} [kg]	$U_{M_{yy}}$ [kg]
1	15.23	0.23	0.08	0.14	-0.69	0.25	15.63	0.23
2	15.68	0.15	-0.13	0.13	-1.04	0.29	16.08	0.13
3	17.38	0.34	-0.72	0.22	-1.99	0.35	17.59	0.32
4	29.02	1.38	-4.50	0.83	-6.52	0.87	22.39	0.93
5	16.95	0.27	0.18	0.26	-1.23	0.30	17.31	0.19
6	16.63	0.17	0.09	0.13	-1.10	0.32	16.94	0.15
7	18.62	0.18	-0.93	0.15	-2.20	0.36	18.42	0.26
8	31.03	2.10	-4.64	0.96	-6.62	1.06	23.12	1.04
9	16.59	0.13	-0.34	0.25	-1.03	0.62	17.03	0.18
10	18.10	0.12	-0.64	0.11	-1.48	0.34	17.79	0.15
11	19.36	0.15	-0.67	0.15	-1.76	0.25	18.81	0.18
12	32.99	3.67	-5.42	1.55	-19.17	8.40	35.30	10.15
13	18.29	0.19	-0.71	0.33	-1.01	0.50	18.76	0.27
14	18.50	0.17	-0.56	0.17	-1.28	0.27	18.19	0.15
15	20.00	0.16	-0.62	0.14	-1.69	0.13	19.37	0.21
16	30.27	2.82	-3.95	1.41	-15.52	7.52	28.07	4.95
17	14.63	0.34	0.14	0.21	-1.46	0.49	15.01	0.40
18	14.97	0.17	0.10	0.19	-1.10	0.29	14.97	0.23
19	16.99	0.26	0.50	0.25	-1.35	0.29	15.20	0.21
20	27.71	2.76	-0.42	0.74	-2.54	0.76	17.45	0.46
21	14.88	0.68	-0.09	0.46	-2.81	0.36	15.44	0.53
22	16.42	0.23	0.97	0.12	-0.77	0.36	15.96	0.15
23	18.96	0.33	0.46	0.24	-1.51	0.41	16.56	0.11
24	30.40	4.04	-2.00	1.29	-16.79	8.17	25.95	6.24
25	16.24	0.70	-0.23	0.46	-2.13	0.92	17.67	0.52
26	17.47	0.14	0.84	0.17	-0.60	0.32	16.90	0.16
27	19.90	0.45	0.33	0.31	-1.17	0.36	17.51	0.16
28	38.15	5.98	-3.94	1.71	-14.66	5.32	24.28	3.26
29	18.50	0.54	-1.24	0.60	-1.42	0.96	19.11	0.64
30	18.06	0.31	0.50	0.19	-0.44	0.29	16.92	0.11
31	19.95	0.30	0.07	0.25	-0.94	0.28	18.24	0.19
32	28.77	2.51	-2.05	1.17	-10.11	3.41	23.50	1.87

Table A. 17. Virtual mass coefficients and uncertainties for the high pre-swirl insert. (Continued)

Test Point	M_{xx} [kg]	$U_{M_{xx}}$ [kg]	M_{xy} [kg]	$U_{M_{xy}}$ [kg]	M_{yx} [kg]	$U_{M_{yx}}$ [kg]	M_{yy} [kg]	$U_{M_{yy}}$ [kg]
33	13.29	0.17	0.76	0.09	-1.49	0.29	13.46	0.18
34	13.57	0.10	0.76	0.17	-0.92	0.19	13.46	0.07
35	16.12	0.26	1.75	0.29	-0.52	0.19	13.80	0.14
36	30.76	5.01	-1.91	1.26	-15.29	5.57	17.65	4.84
37	13.69	0.22	0.59	0.28	-1.39	0.38	13.82	0.22
38	14.37	0.21	0.61	0.31	-1.09	0.28	14.04	0.25
39	17.64	0.27	0.51	0.37	-1.09	0.36	15.50	0.26
40	37.09	6.36	-3.75	1.29	-18.28	5.60	21.31	1.59
41	16.82	0.16	0.08	0.18	-1.65	0.49	17.00	0.14
42	17.35	0.30	-0.09	0.21	-1.85	0.69	17.34	0.38
43	19.51	0.23	-0.49	0.35	-1.70	0.37	17.87	0.30
44	35.39	6.11	-0.77	1.57	-15.00	5.83	22.38	2.01
45	18.11	0.62	-0.22	0.46	-3.31	1.07	19.27	0.95
46	17.22	0.30	0.32	0.19	-0.91	0.41	17.59	0.23
47	19.86	0.48	0.66	0.40	-9.58	4.02	26.05	7.35
48	34.67	5.80	-0.97	1.91	-13.51	5.32	21.21	2.29
49	13.65	0.31	0.99	0.28	-2.05	0.37	13.56	0.25
50	14.27	0.42	1.07	0.17	-1.92	0.37	13.75	0.22
51	16.79	0.73	2.85	0.88	-8.32	3.38	19.11	6.34
52	31.27	5.50	-4.76	1.19	-11.67	3.14	10.09	2.66
53	13.71	0.35	1.14	0.26	-2.13	0.38	13.45	0.23
54	13.97	0.21	1.60	0.24	-1.54	0.21	13.49	0.19
55	17.88	0.87	1.76	0.83	-8.49	2.71	16.90	3.93
56	32.12	4.88	-0.66	1.68	-11.62	2.03	10.45	3.23
57	13.24	0.31	1.64	0.50	-2.63	0.37	13.45	0.32
58	14.30	0.26	1.56	0.56	-1.73	0.54	13.45	0.35
59	19.68	0.71	-0.63	0.80	-7.81	3.22	21.84	4.62
60	34.83	5.53	0.22	1.73	-9.62	3.13	18.40	2.16
61	18.07	0.36	-0.53	0.24	-1.44	0.73	17.48	0.21
62	17.66	0.25	0.16	0.23	-0.76	0.37	17.19	0.22
63	20.03	0.87	0.29	0.82	-8.15	3.29	23.85	5.20
64	35.83	4.69	-0.98	1.59	-18.85	6.80	24.80	2.67

Table A. 18. Whirl frequency ratio, effective damping, and uncertainties for the high pre-swirl insert.

Test Point	Target			Measured			
	ω [rpm]	ΔP [bar]	ε ϵ_0	WFR [-]	U_{WFR} [-]	C_{eff} [kN-s/m]	$U_{C_{eff}}$ [kN-s/m]
1	2000	2.07	0.00	0.62	0.07	2.93	-0.05
2	2000	2.07	0.27	0.64	0.09	2.93	0.22
3	2000	2.07	0.53	0.62	0.08	5.03	0.16
4	2000	2.07	0.8	0.53	0.09	24.57	-0.54
5	2000	4.14	0.00	1.01	0.07	0.00	-0.35
6	2000	4.14	0.27	0.90	0.07	1.17	0.01
7	2000	4.14	0.53	0.77	0.06	3.66	0.03
8	2000	4.14	0.8	0.60	0.10	21.98	-0.17
9	2000	6.21	0.00	0.95	0.07	0.95	-0.97
10	2000	6.21	0.27	1.01	0.05	-0.63	-0.21
11	2000	6.21	0.53	0.92	0.04	1.57	0.01
12	2000	6.21	0.8	0.76	0.26	14.95	-6.39
13	2000	8.27	0.00	1.10	0.06	-1.44	-1.09
14	2000	8.27	0.27	1.13	0.05	-2.69	-0.21
15	2000	8.27	0.53	1.08	0.04	-1.12	0.19
16	2000	8.27	0.8	0.82	0.22	12.58	-5.94
17	4000	2.07	0.00	0.59	0.09	3.07	0.44
18	4000	2.07	0.27	0.56	0.06	3.41	0.45
19	4000	2.07	0.53	0.57	0.06	4.93	0.70
20	4000	2.07	0.8	0.50	0.05	17.52	1.15
21	4000	4.14	0.00	0.65	0.07	4.77	0.74
22	4000	4.14	0.27	0.60	0.05	4.51	0.55
23	4000	4.14	0.53	0.58	0.05	5.61	0.63
24	4000	4.14	0.8	0.61	0.21	15.95	2.52
25	4000	6.21	0.00	0.62	0.07	5.61	0.20
26	4000	6.21	0.27	0.60	0.04	5.19	0.33
27	4000	6.21	0.53	0.60	0.04	6.47	0.50
28	4000	6.21	0.8	0.60	0.17	24.67	6.57
29	4000	8.27	0.00	0.63	0.06	6.12	-0.69
30	4000	8.27	0.27	0.63	0.03	5.44	0.26
31	4000	8.27	0.53	0.64	0.03	6.12	0.31
32	4000	8.27	0.8	0.60	0.16	18.20	4.66

Table A. 18. Whirl frequency ratio, effective damping, and uncertainties for the high pre-swirl insert. (Continued)

Test Point	Target			Measured			
	ω [rpm]	ΔP [bar]	ε ϵ_0	WFR [-]	U_{WFR} [-]	C_{eff} [kN-s/m]	$U_{C_{eff}}$ [kN-s/m]
33	6000	2.07	0.00	0.57	0.05	4.39	0.69
34	6000	2.07	0.27	0.54	0.04	4.77	0.62
35	6000	2.07	0.53	0.55	0.04	6.61	0.80
36	6000	2.07	0.8	0.53	0.10	20.77	2.44
37	6000	4.14	0.00	0.49	0.03	6.34	0.30
38	6000	4.14	0.27	0.49	0.02	6.81	0.20
39	6000	4.14	0.53	0.50	0.02	8.13	0.21
40	6000	4.14	0.8	0.50	0.09	28.11	3.76
41	6000	6.21	0.00	0.50	0.03	6.41	0.26
42	6000	6.21	0.27	0.52	0.04	6.42	0.39
43	6000	6.21	0.53	0.51	0.03	8.00	0.35
44	6000	6.21	0.8	0.55	0.11	23.57	4.84
45	6000	8.27	0.00	0.54	0.05	7.34	-0.27
46	6000	8.27	0.27	0.51	0.03	7.25	0.42
47	6000	8.27	0.53	0.59	0.09	10.01	0.23
48	6000	8.27	0.8	0.55	0.11	25.18	6.24
49	8000	2.07	0.00	0.61	0.05	4.79	0.72
50	8000	2.07	0.27	0.59	0.05	5.42	0.87
51	8000	2.07	0.53	0.62	0.13	10.59	1.95
52	8000	2.07	0.8	0.41	0.08	25.02	4.39
53	8000	4.14	0.00	0.55	0.04	6.36	0.79
54	8000	4.14	0.27	0.53	0.03	6.94	0.77
55	8000	4.14	0.53	0.55	0.06	12.21	1.23
56	8000	4.14	0.8	0.46	0.08	24.57	4.66
57	8000	6.21	0.00	0.51	0.03	8.26	0.63
58	8000	6.21	0.27	0.49	0.03	9.03	0.30
59	8000	6.21	0.53	0.52	0.06	12.79	0.85
60	8000	6.21	0.8	0.50	0.09	23.37	5.62
61	8000	8.27	0.00	0.47	0.02	8.37	0.26
62	8000	8.27	0.27	0.48	0.02	8.06	0.44
63	8000	8.27	0.53	0.53	0.07	12.85	1.51
64	8000	8.27	0.8	0.54	0.10	28.68	4.39

APPENDIX B UNCERTAINTY ANALYSIS

The author used the same general testing apparatus, instrumentation, procedure, and data analysis tools that Moreland and Torres used in their test program [8, 12]. Consequently, the author uses Moreland's uncertainty analysis, adapting it, where needed, to the current study as follows:

"Instrument error is assumed to be negligible and only repeatability is calculated for the uncertainty of measurements. A 95% confidence interval is used to calculate the uncertainties for static measurements and the dynamic stiffness values. The true mean, μ, of a set of sample measurements, x_i, lies within the confidence interval

$$\tilde{x} - t_{\alpha/2,v}\frac{S_x}{\sqrt{n}} < \mu < \tilde{x} + t_{\alpha/2,v}\frac{S_x}{\sqrt{n}} \tag{B. 1}$$

where $\tilde{x}$ is the sample mean, $t_{\alpha/2,v}$ is the Student's t-distribution value, the level of significance is $\alpha = 1 - c$, c = 0.95 is the level of confidence, the degrees of freedom are v = 1 - n, and n is the number of samples. The standard deviation is

$$S_x = \sqrt{\left(\frac{\sum_{i=1}^{n} x_i^2 - n\bar{x}^2}{n-1}\right)} \tag{B. 2}$$

Recalling Eqs. (19)-(23), the confidence intervals on the rotordynamic coefficients are determined using a statistical test described in [26]. The true slope of a least-squares regression lies within the c% confidence interval

$$b \pm t_{\alpha/2,v}\frac{S_{y/x}}{S_{xx}} \tag{B. 3}$$

where the standard error of the y-data about the curve fit is

$$S_{y/x} = \left(\frac{1}{n-2}\sum_{i=1}^{n}[y_i - y(x_i)]^2\right) \tag{B. 4}$$

and the total squared variation of the independent variable, x_i, is

$$S_{xx}^2 = \sum_{i=1}^{n}(x_i - \bar{x})^2 \tag{B. 5}$$

Finally, the true intercept lies within the interval

$$a \pm t_{\alpha/2,v} S_{y/x}\sqrt{\frac{1}{n} + \frac{\overline{x^2}}{S_{xx}^2}} \tag{B. 6}$$

Confidence intervals of the rotordynamic coefficients are propagated into the confidence intervals on the WFR, K_{eff} and values. Uncertainty propagation is defined as”

$$u_y = \sqrt{\left(\frac{\partial y}{\partial x_1}u_1\right)^2 + \left(\frac{\partial y}{\partial x_2}u_2\right)^2 + \cdots + \left(\frac{\partial y}{\partial x_n}u_n\right)^2} \tag{B. 7}$$